FDTD MODELING OF THE EARTH-IONOSPHERE WAVEGUIDE: STOCHASTIC SIMULATIONS AS WELL AS STUDIES OF GEOMAGNETICALLY-INDUCED CURRENTS

by

Bach Thanh Nguyen

A dissertation submitted to the faculty of
The University of Utah
in partial fulfillment of the requirements for the degree of

Doctor of Philosophy

Department of Electrical and Computer Engineering

The University of Utah

December 2017

The University of Utah Graduate School

STATEMENT OF DISSERTATION APPROVAL

The dissertation of **Bach Thanh Nguyen**
has been approved by the following supervisory committee members:

Jamesina J. Simpson ,	Chair(s)	**14 August 2017** Date Approved
Cynthia M. Furse ,	Member	**14 August 2017** Date Approved
Robert Michael Kirby II ,	Member	**14 August 2017** Date Approved
David Alan Schurig ,	Member	**14 August 2017** Date Approved
Berardi Sensale Rodriguez ,	Member	**14 August 2017** Date Approved

by **Behrouz Farhang-Boroujeny** , Chair/Dean of
the Department/College/School of **Electrical and Computer Engineering**
and by **David B. Kieda** , Dean of The Graduate School.

ABSTRACT

The finite-difference time-domain (FDTD) method is a robust numerical modeling approach that has been widely utilized over the past couple decades to solve for electromagnetic (EM) wave propagation in the Earth-ionosphere waveguide. There are two main approaches to modeling EM wave propagation in the ionosphere: (1) treating the ionosphere as an isotropic medium; or (2) treating the ionosphere as an anisotropic medium (i.e., magnetized ionospheric plasma). The first approach simply utilizes an electrical conductivity profile to represent the ionosphere and ignores the influence of the geomagnetic field. The second approach accounts for the Earth's magnetic field as well as the density and collision frequencies of the electrons.

All of the existing FDTD-based Earth-ionosphere models to date account for only the average composition values of the ionosphere and then solve for only the expected average EM fields without considering uncertainties. Not accounting for the variability of the ionosphere content limits the utility and capability of EM modeling for applications such as communications, surveillance, navigation, and geophysical applications.

The primary objective of this dissertation is to improve the versatility and computational efficiency of FDTD models by treating the ionosphere as a random medium. Specifically, stochastic methods are applied to FDTD models in order to better assess how ionosphere variability affects the characteristics of EM wave propagation in the Earth-ionosphere waveguide. Two different stochastic algorithms are implemented into FDTD models: the Galerkin-based polynomial chaos expansion, namely PCE-FDTD, and the delta method, namely S-FDTD. The former is applied to both isotropic and anisotropic ionosphere models. While its accuracy and efficiency show potential advantages compared with the conventional Monte Carlo method, its efficiency is declined when applying to anisotropic model due to the complexity nature of the anisotropic magnetized plasma algorithm. Therefore, the latter is applied to anisotropic model in order to search a more effective model in term of computational cost.

The second objective of this dissertation is to introduce a new possibility for applying the global FDTD Earth-ionosphere waveguide model to forecasting geomagnetically induced currents (GICs). GICs can disrupt the operation of electric power grids during geomagnetic storms and potentially cause widespread blackouts.

To my little daughter Mia

CONTENTS

LIST OF FIGURES

LIST OF TABLES

ACKNOWLEDGEMENTS

I foremost would like to express my sincere gratitude to my advisor, Prof. Jamesina Simpson, for her continuous research supervision and support during the course of this research. I thank her for giving me an opportunity to work with her and for her patience and encouragement throughout this research project. As advisor, mentor, and friend, her influence and guidance will have a lasting effect on my career and my life.

I also would like to thank Prof. Cynthia Furse, Prof. Mike Kirby, Prof. David Schurig, and Prof. Berardi Rodriguez for agreeing to be on my PhD committee and for providing precise and prompt feedback on this dissertation despite their busy schedules.

I would like to thank the past and present members of our research group: Alireza Samimi, Mehdi Hasan, Zhuo Su, Miguel Rodriguez, Sean Burns, Santosh Pokhrel, Dallin Smith, and Victor Taylor, for being such nice colleagues and for many interesting discussions. It was a great pleasure to work with them.

Finally, I owe my deepest gratitude to my parents, Tung and Doanh, my Japanese parents, Kenichi and Taeko Ohno. This work would not have been possible without their unconditional love and support.

This work was supported by the National Science Foundation (NSF) CAREER Award grant #0955404, by the National Science Foundation (NSF) Awards OCI-0725070 and ACI-1238993, by the Blue Waters Sustained Petascale Computing Project Award #1440023, and by the U.S. Air Force.

CHAPTER 1

INTRODUCTION

1.1 Overview

Many communications, radar, and geophysical studies and applications rely on accurate knowledge of both the state of the Earth-ionosphere system and the characteristics of electromagnetic (EM) signal propagation through or reflected by the lithosphere and ionosphere. Satellite communications, the Global Positioning System (GPS), over-the-horizon radar, target direction finding, Schumann resonances, hypothesized earthquake precursors, and ionospheric remote sensing are some example applications. The success of these applications would be greatly improved with the availability of accurate modeling capabilities. Poor understanding of either the Earth-ionospheric state or the complete signal propagation characteristics through the Earth-ionosphere can negatively affect the performance of these applications. For example, inaccurate signal predictions may lead to erroneous target identification and coordinate estimation.

Three major challenges, however, must be overcome in order to perform realistic calculations of EM propagation through the ionosphere:

- The ionosphere is comprised of both large and small-scale structures that often need to be accommodated.
- For many applications, the EM wave frequency is high enough such that complex magnetized plasma physics must be accommodated.
- The ionosphere exhibits high variability and uncertainty in both time and space.

Ray tracing has traditionally been employed for Earth-ionospheric EM wave propagation because it is computationally inexpensive, however it is: (1) incapable of taking into account the full ionospheric variability and/or terrain between the transmitters and receivers; (2) restrictive, in that particular methodologies of implementing the ray tracing

are limited to certain frequency ranges, and its accuracy depends on the plasma properties; (3) it provides solutions at only individual frequencies (steady-state solutions may be obtained; pulses cannot be studied).

The finite-difference time-domain (FDTD) method [1], [2] is a robust computational EM technique that has been applied to problems across the EM spectrum, from low-frequency geophysical problems below 1 Hz and up into the optical frequency range. The FDTD method has been also widely utilized over the past couple decades to solve for EM wave propagation in the Earth-ionosphere waveguide (e.g., [3]–[16]). The advantages of FDTD for Earth-ionosphere wave propagation problems include [12], [13]:

- As a grid-based method, the three-dimensional (3-D) spatial material variations of the ionosphere composition, topography/bathymetry, lithosphere composition, geomagnetic field, targets, and antennas, etc., may be accommodated. Figure 1.1 for example, shows FDTD-calculated global EM propagation in the Earth-ionosphere waveguide below 1 kHz that includes details of the Earths topography, bathymetry, oceans, and an (isotropic) conductivity layering in the ionosphere, which is sufficient for propagation below 1 kHz.
- The complex shielding, scattering and diffraction of EM wave may be calculated in a straightforward manner.
- Any number of simultaneous sources may be accommodated (antennas, plane waves, lightning, ionospheric currents, etc.).
- Any number of observation points may be accommodated, and movies may be created of the time-marching propagating waves.
- As a time-domain method, FDTD can model arbitrary time-varying source waveforms, movement of objects, and time variations in the ionosphere.
- Results may be obtained over a large spectral bandwidth via a discrete Fourier transform.
- A fully 3-D magnetized ionospheric plasma FDTD algorithm may be used to calculate all important ionospheric effects on signals, including absorption, refraction, phase and group delay, frequency shift, polarization, and Faraday rotation.

The downside of being able to accommodate all of the above details and physics, is that the FDTD model may quickly become very memory- and time-intensive, and thus, require significant supercomputing resources. This makes real-time calculations difficult or sometimes even impossible to obtain. Further, if the EM frequency is high enough (and the required grid resolution low enough), the required grid size may become computational infeasible, especially for long propagation paths. Although supercomputing capabilities continue to improve, efficient FDTD algorithms are needed to make EM wave propagation modeling in the Earth-ionosphere feasible and manageable.

Many FDTD models for Earth-ionosphere EM wave propagation simply utilize an electrical conductivity profile to represent the ionosphere and ignore the influence of the geomagnetic field (e.g., [9], [17]–[19]). This assumption appears to be adequate in calculating the average propagation of EM waves below 100 km in altitude and at frequencies of less than 1 kHz over thousands of kilometers. In this case, the governing equations are simpler and require less computational resources compared than when the geomagnetic field is taken into account. When the effects of the geomagnetic field are negligible, the simpler ionospheric conductivity profile is sufficient, such as when modeling global propagation at extremely low frequencies (ELF) and lower frequencies.

In recent years, FDTD anisotropic magnetized ionospheric plasma algorithms have been incorporated into global FDTD models to extend their capabilities. Specifically, a fully three-dimensional (3-D) Cartesian plasma model developed in [14] was applied to the 3-D FDTD latitude-longitude global spherical grid [15] of [9]. By accounting for 3-D magnetized ionospheric plasma physics, [14] was the first global FDTD model to include the calculation of all important ionospheric effects on signals, including absorption, refraction, phase and group delay, frequency shift, polarization, and Faraday rotation. Subsequently, a more efficient magnetized plasma algorithm that avoids the complex matrix formulation used in [15] was published and adapted to the 3-D FDTD latitude-longitude global model [16].

There is still significant progress yet to be made in developing an efficient FDTD modeling methodology that is accurate for all realistic ionosphere composition scenarios, especially the disturbed ionosphere conditions during space weather events. The primary objective of this dissertation is to introduce an effective and fast FDTD-based algorithm

that is well-suited for large scale and large uncertainty of the Earth-ionosphere modeling, so that the EM wave propagation is well understood. In particular, the proposed models in this dissertation could provide a full understanding of the true physics due to the associated uncertainties and applicable for a wide band of frequencies.

Furthermore, as computing capabilities further improve over time, the application of advanced 3-D FDTD models to various problems relating to complex EM wave propagation in the global Earth-ionosphere waveguide is especially promising. Global FDTD models have already been used for a wide range of applications such as calculations of Schumann resonances [20], remote sensing of oil fields [21], remote sensing of ionospheric disturbances [22], and for modeling hypothesized electromagnetic earthquake precursors [23] etc. References [12] and [13] provide a thorough summary of all FDTD local and global models of the Earth-ionosphere system up until the time of their respective publication dates. Another goal of the work described in this dissertation is to apply the global 3-D FDTD model of the Earth-ionosphere cavity to investigate space weather effects on the ground-level electric fields, which provides principle information to calculate the geomanetically induced currents (GICs) that can cause problems in conductor systems operated on the surface of Earth.

1.2 Organization of dissertation

This dissertation consists of seven chapters. Chapter 2 presents background information about the fundamentals of the FDTD method and brief introduction to the basic concepts of probability theory and overview of numerical methods for stochastic computations. Chapter 3 describes the implementation of the stochastic method based on the polynomial chaos expansion in the global isotropic FDTD model of the Earth-ionosphere waveguide that captures the uncertainty in ionospheric conductivity, and quantifies the impact of such variability on the electromagnetic response of stochastic systems in FDTD. Chapter 4 develops the implementation of the polynomial chaos expansion method in the Cartesian 3-D anisotropic FDTD model in order to better estimate the statistic of electromagnetic wave propagation in magnetized cold plasma medium under the variability effect of ionosphere contents and the Earth's geomagnetic field. Chapter 5 develops an alternative approach to the polynomial chaos expansion method and instead uses the

delta method to represent the stochastic / variability of the EM wave propagation in the magnetized cold plasma medium. Next, Chapter 6 presents a potential application of the global isotropic FDTD model of the Earth-ionosphere waveguide for forecasting the geomanetically induced currents (GICs). Finally, Chapter 7 provides conclusions and a discussion of future research in this area.

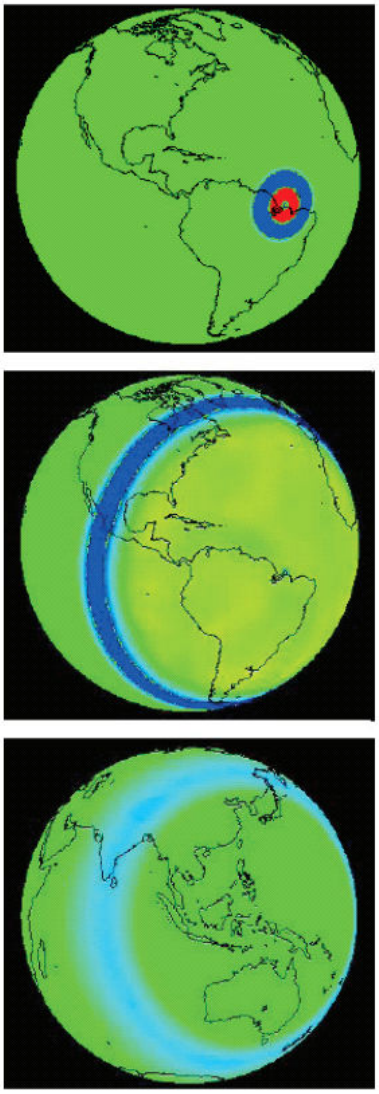

Figure 1.1: Snapshot visualizations of round-the-world EM propagation below 1 kHz as calculated by a 3-D FDTD model, including details of the Earth's topography, oceans, and isotropic ionosphere (figure courtesy of [12]).

CHAPTER 2

BACKGROUND

This chapter provides the background material necessary for development of the Earth-ionosphere modeling in this dissertation. First, the fundamentals of the finite-difference time-domain (FDTD) method are introduced. Next, an overview of techniques for uncertainty analysis is discussed. The polynomial chao expansion (PCE), in particular the Galerkin-based PCE, and the delta method are discussed in more detail, because they provide some of the necessary equations for the derivation of the stochastic equations in Chapters 3-5.

2.1 Finite difference time domain method

2.1.1 Maxwell's equations in three dimensions

In order to develop computationally efficient models to predict electromagnetic wave propagation within Earth-ionosphere waveguide, it is necessary to adequately model the electromagnetic nature of the propagation process without any priori assumptions. In this regard, full wave electromagnetic methods can be used to gain considerable insight into how the Earth-ionosphere structure can influence the electromagnetic fields. This Section introduces the fundamentals of the FDTD method and outlines the parallel implementation strategy of the numerical codes developed.

The FDTD method was first proposed by Yee in 1966 [1], however the high computational cost prevented extensive use and investigation of the method at that time. In 1975, Taflove published a turning paper of the stability bounds and an absorbing boundary condition [24]. Since then, there has been renewed interest and the method has emerged as a primary means to computationally model many scientific and engineering problems dealing with EM wave interactions with material structures [2, pp. 3-5]. This Section briefly focuses on some basic aspects of the FDTD method relevant for modeling propagation within the Earth-ionosphere waveguide (a complete description of the FDTD method

can be found in [2]).

Maxwell's equations describe the spatio-temporal behavior of electric and magnetic fields and hence form the foundation of classical electromagnetism. Considering a source-free region containing materials that may absorb electric energy, then the time-dependent Maxwell's equations are given in differential form as follows

$$\nabla \times \mathbf{E} = -\frac{\partial \mathbf{B}}{\partial t} \tag{2.1}$$

$$\nabla \times \mathbf{H} = \frac{\partial \mathbf{D}}{\partial t} + \mathbf{J} \tag{2.2}$$

$$\nabla \cdot \mathbf{D} = 0 \tag{2.3}$$

$$\nabla \cdot \mathbf{B} = 0 \tag{2.4}$$

where

$\mathbf{E}$: electric field (V/m)

$\mathbf{H}$: magnetic field (A/m)

$\mathbf{D}$: electric flux density (C/m^2)

$\mathbf{B}$: magnetic flux density (Wb/m^2)

$\mathbf{J}$: electric current density (A/m^2)

Furthermore, in linear, isotropic, and nondispersive medium, $\mathbf{E}$ and $\mathbf{H}$ are related to $\mathbf{D}$ and $\mathbf{B}$ via the constitutive equations, given by

$$\mathbf{D} = \epsilon \mathbf{E} = \epsilon_0 \epsilon_r \mathbf{E} \tag{2.5}$$

$$\mathbf{B} = \mu \mathbf{H} = \mu_0 \mu_r \mathbf{H} \tag{2.6}$$

$$\mathbf{J} = \mathbf{J}_{source} + \sigma \mathbf{E} \tag{2.7}$$

where

μ_0 : permeability of free-space, $4\pi \times 10^{-7}(H/m)$

μ_r : relative permeability of the medium

ϵ_0 : permittivity of free-space, $8.8542 \times 10^{-12}(F/m)$

ϵ_r : relative permittivity of the medium

σ : electric conductivity (S/m)

The electrical and magnetic properties of the Earth-ionosphere, i.e., the dielectric permittivity (ϵ), the magnetic permeability (μ), and the electric conductivity (σ) will influence how electromagnetic signals travel in the Earth-ionosphere system. In general, ϵ, μ,

and σ all vary with position in the Earth-ionosphere. However, variations in μ_r are usually encountered only in major ore bodies. Additionally, considering the low-frequency range studied in this dissertation, displacement current is much smaller than conduction current and thus this study is completely insensitive to variations in permittivity. Hence, the dielectric permittivity and the magnetic permeability are assumed to be constants and equal to its values in free space throughout this dissertation. On the other hand, variations in the electrical conductivity are usually much larger than variations in the other two parameters, often orders of magnitude. The electrical conductivity variation significantly affects the electromagnetic wave propagation in the Earth-ionosphere medium and therefore will be main subject in this dissertation's analysis.

Next, substituting three proportion relations (2.5)-(2.7) into equations (2.1) and (2.2) and expanding the curl operators in Cartesian coordinates leads to six coupled differential equations

$$\frac{\partial H_x}{\partial t} = \frac{1}{\mu_0}\left[\frac{\partial E_y}{\partial z} - \frac{\partial E_z}{\partial y}\right] \tag{2.8}$$

$$\frac{\partial H_y}{\partial t} = \frac{1}{\mu_0}\left[\frac{\partial E_z}{\partial x} - \frac{\partial E_x}{\partial z}\right] \tag{2.9}$$

$$\frac{\partial H_z}{\partial t} = \frac{1}{\mu_0}\left[\frac{\partial E_x}{\partial y} - \frac{\partial E_y}{\partial x}\right] \tag{2.10}$$

$$\frac{\partial E_x}{\partial t} = \frac{1}{\epsilon_0}\left[\frac{\partial H_z}{\partial y} - \frac{\partial H_y}{\partial z} - \left(J_{source_x} + \sigma E_x\right)\right] \tag{2.11}$$

$$\frac{\partial E_y}{\partial t} = \frac{1}{\epsilon_0}\left[\frac{\partial H_x}{\partial z} - \frac{\partial H_z}{\partial x} - \left(J_{source_y} + \sigma E_y\right)\right] \tag{2.12}$$

$$\frac{\partial E_z}{\partial t} = \frac{1}{\epsilon_0}\left[\frac{\partial H_y}{\partial x} - \frac{\partial H_x}{\partial y} - \left(J_{source_z} + \sigma E_z\right)\right] \tag{2.13}$$

These equations form the basis of the FDTD numerical algorithm for electromagnetic wave interactions with general three-dimensional (3-D) objects. Except simple cases, analytical solutions to these equations are generally difficult or impossible to obtain.

2.1.2 The Yee algorithm

To numerically discretize equations (2.8)-(2.13), Yee defined an orthogonal cubic lattice whose unit cell is illustrated in Figure 2.1 to spatially allocate the field components. For this allocation, each field component is sampled and evaluated at a particular space position so that every E component is surrounded by four circulating H components, and similarly,

each H component is surrounded by four circulating E components. This provides an efficient yet simple picture of three-dimensional space being filled by interlinked arrays of Faraday's law and Ampere's law contours. It should be noted that this staggered arrangement also simultaneously satisfies the two Gauss's laws (equations (2.3) and (2.4)). Thus, it is possible to identify the E components linking with the H loops and, correspondingly, the H components linking with the E loops as shown in Figure 2.1. The materials are modeled by specifying their characteristic constants (ϵ, μ, and σ) at every grid point. The leapfrog algorithm proposed by Yee interleaves the H- and E-fields in time by half the sampling time step. The time advancing algorithm is explicit and can be easily adapted into computer programs to be solved numerically.

The novelty of Yee algorithm was to apply second order accurate centered finite difference approximations in time and space to discretize the temporal and spatial partial differentiation operators of (2.8)-(2.13). For spatial grid separations Δx, Δy, and Δz and time increment Δt, a field component, U, may be written as

$$U(x,y,z,t) = U(i\Delta x, j\Delta y, k\Delta z, n\Delta t) = U|^n_{i,j,k} \tag{2.14}$$

We now can apply the above ideas and notation to achieve a numerical approximation of the Maxwell's curl equations. For example, consider the E_x field component equation (2.11), repeated here for convenience,

$$\frac{\partial E_x}{\partial t} = \frac{1}{\epsilon_0}\left[\frac{\partial H_z}{\partial y} - \frac{\partial H_y}{\partial z} - (J_{source_x} + \sigma E_x)\right] \tag{2.15}$$

And applying central differences, leading to

$$\begin{aligned}\frac{E_x|^{n+1/2}_{i,j+1/2,k+1/2} - E_x|^{n-1/2}_{i,j+1/2,k+1/2}}{\Delta t} = \frac{1}{\epsilon_0}\Bigg[&\frac{H_z|^n_{i,j+1,k+1/2} - H_z|^n_{i,j,k+1/2}}{\Delta y} \\ &- \frac{H_y|^n_{i,j+1/2,k+1} - H_y|^n_{i,j+1/2,k}}{\Delta z} - J_{source_x}|^n_{i,j+1/2,k+1/2} - \sigma_{i,j+1/2,k+1/2} E_x|^n_{i,j+1/2,k+1/2}\Bigg]\end{aligned} \tag{2.16}$$

However, since $E_x|^n_{i,j+1/2,k+1/2}$ is not assumed to be known for this scheme, a semi-implicit approximation is used to estimate the electric field at time step n

$$E_x|^n_{i,j+1/2,k+1/2} = \frac{E_x|^{n+1/2}_{i,j+1/2,k+1/2} + E_x|^{n-1/2}_{i,j+1/2,k+1/2}}{2} \tag{2.17}$$

Substituting (2.17) into (2.16) and solving for $E_x|^{n+1/2}_{i,j+1/2,k+1/2}$ gives the update equation for E_x as

$$E_x|^{n+1/2}_{i,j+1/2,k+1/2} = \left(\frac{1-\frac{\sigma_{i,j+1/2,k+1/2}\Delta t}{2\epsilon_0}}{1+\frac{\sigma_{i,j+1/2,k+1/2}\Delta t}{2\epsilon_0}}\right) E_x|^{n-1/2}_{i,j+1/2,k+1/2} + \left(\frac{\frac{\Delta t}{\epsilon_0}}{1+\frac{\sigma_{i,j+1/2,k+1/2}\Delta t}{2\epsilon_0}}\right) \cdot \left[\frac{H_z|^n_{i,j+1,k+1/2} - H_z|^n_{i,j,k+1/2}}{\Delta y} - \frac{H_y|^n_{i,j+1/2,k+1} - H_y|^n_{i,j+1/2,k}}{\Delta z} - J_{source_x}|^n_{i,j+1/2,k+1/2}\right] \tag{2.18}$$

Similar expressions can be derived for the remaining electric and magnetic field components.

2.1.3 Numerical dispersion and stability

As in every computation method, also in the FDTD, the time step and the grid size must be well chosen, so that the time and length scale phenomena of interest are properly resolved in the problem. In addition, time step and grid size affect the speed and accuracy of the code.

The FDTD algorithm introduces nonphysical numerical dispersion, which can influence the components of the E and H fields [2, p. 107]. In a free-space lattice, dispersion causes the phase velocity to depend on the frequency, direction of propagation and grid discretization. The extent of these effects can be quantified by comparing finite-difference solutions of monochromatic plane wave propagation with analytical solutions. It has been found that the spatial sampling density greatly influences the numerical dispersion error [2, pp. 120-128]. In particular, the dispersion error decreases with increased sampling density, and reduces to zero, in the limit, as the grid size approaches zero.

For propagation in free space, i.e., $\epsilon_r = \mu_r = 1$, the numerical phase velocity is given by

$$v_p = \frac{\pi}{N_\lambda \sin\left[\frac{1}{S}\sin\left(\frac{\pi S}{N_\lambda}\right)\right]} c_0 \tag{2.19}$$

where $S = c_0\Delta t/\Delta$ is the Courant number, $N_\lambda = \lambda_0/\Delta$ is the grid sampling density and c_0 is the speed of light in free space. Assuming a grid having the Courant number $S = 1/2$ and there are 20 points per wavelength, then (2.19) yields numerical phase velocity of $0.9969c_0$ representing an error of 0.31%, indicating a phase lag relative to a physical wave propagation in free space. Thus, for every wavelength of travel, the FDTD wave

will accumulate about 1.12 degrees of phase error (0.0031×360). If the sampling density is reduced to 10 points per wavelength, the numerical phase velocity drops to $0.9873c_0$, or about a 1.27% error. As a second-order method, the error in FDTD grid increases by roughly a factor of four when sampling density is halved.

To ensure the numerical stability of the FDTD method, the time increment cannot exceed the Courant limit [24]. For a three-dimensional FDTD lattice, with the lattice space increments $\Delta x \times \Delta y \times \Delta z$, the stability bound is

$$\Delta t \leq \Delta t_{Courant} = \frac{1}{c_0 \sqrt{\frac{1}{(\Delta x)^2} + \frac{1}{(\Delta y)^2} + \frac{1}{(\Delta z)^2}}} \tag{2.20}$$

2.1.4 Parallel implementation of the FDTD method

One of the major limitations of the FDTD method, particularly when applied to electrically large problems, is computational requirements that often exceed the capability of a single processor computer. One solution to overcome this limitation is to use parallel computing to divide the computations over multiple processors in order to reduce the total simulation running time. Fortunately, the FDTD algorithm is well suited for parallelization with only minor changes to the algorithm.

As each field component depends only on the immediately adjacent components, the FDTD lattice can be straightforwardly subdivided into smaller sub-volumes, each within the computational limits of a single processor. Each processor only has to update the section of the grid assigned to it and all processors can update in sync. The fields along the boundaries of the sub-volumes are exchanged every time step, thereby allowing field propagation between the sub-volumes.

To illustrate this solution, Figure 2.2 shows the electric and magnetic field exchanges between processor $n-1$ and n for a TM_z lattice parallelized in the x direction. A single layer of cells overlap on the boundary between processors $n-1$ and n. First, the electric fields are updated in both processors. The updated E_z fields on the left boundary of processor n are sent back to processor $n-1$ and stored on the right boundary. The magnetic fields are then updated in both processors. Now the H_y fields on the right boundary of processor $n-1$ are sent forward to processor n and stored on the left boundary. The E_z fields are then updated, and the field-exchange process is repeated at every time step. This

arrangement allows waves to propagate in both directions between the processors with no spurious reflections or distortions. All processors can update in synch because the update equations only call on stored values on each processor, and on values calculated in the previous half time step already sent/received to/from neighboring processors. It should be noted that, in this example, H_x fields do not need to be exchanged. The efficiency in two-dimensional (2-D) grid can be maximized by exchanging fields in both the x and y directions, which can be treated independently. Also, since each processor has a specific amount of memory, by dividing the FDTD grid onto many processors, there is more total memory available to work with. This process can be readily extended to a 3-D grid.

2.2 Numerical methods for stochastic computations

In this dissertation, we are addressing Earth-ionosphere system that have electrical properties, that vary over location due to the complexity of the system structure and over time due to solar activities, etc. In other words, samples of a particular medium, i.e., Earth and ionosphere, vary when measured from time to time or from point to point in a given area. So in order to take into account the variability of the medium's electrical properties, many measurements from various samples at any given location and at different times should be taken. These samples are averaged to give us the mean of the electrical parameter being measured, i.e., the electric conductivity (σ) when we are referring to isotropic Earth-ionosphere model or the electron density (n_e) when we are referring to anisotropic ionosphere model. Note that in the latter model, two additional parameters, i.e, the ambient Earth's magnetic field $(\mathbf{B})$ and the collision frequency (v_e), should be also considered as uncertainty parameters. Additional data analysis gives the variance (or standard deviation), which tells how much the electrical parameter varies from the mean. When talking about the covariance, we are referring to how two electrical properties vary together. Each of these statistical properties have mathematical definitions as follows.

The mean, which is often referred to as the expectation (defined using E) is defined as

$$E[x] = \mu_x = \sum_{i=1}^{n} x_i f(x_i) \tag{2.21}$$

This is the discrete version with $f(x)$ equal to the probability density. The continuous form is

$$E[x] = \mu_x = \int_{-\infty}^{+\infty} x f(x) dx \tag{2.22}$$

Note that the expectation operator is linear. The variance is often referred to as the mean of the squared difference of each data point from the mean of the data. The discrete form is

$$\mathrm{Var}(x) = \sigma^2(x) = E\left[(x-\mu_x)^2\right] = \sum_{i=1}^{n} (x_i - \mu_x)^2 f(x_i) \tag{2.23}$$

and the continuous form is

$$\mathrm{Var}(x) = \sigma^2(x) = E\left[(x-\mu_x)^2\right] = \int_{-\infty}^{+\infty} (x_i - \mu_x)^2 f(x_i) \tag{2.24}$$

Expanding the expectation operator for the variance yields the following form

$$\begin{aligned} \sigma^2(x) &= E\left[(x-\mu_x)^2\right] \\ &= E\left[x^2 - 2x\mu_x + \mu_x^2\right] \\ &= E\left[x^2\right] - 2\mu_x\mu_x + \mu_x^2 \\ &= E\left[x^2\right] - \mu_x^2 = \mu_{x^2} - \mu_x^2 \end{aligned} \tag{2.25}$$

The square-root of the variance gives the standard deviation $\sigma(x)$. The covariance between two random variables is a measure of how these two variables are related to each other and is defined as

$$\begin{aligned} \mathrm{Cov}(x,y) &= E\left[(x-\mu_x)(y-\mu_y)\right] \\ &= E\left[xy - x\mu_y + \mu_x y + \mu_x\mu_y\right] \\ &= E[xy] - \mu_x\mu_y - \mu_x\mu_y + \mu_x\mu_y \\ &= E[xy] - \mu_x\mu_y = \mu_{xy} - \mu_x\mu_y \end{aligned} \tag{2.26}$$

These definitions of mean (μ), standard deviation (σ) and variance (σ^2) and other statistical properties will be used throughout this dissertation to develop the stochastic equations.

The importance of quantifying uncertainty has been realized for a long time in disciplines such as mechanical engineering, control, power system, etc. Previous studies also highlighted the importance of uncertainty analysis in computational electromagnetics (e.g., [25]–[28]). As a result, many methods have been devised to tackle this issue. The most dominant approach is to treat data uncertainty as random variables or random processes and recast the original deterministic systems as stochastic systems.

2.2.1 Monte Carlo method

One of the most comprehensive and popular methods is Monte Carlo (MC) method or one of its variants, e.g., the Latin hypercube method [29] and the quasi-Monte Carlo method [30]. In MC method, one generates independent realizations of random inputs based on their prescribed probability distribution. The problem becomes deterministic for each realization since the data are fixed. Upon solving the deterministic realizations of the problem, one collects an ensemble of solutions, i.e., realizations of the random solutions. From this ensemble, statistical information (e.g., mean and standard deviation) can be extracted. Although MC method is straightforward to apply, typically it requires a large number of executions, due to the slow convergence of the solution statistics. For example, the mean value typically converges as $1/\sqrt{K}$, where K is the number of realizations [31]. The need for a large number of executions for accurate results can incur an excessive computational burden, especially for complex systems, such as Earth-ionosphere modeling, that are already computationally intensive in their deterministic settings. Still, the Monte Carlo method is the "*gold standard*" for calculation of mean and standard deviation and will be used to verify the validity of the new methods developed in this dissertation.

2.2.2 Perturbation method

The most popular nonsampling methods were perturbation methods, where random fields are expanded around their mean via Taylor series and truncated at a certain order. Typically, at most second-order expansion is employed because the resulting system of equations becomes extremely complicated beyond the second order. An inherent limitation of perturbation methods is that the magnitude of the uncertainties, at both the inputs and outputs, cannot be too large (typically less than 10%); otherwise, the methods do not perform well.

2.2.3 Moment equations

In this approach one attempts to compute the moments of the random solution directly. The unknowns are the moments of the solution, and their equations are derived by taking averages of the original stochastic governing equations. For example, the mean field is determined by the mean of the governing equations. The difficulty lies in the fact that the derivation of a moment almost always, except on some rare occasions, requires

information about higher moments. This brings out the closure problem, which is often dealt with by utilizing some ad hoc arguments about the properties of the higher moments.

2.2.4 Operator-based methods

These methods are based on manipulation of the stochastic operators in the governing equations. They include Neumann expansion, which expresses the inverse of the stochastic operator in a Neumann series [32], and the weighted integral method [33], [34]. Similar to perturbation methods, these operator-based methods are also restricted to small uncertainties. Their applicability is often strongly dependent on the underlying operator and is typically limited to static problems.

2.2.5 Generalized polynomial chaos method

A recently developed method, generalized polynomial chaos (gPC) [35], a generalization of classical polynomial chaos [36], has become one of the most widely used methods. With gPC, stochastic solutions are expressed as orthogonal polynomials of the input random parameters, and different types of orthogonal polynomials can be chosen to achieve better convergence. It is essentially a spectral representation in random space and exhibits fast convergence when the solution depends smoothly on the random parameters. gPC-based method will be one of the two primary tools for uncertainty analysis in this dissertation.

Upon choosing a proper basis, a numerical technique is needed to solve the problem. The early work was mostly based on the Galerkin method, which minimizes the error of a finite-order gPC expansion by Galerkin projection. This is the stochastic Galerkin (SG) approach and has been applied since the early work on PC and proved to be effective. The Galerkin procedure usually results in a set of coupled deterministic equations and requires additional effort to solve. Also, the derivation of the resulting equations can be challenging when the governing stochastic equations take complicated forms.

Another numerical approach is the stochastic collocation (SC) method, where one repetitively excecutes an established deterministic code on a prescribed node in the random space defined by the random inputs. Upon completing the simulations, one conducts postprocessing to obtain the desired solution properties from the solution ensemble.

A detailed comparison between the Galerkin method and the stochastic collocation

method can be found in [37, pp. 87-88]. In this dissertation, the Galerkin method is chosen since this approach ensures that the residue of the stochastic governing equations is orthogonal to the linear space spanned by the gPC polynomials, and therefore the accuracy is optimal. On the other hand, all of the existing collocation methods require the solution of a much larger number of equations than that required by the gPC Galerkin method, especially for higher-dimensional random spaces.

2.2.5.1 Mathematical formulation

A general random process $g(\theta)$, depending on random event θ, can be represented as

$$\begin{aligned} g(\theta) = a_0\psi_0 &\\ &+ \sum_{i_1=1}^{\infty} c_{i_1}\psi_1(\zeta_{i_1}(\theta)) \\ &+ \sum_{i_1=1}^{\infty}\sum_{i_2=1}^{i_1} c_{i_1 i_2}\psi_2(\zeta_{i_1}(\theta),\zeta_{i_2}(\theta)) \\ &+ \sum_{i_1=1}^{\infty}\sum_{i_2=1}^{i_1}\sum_{i_3=1}^{i_2} c_{i_1 i_2 i_3}\psi_3(\zeta_{i_1}(\theta),\zeta_{i_2}(\theta),\zeta_{i_3}(\theta)) \\ &+ \dots \end{aligned} \tag{2.27}$$

where $\psi_n(\zeta_{i_1},\dots,\zeta_{i_n})$ denotes the generalized polynomial chaos of order n in terms of the random vector $\boldsymbol{\zeta} = (\zeta_{i_1},\dots,\zeta_{i_n})$. It should be noted that equation (2.27) involves an infinite summation, which is often truncated to finite order. The expansion bases ψ_n are multidimensional polynomials defined as tensor-products of the corresponding one-dimensional polynomials ϕ_m. For notational convenience, equation (2.27) is rewritten as

$$g(\theta) = \sum_{m=0}^{\infty} c_m\Phi_m(\boldsymbol{\zeta}) \tag{2.28}$$

where there is a one-to-one correspondence between the coefficients and polynomial basis in (2.27) and (2.28).

The polynomials Φ_m are a set of orthogonal polynomials satisfying the orthogonality conditions

$$\langle\Phi_m(\boldsymbol{\zeta})\Phi_n(\boldsymbol{\zeta})\rangle = \langle\Phi_m^2(\boldsymbol{\zeta})\rangle\,\delta_{mn} \tag{2.29}$$

where δ_{mn} is the Kronecker delta and the angled bracket denotes the inner product operation defined in the Hilbert space of the random vector $\boldsymbol{\zeta}$ expressed as

$$\langle f(\boldsymbol{\zeta})g(\boldsymbol{\zeta})\rangle = \int_{\Gamma} f(\boldsymbol{\zeta})g(\boldsymbol{\zeta})\rho(\boldsymbol{\zeta})d\boldsymbol{\zeta} \tag{2.30}$$

or

$$\langle f(\zeta)g(\zeta)\rangle = \sum_{\zeta} f(\zeta)g(\zeta)\rho(\zeta) \tag{2.31}$$

in the discrete case. The probability density function $\rho(\zeta)$ serves as the role of integration weight, which in turn dictates the choice of orthogonal polynomials $\Phi_m(\zeta)$. For example, if ζ corresponds to uniformly distributed variables, the probability density function $\rho(\zeta)$ defines Legendre polynomials. Similarly, a Beta distribution defines Jacobi polynomials. It is noted that most of the common distributions are associated with corresponding orthogonal polynomials. Some of the well known correspondences are listed in Table 2.1.

2.2.5.2 Galerkin projection

In this Section, we present the gPC Galerkin method to solve stochastic equation, which is rewritten here for clarity

$$\mathcal{L}(\mathbf{x}, t, \theta; g) = f(\mathbf{x}, t; \theta) \tag{2.32}$$

where $g = g(\mathbf{x}, t, \theta)$ is the solution and $f(\mathbf{x}, t, \theta)$ is the source term. Operator $\mathcal{L}$ generally involves differentiations in space/time and can be nonlinear. Appropriate initial and boundary conditions are assumed. The existence of random parameter θ is due to the introduction of uncertainty into the system via boundary conditions, initial conditions, material properties, etc. The solution g, which is regarded as a random process, can be expanded by the Wiener-Askey polynomial chaos as

$$g(\mathbf{x}, t; \theta) = \sum_{i=0}^{P} g_i(\mathbf{x}, t)\Phi_i(\zeta(\theta)) \tag{2.33}$$

Note here the infinite summation has been truncated at the finite term P. The above representation can be considered as a spectral expansion in the random dimension θ, and the random trial basis Φ_i is the Askey-scheme-based orthogonal polynomials discussed in the previous Section. The total number of expansion terms is $(P+1)$, and is determined by the dimension (n) of random variable and the highest order (p) of the polynomials

$$P + 1 = \frac{(n+p)!}{n!p!} \tag{2.34}$$

Upon substituting equation (2.33) into the governing equation (2.32), we obtain

$$\mathcal{L}\left(\mathbf{x}, t, \theta; \sum_{i=0}^{P} g_i(\mathbf{x}, t)\Phi_i(\zeta(\theta))\right) = f(\mathbf{x}, t; \theta) \tag{2.35}$$

A Galerkin projection of the above equation onto each polynomial basis Φ_i is then conducted in order to ensure the error is orthogonal to the functional space spanned by the finite-dimensional basis Φ_i

$$\left\langle \mathcal{L}\left(\mathbf{x}, t, \theta; \sum_{i=0}^{P} g_i(\mathbf{x}, t)\Phi_i(\boldsymbol{\zeta}(\theta))\right)\right\rangle = \langle f(\mathbf{x}, t; \theta)\rangle\,, \qquad k = 0, 1, \ldots, P \tag{2.36}$$

By using the orthogonality of the polynomial basis, we can obtain a set of $(P+1)$ coupled equations for each random mode $g_i(\mathbf{x}, t)$ where $i = \{0, 1, \ldots, P\}$. It should be noted that by utilizing the Wiener-Askey polynomial chaos expansion (2.33), the randomness is effectively transferred into the basis polynomials. Thus, the governing equations for the expansion coefficients g_i resulted from equation (2.36) are deterministic. Discretizations in space $\mathbf{x}$ and time t can be carried out by any conventional deterministic techniques, i.e., the FDTD is focused in this dissertation.

2.2.5.3 Stochastic information of solutions

Once the coupled equations (2.36) are solved and the expansion coefficients g_i are available, one has in fact established an analytical expression of the stochastic solution $g(\mathbf{x}, t; \theta)$ in terms of the random inputs θ. To this end, almost all of the stochastic information can be extracted from the gPC expansion in a straightforward way and with minimal computational cost, based on analytical evaluations.

Assume the stochastic solution $g(\mathbf{x}, t; \theta)$ in equation (2.32) is available. Keep in mind that for real random variables X and Y, the expected value of their product is an inner product, i.e., $E[XY] = \langle X, Y\rangle$. Therefore, two of the most important statistical moments, mean and variance, can be calculated as

$$\begin{aligned}\mu_g = E[g(\mathbf{x}, t; \theta)] &= \sum_{i=0}^{P} g_i(\mathbf{x}, t)\,\langle\Phi_i(\boldsymbol{\zeta}(\theta))\rangle \\ &= \sum_{i=0}^{P} g_i(\mathbf{x}, t)\delta_{m0} = g_0(\mathbf{x}, t)\end{aligned} \tag{2.37}$$

and

$$\begin{aligned}\sigma_g^2 = E[g^2(\mathbf{x}, t; \theta)] - \mu_g &= \sum_{i=0}^{P} g_i^2(\mathbf{x}, t)\,\langle\Phi_i^2(\boldsymbol{\zeta}(\theta))\rangle - g_0^2(\mathbf{x}, t) \\ &= \sum_{i=1}^{P} g_i^2(\mathbf{x}, t)\,\langle\Phi_i^2(\boldsymbol{\zeta}(\theta))\rangle\end{aligned} \tag{2.38}$$

2.2.6 Delta method

Another stochastic evaluation method is the delta method which could be considered to be a subset of the perturbation methods [38], because it also uses a truncated Taylor series expansion to determine the mean and the variance of functions of random variables. The delta method is used to derive the stochastic FDTD approach, namely S-FDTD, for magnetized cold plasma modeling in this dissertation. Suitably truncated, this series is substituted into the equation being approximated; the equation is expanded; and the coefficients of the Taylor series are determined via linear algebra. This Section provides the basic formulation of the delta method derivation of the mean and variance, respectively, of a generic function of multiple random variables.

2.2.6.1 Mean of a generic multivariable function

We begin with the Taylor's series expansion of a generic function, g, of stochastic variables $x_1, x_2, ..., x_n$

$$g(x_1, x_2, \ldots, x_n) = g(\mu_{x_1}, \mu_{x_2}, \ldots, \mu_{x_n}) + \sum_{i=1}^{n} \left.\frac{\partial g}{\partial x_i}\right|_{\mu_{x_1},\ldots,\mu_{x_n}} (x_i - \mu_{x_i}) + \frac{1}{2!}\sum_{i=1}^{n}\sum_{j=1}^{n} \left.\frac{\partial^2 g}{\partial x_i \partial x_j}\right|_{\mu_{x_1},\ldots,\mu_{x_n}} (x_i - \mu_{x_i})\left(x_j - \mu_{x_j}\right) + \ldots \tag{2.39}$$

Here, the mean of the i^{th} stochastic variable is denoted as x_i, and in Chapter 5, the function, g, will be obtained from the FDTD time-stepping expressions for E, H, and J. Now, taking the expectation of (2.39) and applying the linearity of the expectation operator gives

$$\begin{aligned} E[g(x_1, x_2, \ldots, x_n)] = {} & E[g(\mu_{x_1}, \mu_{x_2}, \ldots, \mu_{x_n})] \\ & + E\left[\sum_{i=1}^{n} \left.\frac{\partial g}{\partial x_i}\right|_{\mu_{x_1},\ldots,\mu_{x_n}} (x_i - \mu_{x_i})\right] \\ & + E\left[\frac{1}{2!}\sum_{i=1}^{n}\sum_{j=1}^{n} \left.\frac{\partial^2 g}{\partial x_i \partial x_j}\right|_{\mu_{x_1},\ldots,\mu_{x_n}} (x_i - \mu_{x_i})\left(x_j - \mu_{x_j}\right)\right] \\ & + \ldots \end{aligned} \tag{2.40}$$

Several terms in (2.40) go to zero. For example, $E[x_i - \mu_{x_i}] = E[x_i] - E[x_i] = 0$, recognizing that expectation is a linear operator having the distributive property, and the

expectation of a constant is a constant. Noting also that $E[ax] = aE[x]$. Equation (2.40) can now be simplified to

$$\begin{aligned} E[g(x_1, x_2, \ldots, x_n)] &= g(\mu_{x_1}, \mu_{x_2}, \ldots, \mu_{x_n}) \\ &+ \sum_{i=1}^{n} \left.\frac{\partial g}{\partial x_i}\right|_{\mu_{x_1},\ldots,\mu_{x_n}} E\left[x_i - \mu_{x_i}\right] + \frac{1}{2!}\sum_{i=1}^{n}\sum_{j=1}^{n} \left.\frac{\partial^2 g}{\partial x_i \partial x_j}\right|_{\mu_{x_1},\ldots,\mu_{x_n}} E\left[\left(x_i - \mu_{x_i}\right)\left(x_j - \mu_{x_j}\right)\right] \\ &+ \ldots \end{aligned} \tag{2.41}$$

Neglecting higher-order terms removes the double-sum in (2.41), thus yielding

$$E[g(x_1, x_2, \ldots, x_n)] = g(\mu_{x_1}, \mu_{x_2}, \ldots, \mu_{x_n}) \tag{2.42}$$

Equation (2.42) is the mathematical verification of the traditional FDTD approachnamely, the average (or expected) fields on the left-hand side of (2.42) can be found by solving the field equations using the means or averages of the variables on the right-hand side of (2.42). Thus, the equations for the mean values of the fields in the S-FDTD method are the traditional FDTD field equation updates. The usual FDTD field values are now recognized to be the mean field values, and can be found by inputting the mean electrical properties.

2.2.6.2 Variance of a generic multivariable function

We now turn our attention to finding the variance of a generic multivariable function, $\sigma^2(g)$, defined as

$$\sigma^2\left\{g(x_1, x_2, \ldots, x_n)\right\} = E[g^2(x_1, x_2, \ldots, x_n)] - E^2[g(x_1, x_2, \ldots, x_n)] \tag{2.43}$$

To obtain the first term on the right-hand side, namely $E[g^2(x_1, x_2, \ldots, x_n)]$, we first find $g^2(x_1, x_2, \ldots, x_n)$ by squaring (2.39), the Taylor's series expansion of $g(x_1, x_2, \ldots, x_n)$. Retaining only terms through second-order, this yields

$$\begin{aligned} g^2(x_1, x_2, \ldots, x_n) &= g^2(\mu_{x_1}, \mu_{x_2}, \ldots, \mu_{x_n}) \\ &+ 2g(\mu_{x_1}, \mu_{x_2}, \ldots, \mu_{x_n}) \sum_{i=1}^{n} \left.\frac{\partial g}{\partial x_i}\right|_{\mu_{x_1},\ldots,\mu_{x_n}} \left(x_i - \mu_{x_i}\right) \\ &+ \sum_{i=1}^{n}\sum_{j=1}^{n} \left.\frac{\partial g}{\partial x_i}\frac{\partial g}{\partial x_j}\right|_{\mu_{x_1},\ldots,\mu_{x_n}} \left(x_i - \mu_{x_i}\right)\left(x_j - \mu_{x_j}\right) \\ &+ \frac{2}{2!} g(\mu_{x_1}, \mu_{x_2}, \ldots, \mu_{x_n}) \sum_{i=1}^{n}\sum_{j=1}^{n} \left.\frac{\partial^2 g}{\partial x_i \partial x_j}\right|_{\mu_{x_1},\ldots,\mu_{x_n}} \left(x_i - \mu_{x_i}\right)\left(x_j - \mu_{x_j}\right) \\ &+ \ldots \end{aligned} \tag{2.44}$$

Taking the expectation of this equation yields

$$\begin{aligned}
E[g^2(x_1, x_2, \ldots, x_n)] &= E[g^2(\mu_{x_1}, \mu_{x_2}, \ldots, \mu_{x_n})] \\
&+2g(\mu_{x_1}, \mu_{x_2}, \ldots, \mu_{x_n}) \sum_{i=1}^{n} \frac{\partial g}{\partial x_i}\bigg|_{\mu_{x_1},\ldots,\mu_{x_n}} E\left[x_i - \mu_{x_i}\right] \\
&+ \sum_{i=1}^{n}\sum_{j=1}^{n} \frac{\partial g}{\partial x_i}\frac{\partial g}{\partial x_j}\bigg|_{\mu_{x_1},\ldots,\mu_{x_n}} E[(x_i - \mu_{x_i})\left(x_j - \mu_{x_j}\right)] \\
&+ \frac{2}{2!} g(\mu_{x_1}, \mu_{x_2}, \ldots, \mu_{x_n}) \sum_{i=1}^{n}\sum_{j=1}^{n} \frac{\partial^2 g}{\partial x_i \partial x_j}\bigg|_{\mu_{x_1},\ldots,\mu_{x_n}} E[(x_i - \mu_{x_i})\left(x_j - \mu_{x_j}\right)] \\
&+ \ldots
\end{aligned} \tag{2.45}$$

Terms containing expressions such as $E[x_i - \mu_{x_i}]$ go to zero as discussed previously, leaving the following equation

$$\begin{aligned}
E[g^2(x_1, x_2, \ldots, x_n)] &= g^2(\mu_{x_1}, \mu_{x_2}, \ldots, \mu_{x_n}) \\
&+ \sum_{i=1}^{n}\sum_{j=1}^{n} \frac{\partial g}{\partial x_i}\frac{\partial g}{\partial x_j}\bigg|_{\mu_{x_1},\ldots,\mu_{x_n}} E[(x_i - \mu_{x_i})\left(x_j - \mu_{x_j}\right)] \\
&+ \frac{2}{2!} g(\mu_{x_1}, \mu_{x_2}, \ldots, \mu_{x_n}) \sum_{i=1}^{n}\sum_{j=1}^{n} \frac{\partial^2 g}{\partial x_i \partial x_j}\bigg|_{\mu_{x_1},\ldots,\mu_{x_n}} E[(x_i - \mu_{x_i})\left(x_j - \mu_{x_j}\right)] \\
&+ \ldots
\end{aligned} \tag{2.46}$$

Next, to obtain the second term on the right-hand side of (2.43), we square (2.41). This yields

$$\begin{aligned}
E^2[g(x_1, x_2, \ldots, x_n)] &= g^2(\mu_{x_1}, \mu_{x_2}, \ldots, \mu_{x_n}) \\
&+ \frac{2}{2!} g(\mu_{x_1}, \mu_{x_2}, \ldots, \mu_{x_n}) \sum_{i=1}^{n}\sum_{j=1}^{n} \frac{\partial^2 g}{\partial x_i \partial x_j}\bigg|_{\mu_{x_1},\ldots,\mu_{x_n}} E[(x_i - \mu_{x_i})\left(x_j - \mu_{x_j}\right)] \\
&+ \left\{ \frac{1}{2!} \sum_{i=1}^{n}\sum_{j=1}^{n} \frac{\partial^2 g}{\partial x_i \partial x_j}\bigg|_{\mu_{x_1},\ldots,\mu_{x_n}} E[(x_i - \mu_{x_i})\left(x_j - \mu_{x_j}\right)] \right\}^2 \\
&+ \ldots
\end{aligned} \tag{2.47}$$

Subtracting (2.47) from (2.46) and removing the higher order terms, we obtain an approximation for the variance of function g

$$\sigma^2\left\{g(x_1, x_2, \ldots, x_n)\right\} \approx \sum_{i=1}^{n}\sum_{j=1}^{n} \frac{\partial g}{\partial x_i}\frac{\partial g}{\partial x_j}_{\mu_{x_1},\ldots,\mu_{x_n}} E\left[(x_i - \mu_{x_i})\left(x_j - \mu_{x_j}\right)\right] \tag{2.48}$$

Putting this equation in terms of the covariance

$$\sigma^2\left\{g(x_1,x_2,\ldots,x_n)\right\} \approx \sum_{i=1}^{n}\sum_{j=1}^{n}\frac{\partial g}{\partial x_i}\frac{\partial g}{\partial x_j}_{\mu_{x_1},\ldots,\mu_{x_n}} \mathrm{Cov}(x_i,x_j) \tag{2.49}$$

At this point we have derived two important approximate relations: equation (2.42) for the mean, and equation (2.49) for the variance, of a generic function g of random variables $(x_1,x_2,\ldots,x_n)$, all based on truncated Taylor-series expansions. Before applying these relations to develop the S-FDTD algorithm in Chapter 5, it is useful to recall three fundamental identities regarding the random variables, x and y. First, the variance of $x \pm y$ is

$$\sigma^2(x \pm y) = \sigma^2(x) + \sigma^2(y) \pm 2\mathrm{Cov}(x,y) \tag{2.50}$$

Second, the variance of x scaled by the constant, a

$$\sigma^2(ax) = a^2\sigma^2(x) \tag{2.51}$$

And third, the covariance identity

$$\mathrm{Cov}(x,y) = \rho(x,y)\sigma(x)\sigma(y) \tag{2.52}$$

In the covariance identity, the two terms $\sigma(x)$ and $\sigma(y)$ are the standard deviations of x and y, and $\rho(x,y)$ is the correlation coefficient of these two random variables. This correlation is bounded between $[-1,1]$.

Table 2.1: Correspondence between the probability distribution and the type of gPC polynomial basis ($N \geq 0$ is a finite integer).

Type	Distribution	gPC Basis polynomials	Support
Continuous	Gaussian	Hermite	$(-\infty,\infty)$
	Gamma	Laguerre	$[0,\infty)$
	Beta	Jacobi	$[a,b]$
	Uniform	Legendre	$[a,b]$
Discrete	Poison	Charlier	$\{0,1,2,...\}$
	Binomial	Krawtchouk	$\{0,1,...,N\}$
	Negative Binomial	Meixner	$\{0,1,2,...\}$
	Hypergeometric	Hahn	$\{0,1,...,N\}$

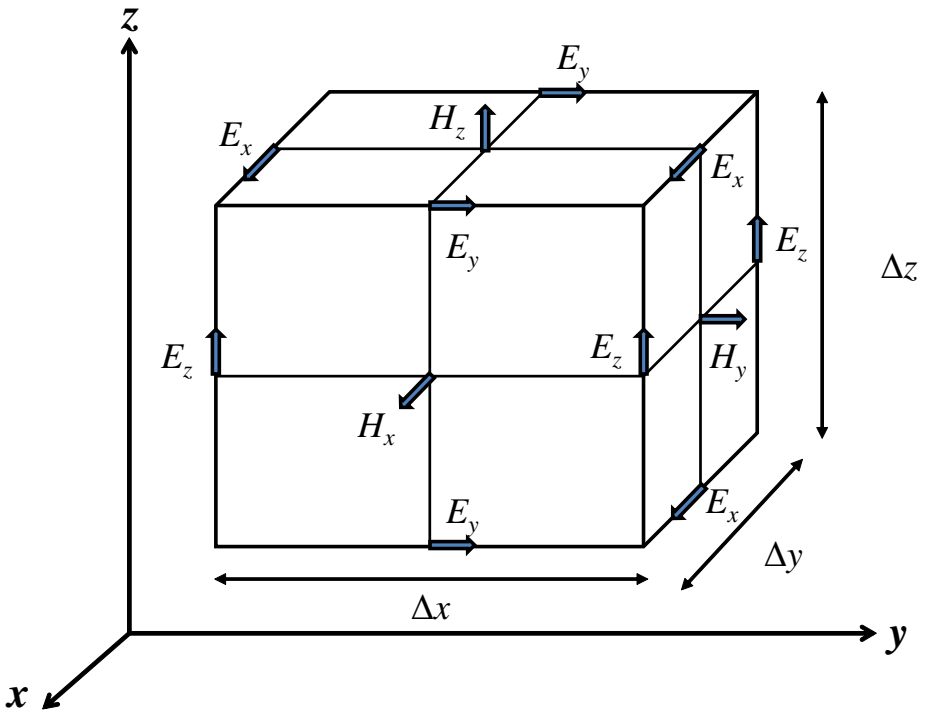

Figure 2.1: Positions of the field components in a unit cell of the Yee lattice.

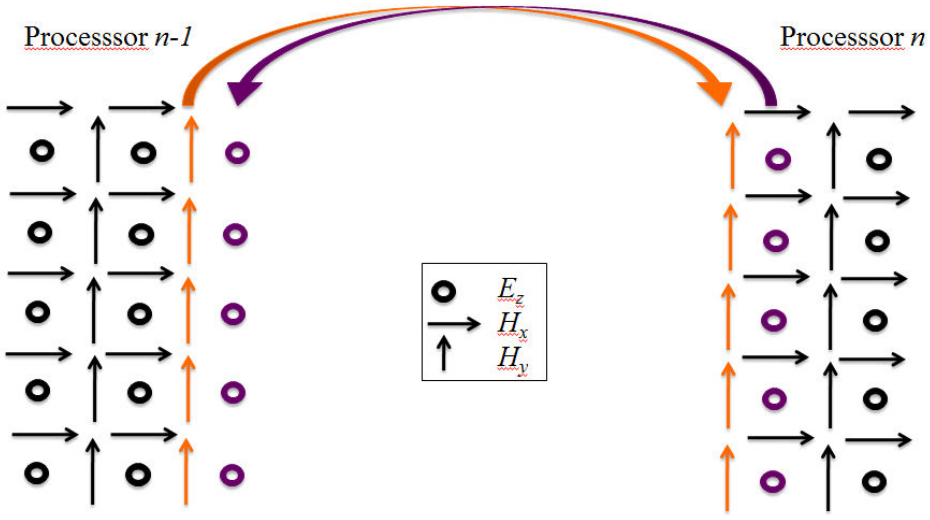

Figure 2.2: TM_z parallelization with field exchange in the x direction.

CHAPTER 3

IONOSPHERIC VARIABILITY EFFECTS ON IMPULSIVE ELF ANTIPODAL PROPAGATION ABOUT THE EARTH-SPHERE

3.1 Introduction

The ionosphere and the Earth's ground form a spherical annular cavity in which extremely low-frequency (ELF: 3 Hz - 3 kHz) electromagnetic waves propagate on a global scale. Accurate models of ELF wave propagation in the Earth-ionosphere waveguide are helpful for studying lightning and sprites, global temperature change, hypothesized earthquake precursors, remote sensing, and communications, as well as other geophysical phenomena and engineering applications (e.g., [39]–[42]).

Analytical and numerical models have been developed to study ELF propagation. Most analytical approaches are based on ray theory for short distant propagation and mode theory for long distant propagation (e.g., [43]–[45]). Alternatively, the transmission line method has been used (e.g., [46], [47]). In general, analytical methods are very fast and computationally efficient, however they can only provide solutions for specific scenarios wherein simplifying assumptions have been made (such as ignoring much of the Earth's topographical details and ionospheric inhomogeneity). More recently, numerical methods have been developed to take advantage of modern supercomputing capabilities via a high-resolution spatial mesh of grid cells that may be assigned to the varying electrical details of the lithosphere, ionosphere, and oceans. The finite-difference time-domain (FDTD) method [2] is particularly attractive for this problem (e.g., [7], [9], [20], [48]–[52]).

Analytical and numerical solutions to ELF electromagnetic wave propagation in the Earth-ionosphere waveguide nearly always assume average (mean) material properties at each position of interest and only solve for the average (mean) electric and magnetic fields. However, numerically assuming only an average state of the ionosphere yields calculated

output electromagnetic field waveforms that are not as rich and complex as measured electromagnetic fields. Further, there is great uncertainty in the content of the ionosphere at any given moment.

The continual fluctuation of the state of the ionosphere has resulted in the generation of many different ionosphere conductivity models over time (e.g., [53]–[57]). Three observations may be made about these various conductivity models: (1) There are notable differences between these models because different methodologies and approaches are used to generate them. (2) These models cannot be adequately verified because there is little experimental data on the ionosphere conductivity within the altitude range of $50 - 100$ km (which is a crucial range for ELF propagation). This range is inaccessible by most modern remote sensing equipment since it is too high for balloons and airplanes, but too low for satellites. (3) All of these models are static with time, so they do not reproduce a realistic ionosphere conductivity that constantly changes over time with solar activity. There are some other models that change with time, such as the International Reference Ionosphere (IRI), but these provide only the background ionosphere's electron density profile and its variation [58]–[60]. Note that ionosphere conductivity may be directly converted from the ionosphere's electron density.

Instead of assuming an average ionospheric state, a more comprehensive and realistic approach is to treat the ionosphere as a random medium and account for the variation of its conductivity. However, to account for the ionosphere's conductivity uncertainties brings a significant additional computational cost. The easiest and most traditional approach is the well-known Monte Carlo (MC) method in which a large set of simulations with different samples of the random parameters is used to collect quantitative information on the statistical behavior of the model. A deterministic simulation of wave propagation in the Earth-ionosphere cavity may takes hours/days for many scenarios even with the support of supercomputers, this turns out to be extremely inefficient when applying the MC method as it requires large simulation times and thus prevent us from its application to the analysis of complex realistic ionosphere structures. Therefore, the requirement of computational efficiency is recognized as a critical aspect in context with the Earth-ionosphere modeling.

In this chapter, the polynomial chaos expansion (PCE) technique is used to efficiently

account for the variability of the ionosphere conductivity in a global FDTD Earth-ionosphere waveguide model. Specifically the Galerkin-based PCE technique is used to assume a series of orthogonal polynomials of random variables for the description of the solution in a stochastic dynamical system. The PCE is a widely used method within uncertainty quantification area and has been successfully applied to various types of problems (e.g., [28], [61]–[63]). The proposed numerical technique is capable of treating the ionospheres complicated structure while keeping the computation cost reasonable. It is important to note that the method is particularly efficient when a small number of random input parameters is used in a large simulation, making the use of the direct method such as Monte Carlo simulation infeasible.

3.2 Mathematical description

This Section first provides a brief overview of the most important aspects of the global FDTD Earth-ionosphere waveguide model relevant to understanding the stochastic version. Section 3.2.2 describes the corresponding stochastic global FDTD algorithm that uses the Galerkin-based polynomial chaos expansion method to take into account the variations of the ionospheric conductivity layers. Note that the formulations are derived here for only the Northern hemisphere. The algorithm for the Southern hemisphere may be derived in an analogous manner. Finally, Section 3.2.3 describes the methodology for calculating the global sensitivities of each input parameter on the electromagnetic fields.

3.2.1 Deterministic model - Global FDTD update equations (Northern hemisphere)

The grid is comprised of isosceles trapezoidal cells away from the North and South poles and isosceles triangular cells at the poles as shown in Figure 3.1. We set M cells in θ-direction (the south-to-north direction), $2M$ cells in ϕ-direction (the west-to-east direction) in order to maintain square or nearly square grid cells near the equator, and K cells in the r-direction (the radial direction that extends -100 km (below) to $+110$ km (above) sea level. The indexes of the E and H fields extend over the following ranges

$$H_\phi(1,1,1) \rightarrow H_\phi(2M, M-1, K+1)$$
$$H_\theta(1,1,1) \rightarrow H_\theta(2M+1, M, K+1)$$
$$H_r(1,1,1) \rightarrow H_r(2M+1, M-1, K)$$
$$H_{r,Npole/Spole}(1) \rightarrow H_{r,Npole/Spole}(K)$$
$$E_\phi(1,1,1) \rightarrow E_\phi(2M+1, M, K)$$
$$E_\theta(1,1,1) \rightarrow E_\theta(2M, M-1, K)$$
$$E_r(1,1,1) \rightarrow E_r(2M, M, K+1)$$

The lattice space increments are $\Delta^{j,k}_{w-e} = \pi R_k \sin\left[(M-j+1)\frac{\pi}{M}\right]/M$, $\Delta^k_{s-n} = \pi R_k/M$, and Δr, with R_k is the Earth's radius regarding to k-cell in r-direction [9]. The space-cell eccentricity increases upon approaching either the North or South poles, which would reduce the allowable time step since the Courant stability limit is determined by the smallest cell dimensions in the grid. To effectively mitigate this problem, pairs of adjacent cells in the West-East direction are merged several times as the grid approaches either Pole from the Equator, specifically at latitudes wherein $\Delta^k_{s-n}/\Delta^{j,k}_{w-e} \geq 2$. The illustration of merging cells is also shown in Figure 3.1. Finally, a periodic boundary condition is applied to the H_θ and H_r field components along the 2-D slices of cells (over the j and r directions) at $i = 1$ and $i = 2M+1$. Readers are encouraged to refer to Reference [9] for more details.

3.2.1.1 H-field update

Referring to Figure 3.1 a regular H_ϕ-field update is

$$\begin{aligned} H_\phi|^{n+1/2}_{i+1/2,j,k} = H_\phi|^{n-1/2}_{i+1/2,j,k} &+ DB_{\phi 1}\left(E_\theta|^n_{i+1/2,j,k+1/2} - E_\theta|^n_{i+1/2,j,k-1/2}\right) \\ &- DB^k_{\phi 2}\left(E_r|^n_{i+1/2,j+1/2,k} - E_r|^n_{i+1/2,j-1/2,k}\right) \end{aligned} \tag{3.1}$$

where

$$DB_{\phi 1} = \frac{\Delta t}{\mu_0 \Delta r} \quad \text{and} \quad DB^k_{\phi 2} = \frac{\Delta t}{\mu_0 \Delta^k_{s-n}}$$

For a trapezoidal merging-cell H_ϕ-field update, the left and right H_ϕ at the bottom of the merging cell require separate update equations as follows (the regular update equation (3.1) for the H_ϕ may be applied at the top of the merging cell)

$$H_\phi|^{n+1/2}_{i+1/2,j+1,k} = H_\phi|^{n-1/2}_{i+1/2,j,k} + DB_{\phi 1}\left(E_\theta|^n_{i+1/2,j+1,k+1/2} - E_\theta|^n_{i+1/2,j+1,k-1/2}\right) - DB^k_{\phi 2}\left(\frac{3E_r|^n_{i+1,j+3/2,k} + E_r|^n_{i-1,j+3/2,k}}{4} - E_r|^n_{i+1/2,j+1/2,k}\right) \tag{3.2}$$

$$H_\phi|^{n+1/2}_{i+3/2,j+1,k} = H_\phi|^{n-1/2}_{i+3/2,j,k} + DB_{\phi 1}\left(E_\theta|^n_{i+3/2,j+1,k+1/2} - E_\theta|^n_{i+3/2,j+1,k-1/2}\right) - DB^k_{\phi 2}\left(\frac{3E_r|^n_{i+1,j+3/2,k} + E_r|^n_{i+3,j+3/2,k}}{4} - E_r|^n_{i+3/2,j+1/2,k}\right) \tag{3.3}$$

The H_ϕ-field update for triangular cells is analogous to (3.1), (3.2), and (3.3) (depending on whether or not a merging of cells occurs at the latitude of the triangular cells immediately adjacent to the Poles).

Next, the H_θ-field updates for regular, merging cell, and triangular cells are identical, and is as follows

$$H_\theta|^{n+1/2}_{i,j+1/2,k} = H_\theta|^{n-1/2}_{i,j+1/2,k} + DB^{j+1/2,k}_{\theta 1}\left(E_r|^n_{i+1/2,j+1/2,k} - E_r|^n_{i-1/2,j+1/2,k}\right) - DB_{\theta 2}\left(E_\phi|^n_{i,j+1/2,k+1/2} - E_\phi|^n_{i,j+1/2,k-1/2}\right) \tag{3.4}$$

where

$$DB^{j+1/2,k}_{\theta 1} = \frac{\Delta t}{\mu_0 \Delta^{j+1/2,k}_{w-e}} \quad \text{and} \quad DB_{\theta 2} = \frac{\Delta t}{\mu_0 \Delta r}$$

The regular H_r-field update is

$$\begin{aligned} H_r|^{n+1/2}_{i,j,k+1/2} &= H_r|^{n-1/2}_{i,j,k+1/2} \\ &+ DB^{k+1/2}_{r1}\left(E_\phi|^n_{i,j+1/2,k+1/2}\frac{\Delta^{j+1/2,k+1/2}_{w-e}}{\Delta^{j,k+1/2}_{w-e}} - E_\phi|^n_{i,j-1/2,k+1/2}\frac{\Delta^{j-1/2,k+1/2}_{w-e}}{\Delta^{j,k+1/2}_{w-e}}\right) \\ &- DB^{j,k+1/2}_{r2}\left(E_\theta|^n_{i+1/2,j,k+1/2} - E_\theta|^n_{i-1/2,j,k+1/2}\right) \end{aligned} \tag{3.5}$$

where

$$DB^{k+1/2}_{r1} = \frac{\Delta t}{\mu_0 \Delta^{k+1/2}_{s-n}} \quad \text{and} \quad DB^{j,k+1/2}_{r2} = \frac{\Delta t}{\mu_0 \Delta^{j,k+1/2}_{w-e}}$$

For trapezoidal merging cells, only the middle H_r-fields at bottom of the merging cells require new update equation as shown below

$$\begin{aligned} H_r|^{n+1/2}_{i+1,j+1,k+1/2} &= H_r|^{n-1/2}_{i+1,j+1,k+1/2} + DB^{k+1/2}_{r1} \\ &\times \left(\frac{E_\phi|^n_{i+2,j+3/2,k+1/2} + E_\phi|^n_{i,j+3/2,k+1/2}}{2}\frac{\Delta^{j+3/2,k+1/2}_{w-e}}{\Delta^{j+1,k+1/2}_{w-e}} - E_\phi|^n_{i+1,j+1/2,k+1/2}\frac{\Delta^{j+1/2,k+1/2}_{w-e}}{\Delta^{j+1,k+1/2}_{w-e}}\right) \\ &- DB^{j+1,k+1/2}_{r2}\left(E_\theta|^n_{i+3/2,j+1,k+1/2} - E_\theta|^n_{i+1/2,j+1,k+1/2}\right) \end{aligned} \tag{3.6}$$

The H_r-field update at the North pole is

$$H_{r,Npole}|^{n+1/2}_{1,M+1,k+1/2} = H_{r,Npole}|^{n-1/2}_{1,M+1,k+1/2} - \frac{4\tan(\pi/N)\Delta t}{N\Delta^{M+1/2,k+1/2}_{w-e}\mu_0}\sum_{X=1}^{N} E_\phi|^n_{X,M+1/2,k+1/2} \tag{3.7}$$

3.2.1.2 E-field update

Similarly, referring to Figure 3.1, the regular E_ϕ-field update is

$$\begin{aligned} E_\phi|^{n+1}_{i,j+1/2,k+1/2} &= CA^{i,j+1/2,k+1/2}_\phi E_\phi|^n_{i,j+1/2,k+1/2} \\ &+CB^{i,j+1/2,k+1/2}_{\phi 1}\left(H_r|^{n+1/2}_{i,j+1,k+1/2} - H_r|^{n+1/2}_{i,j,k+1/2}\right) \\ &-CB^{i,j+1/2,k+1/2}_{\phi 2}\left(H_\theta|^{n+1/2}_{i,j+1/2,k+1} - H_\theta|^{n+1/2}_{i,j+1/2,k}\right) \end{aligned} \tag{3.8}$$

where

$$CA^{i,j+1/2,k+1/2}_\phi = \frac{1-\frac{\sigma_{i,j+1/2,k+1/2}\Delta t}{2\epsilon_0}}{1+\frac{\sigma_{i,j+1/2,k+1/2}\Delta t}{2\epsilon_0}}, \quad CB^{i,j+1/2,k+1/2}_{\phi 1} = \frac{\frac{\Delta t}{\epsilon_0\Delta^{k+1/2}_{s-n}}}{1+\frac{\sigma_{i,j+1/2,k+1/2}\Delta t}{2\epsilon_0}},$$

$$\text{and} \quad CB^{i,j+1/2,k+1/2}_{\phi 2} = \frac{\frac{\Delta t}{\epsilon_0\Delta r}}{1+\frac{\sigma_{i,j+1/2,k+1/2}\Delta t}{2\epsilon_0}}$$

Equation (3.8) will be also used for trapezoidal merging cells and triangular cells E_ϕ-field updates.

Next, similar with the H_θ update, all the E_θ-field updates for regular cells, trapezoidal merging cell or triangular cell use identical update equation given by

$$\begin{aligned} E_\theta|^{n+1}_{i+1/2,j,k+1/2} &= CA^{i+1/2,j,k+1/2}_\theta E_\theta|^n_{i+1/2,j,k+1/2} \\ &+CB^{i+1/2,j,k+1/2}_{\theta 1}\left(H_\phi|^{n+1/2}_{i+1/2,j,k+1} - H_\phi|^{n+1/2}_{i+1/2,j,k}\right) \\ &-CB^{i+1/2,j,k+1/2}_{\theta 2}\left(H_r|^{n+1/2}_{i+1,j,k+1/2} - H_r|^{n+1/2}_{i,j,k+1/2}\right) \end{aligned} \tag{3.9}$$

where

$$CA^{i+1/2,j,k+1/2}_\theta = \frac{1-\frac{\sigma_{i+1/2,j,k+1/2}\Delta t}{2\epsilon_0}}{1+\frac{\sigma_{i+1/2,j,k+1/2}\Delta t}{2\epsilon_0}}, \quad CB^{i+1/2,j,k+1/2}_{\theta 1} = \frac{\frac{\Delta t}{\epsilon_0\Delta r}}{1+\frac{\sigma_{i+1/2,j,k+1/2}\Delta t}{2\epsilon_0}},$$

$$\text{and} \quad CB^{i+1/2,j,k+1/2}_{\theta 2} = \frac{\frac{\Delta t}{\epsilon_0\Delta^{j,k+1/2}_{w-e}}}{1+\frac{\sigma_{i+1/2,j,k+1/2}\Delta t}{2\epsilon_0}}$$

Finally, the E_r-field update for regular cells is

$$\begin{aligned} E_r|^{n+1}_{i+1/2,j+1/2,k} &= CA_r^{i+1/2,j+1/2,k} E_r|^{n}_{i+1/2,j+1/2,k} \\ &+CB_{r1}^{i+1/2,j+1/2,k}\left(H_\theta|^{n+1/2}_{i+1,j+1/2,k} - H_\theta|^{n+1/2}_{i,j+1/2,k}\right) \\ &-CB_{r2}^{i+1/2,j+1/2,k}\left(H_\phi|^{n+1/2}_{i+1/2,j+1,k}\frac{\Delta_{w-e}^{j+1,k}}{\Delta_{w-e}^{j+1/2,k}} - H_\phi|^{n+1/2}_{i+1/2,j,k}\frac{\Delta_{w-e}^{j,k}}{\Delta_{w-e}^{j+1/2,k}}\right) \end{aligned} \tag{3.10}$$

where

$$CA_r^{i+1/2,j+1/2,k} = \frac{1-\frac{\sigma_{i+1/2,j+1/2,k}\Delta t}{2\epsilon_0}}{1+\frac{\sigma_{i+1/2,j+1/2,k}\Delta t}{2\epsilon_0}}, \quad CB_{r1}^{i+1/2,j+1/2,k} = \frac{\frac{\Delta t}{\epsilon_0\Delta_{w-e}^{j+1/2,k}}}{1+\frac{\sigma_{i+1/2,j+1/2,k}\Delta t}{2\epsilon_0}},$$

$$\text{and} \quad CB_{r2}^{i+1/2,j+1/2,k} = \frac{\frac{\Delta t}{\epsilon_0\Delta_{s-n}^{k}}}{1+\frac{\sigma_{i+1/2,j+1/2,k}\Delta t}{2\epsilon_0}}$$

For trapezoidal merging cells is followed by

$$\begin{aligned} E_r|^{n+1}_{i+1,j+3/2,k} &= CA_r^{i+1,j+3/2,k} E_r|^{n}_{i+1,j+3/2,k} \\ &+CB_{r1}^{i+1,j+3/2,k}\left(H_\theta|^{n+1/2}_{i+3,j+3/2,k} - H_\theta|^{n+1/2}_{i,j+3/2,k}\right) \\ &-CB_{r2}^{i+1,j+3/2,k}\left(H_\phi|^{n+1/2}_{i+1,j+2,k}\frac{\Delta_{w-e}^{j+2,k}}{\Delta_{w-e}^{j+3/2,k}} - \frac{H_\phi|^{n+1/2}_{i+1/2,j+1,k}+H_\phi|^{n+1/2}_{i+3/2,j+1,k}}{2}\frac{\Delta_{w-e}^{j+1,k}}{\Delta_{w-e}^{j+3/2,k}}\right) \end{aligned} \tag{3.11}$$

And for triangular merging cells is derived by

$$\begin{aligned} E_r|^{n+1}_{i+2,M+1/2,k} &= CA_r^{i+2,M+1/2,k} E_r|^{n}_{i+2,M+1/2,k} \\ &+CB_{r1}^{i+2,M+1/2,k}\left(H_\theta|^{n+1/2}_{i+4,M+1/2,k} - H_\theta|^{n+1/2}_{i,M+1/2,k}\right) \\ &+CB_{r2}^{i+2,M+1/2,k}\frac{H_\phi|^{n+1/2}_{i+1,M,k}+H_\phi|^{n+1/2}_{i+3,M,k}}{2} \end{aligned} \tag{3.12}$$

where

$$CA_r^{i+2,M+1/2,k} = \frac{1-\frac{\sigma_{i+2,M+1/2,k}\Delta t}{2\epsilon_0}}{1+\frac{\sigma_{i+2,M+1/2,k}\Delta t}{2\epsilon_0}}, \quad CB_{r1}^{i+2,M+1/2,k} = \frac{\frac{2\Delta t}{\epsilon_0\Delta_{w-e}^{M,k}\sin\alpha}}{1+\frac{\sigma_{i+2,M+1/2,k}\Delta t}{2\epsilon_0}},$$

$$\text{and} \quad CB_{r2}^{i+2,M+1/2,k} = \frac{\frac{2\Delta t}{\epsilon_0\Delta_{s-n}^{k}\sin\alpha}}{1+\frac{\sigma_{i+2,M+1/2,k}\Delta t}{2\epsilon_0}} \quad \text{with} \quad \alpha = \cos^{-1}\left[\frac{\Delta_{w-e}^{M,k}}{2\Delta_{s-n}^{k}}\right]$$

3.2.2 Stochastic model - Global PCE-FDTD update equations (Northern hemisphere)

The polynomial chaos method expands the uncertain field components (E, H) as a truncated summation of orthogonal basis functions ψ_a, which are chosen from the Weiner-Askey scheme [35]. With $u = \phi, \theta, r$; we set

$$H_u = \sum_{a=0}^{P} h_u^a \psi_a(\boldsymbol{\xi}) \tag{3.13}$$

$$E_u = \sum_{a=0}^{P} e_u^a \psi_a(\boldsymbol{\xi}) \tag{3.14}$$

where h_u^a, e_u^a are the weighting coefficients. For the case of N mutually independent input variables, i.e., $\boldsymbol{\xi} = \xi_1, \xi_2, ..., \xi_N$, the multivariate polynomial chaos basis function may be expressed as

$$\psi_a(\boldsymbol{\xi}) = \prod_{i=1}^{N} \phi_{m_i^a}(\xi_i) \tag{3.15}$$

where $\phi_{m_i^a}(\xi_i)$ is a one-dimensional orthogonal polynomial in ξ_i, and m_i^a is the multi-index corresponding to the order of the expansion for $a = 0, ..., P$. The number of terms is given by

$$P + 1 = \frac{(N + D)!}{N!D!} \tag{3.16}$$

where D is the highest polynomial order in the expansion.

The orthogonality property of the polynomials is expressed by

$$\langle \psi_a(\boldsymbol{\xi}), \psi_b(\boldsymbol{\xi}) \rangle = \left\langle \psi_b^2(\boldsymbol{\xi}) \right\rangle \delta_{a,b} \tag{3.17}$$

where $\delta_{a,b}$ is the Kronecker delta function ($\delta_{a,b} = 0$ if $a \neq b$ and $\delta_{a,b} = 1$ if $a = b$). To evaluate the coefficients h_u^a, e_u^a, the Galerkin method is used. This method takes inner products of expansions with the test function $\psi_b(\boldsymbol{\xi})$ (where $b = 0, ..., P$) as follows

$$h_u^b = \frac{\langle H_u, \psi_b(\boldsymbol{\xi}) \rangle}{\left\langle \psi_b^2(\boldsymbol{\xi}) \right\rangle} \quad \text{and} \quad e_u^b = \frac{\langle E_u, \psi_b(\boldsymbol{\xi}) \rangle}{\left\langle \psi_b^2(\boldsymbol{\xi}) \right\rangle} \tag{3.18}$$

Note that the choice of $\phi_{m_i^a}(\xi_i)$ depends on the distribution of the random variable ξ_i and follows the Weiner-Askey scheme. For example, Gaussian distributed inputs are associated with Hermite polynomials and uniformly distributed inputs with Legendre polynomials. Table 3.1 summarizes the polynomial chaos basis functions truncated at

order $D = 2$, for $N = 3$ (where ξ_1 is Gaussian distributed, and ξ_2, ξ_3 are uniformly distributed).

Once the coefficients e_u^a, h_u^a are found, the mean and variance of the output fields may be directly obtained. For example, the mean and variance of the E_r field is

$$\mu\left[E_{r,i+1/2,j+1/2,k}\left(\boldsymbol{\xi}\right)\right] = e^0_{r,i+1/2,j+1/2,k} \tag{3.19}$$

$$\sigma^2\left[E_{r,i+1/2,j+1/2,k}\left(\boldsymbol{\xi}\right)\right] = \sum_{a=1}^{P}(e^a_{r,i+1/2,j+1/2,k})^2\left\langle\psi_a^2\right\rangle \tag{3.20}$$

To derive the stochastic update equations for the global FDTD Earth-ionosphere waveguide model, the approach described above is applied to all of the update equations of Section 3.2.1. Note that none of H-field update equations of Section 3.2.1 contain the electrical conductivity parameter, which is the only uncertainty input parameter. Therefore, the stochastic update equations for all of the H-field components have an analogous form as the deterministic update equations. This is due to the orthogonality condition of (3.17). For example, the stochastic update equation for both regular and merging cell H_θ-field (for both trapezoidal and triangular cells) is given by

$$\begin{aligned} h_\theta^b|^{n+1/2}_{i,j+1/2,k} = h_\theta^b|^{n-1/2}_{i,j+1/2,k} &+ DB_{\theta1}^{j+1/2,k}\left(e_r^b|^n_{i+1/2,j+1/2,k} - e_r^b|^n_{i-1/2,j+1/2,k}\right) \\ &- DB_{\theta2}\left(e_\phi^b|^n_{i,j+1/2,k+1/2} - e_\phi^b|^n_{i,j+1/2,k-1/2}\right) \end{aligned} \tag{3.21}$$

On the other hand, all the coefficients of E-field update equations include the electrical conductivity parameter in which may be spatially seen as uncertainty. For each computational cell wherein the cell's conductivity is considered as an uncertainty (such as in the ionosphere, but not in the air region immediately above the ground), its E-field update equations are derived as shown in (3.22)-(3.26) after applying the Galerkin process.

Both regular and merging cell E_ϕ-field (for both trapezoidal and triangular cells) updates

$$\begin{aligned} e_\phi^b|^{n+1}_{i,j+1/2,k+1/2} = \frac{1}{\left\langle\psi_b^2\right\rangle}\sum_{a=0}^{P}\Big[& e_\phi^a|^n_{i,j+1/2,k+1/2}\left\langle CA_\phi^{i,j+1/2,k+1/2}(\boldsymbol{\xi})\psi_a(\boldsymbol{\xi})\psi_b(\boldsymbol{\xi})\right\rangle \\ &+ \left(h_r^a|^{n+1/2}_{i,j+1,k+1/2} - h_r^a|^{n+1/2}_{i,j,k+1/2}\right)\left\langle CB_{\phi1}^{i,j+1/2,k+1/2}(\boldsymbol{\xi})\psi_a(\boldsymbol{\xi})\psi_b(\boldsymbol{\xi})\right\rangle \\ &- \left(h_\theta^a|^{n+1/2}_{i,j+1/2,k+1} - h_\theta^a|^{n+1/2}_{i,j+1/2,k}\right)\left\langle CB_{\phi2}^{i,j+1/2,k+1/2}(\boldsymbol{\xi})\psi_a(\boldsymbol{\xi})\psi_b(\boldsymbol{\xi})\right\rangle\Big] \end{aligned} \tag{3.22}$$

Both regular and merging cell E_θ-field (for both trapezoidal and triangular cells) updates

$$e_\theta^b|_{i+1/2,j,k+1/2}^{n+1} = \frac{1}{\langle \psi_b^2 \rangle} \sum_{a=0}^{P} \Big[e_\theta^a|_{i+1/2,j,k+1/2}^{n} \left\langle CA_\theta^{i+1/2,j,k+1/2}(\xi)\psi_a(\xi)\psi_b(\xi) \right\rangle + \left(h_\phi^a|_{i+1/2,j,k+1}^{n+1/2} - h_\phi^a|_{i+1/2,j,k}^{n+1/2} \right) \left\langle CB_{\theta 1}^{i+1/2,j,k+1/2}(\xi)\psi_a(\xi)\psi_b(\xi) \right\rangle - \left(h_r^a|_{i+1,j,k+1/2}^{n+1/2} - h_r^a|_{i,j,k+1/2}^{n+1/2} \right) \left\langle CB_{\theta 2}^{i+1/2,j,k+1/2}(\xi)\psi_a(\xi)\psi_b(\xi) \right\rangle \Big] \tag{3.23}$$

Regular E_r-field updates

$$e_r^b|_{i+1/2,j+1/2,k}^{n+1} = \frac{1}{\langle \psi_b^2 \rangle} \sum_{a=0}^{P} \Big[e_r^a|_{i+1/2,j+1/2,k}^{n} \left\langle CA_r^{i+1/2,j+1/2,k}(\xi)\psi_a(\xi)\psi_b(\xi) \right\rangle + \left(h_\theta^a|_{i+1,j+1/2,k}^{n+1/2} - h_\theta^a|_{i,j+1/2,k}^{n+1/2} \right) \left\langle CB_{r1}^{i+1/2,j+1/2,k}(\xi)\psi_a(\xi)\psi_b(\xi) \right\rangle - \left(h_\phi^a|_{i+1/2,j+1,k}^{n+1/2} \frac{\Delta_{w-e}^{j+1,k}}{\Delta_{w-e}^{j+1/2,k}} - h_\phi^a|_{i+1/2,j,k}^{n+1/2} \frac{\Delta_{w-e}^{j,k}}{\Delta_{w-e}^{j+1/2,k}} \right) \left\langle CB_{r2}^{i+1/2,j+1/2,k}(\xi)\psi_a(\xi)\psi_b(\xi) \right\rangle \Big] \tag{3.24}$$

Trapezoidal merging cell E_r-field updates

$$e_r^b|_{i+1,j+3/2,k}^{n+1} = \frac{1}{\langle \psi_b^2 \rangle} \sum_{a=0}^{P} \Big[e_r^a|_{i+1,j+3/2,k}^{n} \left\langle CA_r^{i+1,j+3/2,k}(\xi)\psi_a(\xi)\psi_b(\xi) \right\rangle + \left(h_\theta^a|_{i+3,j+3/2,k}^{n+1/2} - h_\theta^a|_{i,j+3/2,k}^{n+1/2} \right) \left\langle CB_{r1}^{i+1,j+3/2,k}(\xi)\psi_a(\xi)\psi_b(\xi) \right\rangle - \left(h_\phi^a|_{i+1,j+2,k}^{n+1/2} \frac{\Delta_{w-e}^{j+2,k}}{\Delta_{w-e}^{j+3/2,k}} - \frac{h_\phi^a|_{i+1/2,j+1,k}^{n+1/2} + h_\phi^a|_{i+3/2,j+1,k}^{n+1/2}}{2} \frac{\Delta_{w-e}^{j+1,k}}{\Delta_{w-e}^{j+3/2,k}} \right) \times \left\langle CB_{r2}^{i+1,j+3/2,k}(\xi)\psi_a(\xi)\psi_b(\xi) \right\rangle \Big] \tag{3.25}$$

Triangular cell E_r-field (merging cell case) updates

$$e_r^b|_{i+2,M+1/2,k}^{n+1} = \frac{1}{\langle \psi_b^2 \rangle} \sum_{a=0}^{P} \Big[e_r^a|_{i+2,M+1/2,k}^{n} \left\langle CA_r^{i+2,M+1/2,k}(\xi)\psi_a(\xi)\psi_b(\xi) \right\rangle + \left(h_\theta^a|_{i+4,M+1/2,k}^{n+1/2} - h_\theta^a|_{i,M+1/2,k}^{n+1/2} \right) \left\langle CB_{r1}^{i+2,M+1/2,k}(\xi)\psi_a(\xi)\psi_b(\xi) \right\rangle + \frac{h_\phi^a|_{i+1,M,k}^{n+1/2} + h_\phi^a|_{i+3,M,k}^{n+1/2}}{2} \left\langle CB_{r2}^{i+2,M+1/2,k}(\xi)\psi_a(\xi)\psi_b(\xi) \right\rangle \Big] \tag{3.26}$$

All of the inner products of the three random functions may be precomputed via numerical integration before time-stepping begins. This step obviously requires some extra memory and simulation time, but its cost is negligible compared to a single run of the deterministic simulation.

To minimize the amount of memory needed, the electrical conductivities at the locations of the E_ϕ and E_θ components are interpolated from the conductivities at the locations

of the four nearest-neighbor E_r components (which are stored in memory). For example, consider the electrical conductivity at the location of $E_\theta^{i+1/2,j,k+1/2}$ near a material interface, specifically for a case wherein the $E_\theta^{i+1/2,j,k+1/2}$ is surrounded by a material with no conductivity randomness at two of the nearest-neighbor E_r components, and a material with conductivities following an independent random variable ξ_1 and ξ_2 at the other two nearest-neighbor E_r components. In this case, the inner product integral may be calculated according to (3.27).

$$\begin{aligned}&\left\langle CB_{\theta 1}^{i+1/2,j,k+1/2}(\xi_1,\xi_2)\psi_a(\xi_1,\xi_2)\psi_b(\xi_1,\xi_2)\right\rangle \\ &= \int_\Gamma \frac{2\Delta t}{\Delta r[2\epsilon_0 + (\sigma_{i+1/2,j+1/2,k}(\xi_1) + \sigma_{i+1/2,j+1/2,k+1}(\xi_2) + \sigma_{i+1/2,j-1/2,k} + \sigma_{i+1/2,j-1/2,k+1})\Delta t/4]} \times \\ &\qquad \psi_a(\xi_1,\xi_2)\psi_b(\xi_1,\xi_2)\rho(\xi_1,\xi_2)d(\xi_1)d(\xi_2)\end{aligned} \tag{3.27}$$

For other $E_\theta^{i+1/2,j,k+1/2}$ locations not inside or neighboring any uncertainty materials, these inner products reduce to two random functions and may then utilize the orthogonal property of the polynomial basis functions. Thus the E-field update equations may be decoupled and solved for $b = 0, ..., P$ independently, as for the H-field update equations.

3.2.3 Sensitivities

In order to analyze the impact of the uncertain inputs on the variability of the output electromagnetic field components, the Sobol decomposition is applied to equations (3.13) and (3.14) [64], [65]. The Sobol decomposition yields a set of conditional variances (the Sobol indices) indicating the relative contribution each combination of input parameters makes toward the uncertainty of the output E and H fields. Using E_r as an example, the Sobol indices for the set of inputs v, with $v \subseteq \{1, 2, ..., N\}$, are given by [65]

$$S_v = \frac{\sum_{m\in K_v}(e^m_{r,i+1/2,j+1/2,k})^2 \left\langle \psi_m^2 \right\rangle}{\sum_{a=1}^{P}(e^a_{r,i+1/2,j+1/2,k})^2 \left\langle \psi_a^2 \right\rangle} \tag{3.28}$$

where K_v is an index to the terms in (3.14) that contain v.

3.3 Numerical examples

To validate the new 3-D PCE-FDTD model in this chapter, the ELF propagation characteristics reported in [9] are first reproduced. A resolution of $40 \times 40 \times 5$ km at the

equator is chosen for accuracy (at least 10 cells per wavelength at ELF) and to resolve major topographical details. For the lithosphere, conductivity values are assigned according to Figure 13 of [66], depending on whether a grid cell coordinate is below an ocean or a continent. For the ionosphere, the exponential conductivity profile of [54] is used, with an additional assumption that the conductivity values have an uncertainty layer at the heights of 35, 50, and 75 km as shown in Figure 3.2. The uncertainty parameters behave as three independent random variables with distributions and statistical values given in Table 3.2.

The source is a vertical, 5 km-long current pulse having a Gaussian time-waveform with a $1/e$ full-width of $480\Delta t$, where $\Delta t = 3.0\mu s$. It is located just above the Earth's surface on the equator at longitude 47^0W. First, a brute-force 1000 iterations Monte Carlo simulation is run following by Algorithm 1 to make a benchmark for the model's validation. Second, PCE simulations of first and second order following by Algorithm 2 are computed.

Figures 3.3 and 3.4 illustrate time-waveforms comparing the mean and standard deviation, respectively, of the radial E-field computed via the new PCE method versus the Monte Carlo method. The observation point is located on the Earth's surface at the equator directly east of the source at $1/4$ of the distance to the antipode. Figures 3.3 and 3.4 indicate that the PCE method with order $d = 1$ is already quite accurate, and that the PCE results of order $d = 2$ are nearly a perfect match with the Monte Carlo results.

Figure 3.5 includes 20 lines of the standard deviation values based on limited sets of Monte Carlo simulations (each 50 out of 1000 runs). The large variation of the lines in Figure 3.5 demonstrate the need to run thousands of Monte Carlo simulations in order to obtain accurate standard deviation results. A large number of Monte Carlo simulations are needed because of the large variability of the input conductivity parameters shown in Table 3.2. Even when the standard deviation of the conductivity layer at 50 and 75 km is increased to 50% and 100%, respectively, it is also quite clear that a PCE with $d = 2$ is good enough to capture the statistical information of the system response as shown in Figure 3.6. On the other hand, the Monte Carlo method required an additional one thousand simulations.

Using the approach of Section 3.2.3, Figure 3.7 shows the relative contribution that each

ionosphere conductivity layer makes toward the uncertainty in E_r computed via equation (3.28). The results in this figure indicate that the variation of the output E_r-field relies mostly on the variation of the conductivity layers at 50 and 75 km during the period of $7000 - 10000$ time steps, where the amplitude of the ELF propagation pulse is largest. This sensitivity analysis is valuable as it indicates which layers have greater impact in the variability of the response and play a important role on ELF propagation. For example, Figure 3.8 plots the sensitivity analysis for a test case wherein four conductivity layers at 40, 60, 80 and 100 km have an identical variability of $\sigma = 20\%$. The conductivity variations at 60 and 80 km are seen to have a larger impact than the variations at 40 and 100 km on $7000 - 10000$ time steps of interest. It may leads to two conclusions: first, as the atmosphere conductivity follows exponential profile, the values at 40 km is too small to affect the ELF propagation, and second, the ELF waves are reflected below 100 km (which is why the upper boundary of the grid may be set to a PEC).

Finally, Table 3.3 compares the efficiency of the Monte Carlo method to the proposed PCE-based method. Both methods are parallelized and run on the Blue Waters supercomputer at the University of Illinois Urbana-Champaign using 256 computational cores. The comparison confirms the efficiency and time-savings of the PCE method over the brute-force Monte Carlo approach.

3.4 Summary

Modeling ELF electromagnetic wave propagation in the global Earth-ionosphere waveguide using the FDTD method must be as efficient as possible due to the required large number of grid cells and long simulation times (large number of time steps due to the small time step increments). In order to account for the uncertainty and variability of the ionospheric conductivity resulting from space weather events, time of day, etc., a large number of simulations are needed when utilizing the Monte Carlo method. In this chapter, an efficient numerical approach has been presented to calculate both the mean and variance of the electric and magnetic fields in the Earth-ionosphere waveguide using the nonsampling PCE-based FDTD method. Excellent agreement was obtained between the results of the proposed method and the standard Monte Carlo method. Furthermore, the proposed method was shown to be more computationally efficient than the Monte

Carlo approach. This PCE-FDTD method can be used as a powerful numerical tool for any complex ELF propagation models since the method is applicable to any type of medium's structures, including one that is too complex to study by analytical methods.

It is worth noting that the proposed global stochastic model may be applied to a localized high resolution regions, uncertainty in the ground conductivity, or even to other planets in a straightforward manner. For example, studying Schumann resonances on planets such as Venus, Mars, Jupiter, Saturn, Titan etc., still remains active research area (e.g., [52], [67]–[72]). Some planets are known to have rather low ground conductivity that has a significant influence on the ELF wave propagation. In such cases, uncertainty in the ground conductivity may be included in the model due to lack of full knowledge of the ground conductivity parameter. The equations set developed in this chapter is also fully capable of studying these cases.

Algorithm 1 Monte Carlo simulation

1: //*num_uncert*: number of conductivity uncertainties
2: **for** $nn = 1 \rightarrow num\_uncert$ **do**
3: //*num_MC*: Monte Carlo iterations
4: **for** $m = 1 \rightarrow num\_MC$ **do**
5: Generate and assign random values for each conductivity value $array\_cond(m, nn)$
6: **end for**
7: **end for**
8: //Begin Monte Carlo simulation
9: **for** $m = 1 \rightarrow num\_MC$ **do**
10: Calculate all coefficients using conductivities $array\_cond(m, nn)$ determined earlier
11: //Begin time stepping loop
12: **for** $n = 1 \rightarrow nmax$ **do**
13: Calculate space loop for H-field and E-field using equations (3.1)-(3.12)
14: **end for**
15: **end for**
16: **for** $n = 1 \rightarrow nmax$ **do**
17: //Calculate mean and standard deviation values of H-field and E-field
18: $\mu(n) = \frac{1}{num\_MC} \sum_{m=1}^{num\_MC} array(m, n)$
19:
20: $\sigma(n) = \sqrt{\frac{1}{num\_MC} \sum_{m=1}^{num\_MC} [array(m, n) - \mu(n)]^2}$
21: **end for**

Algorithm 2 PCE simulation

for $b = 0 \rightarrow P$ **do**
    Calculate $\langle \psi_b^2 \rangle$
end for
for $nn = 1 \rightarrow num\_uncert$ **do**
    for $a = 0 \rightarrow P$ **do**
        for $b = 0 \rightarrow P$ **do**
            Pre-calculate all inner products
        end for
    end for
end for
//Begin time stepping loop
for $n = 1 \rightarrow nmax$ **do**
    for $b = 0 \rightarrow P$ **do**
        Calculate space loop for H-field using (3.21)
        REGULAR_MESH = TRUE
        for $nn = 1 \rightarrow num\_uncert$ **do**
            if $i, j, k \in [i, j, k\_uncert\_start(nn) \rightarrow i, j, k\_uncert\_end(nn)]$ **then**
                REGULAR_MESH = FALSE
                Calculate E-field using (3.22)-(3.26)
            end if
        end for
        if REGULAR_MESH = TRUE **then**
            Calculate E-field using regular updates
        end if
    end for
    Calculate mean and standard deviation values of H-field and E-field and sensitivity using (3.19), (3.20) and (3.28)
end for

Table 3.1: Polynomials chaos basis for the case of three independent random variables ($N = 3, \boldsymbol{\xi} = [\xi_1, \xi_2, \xi_3]$) and a second-order expansion ($D = 2$)

Index b	Order D	b^{th} basis $\boldsymbol{\psi_b}$	$\langle \boldsymbol{\psi_b^2} \rangle$
0	0	1	1
1	1	ξ_1	1
2	1	ξ_2	1/3
3	1	ξ_3	1/3
4	2	$\xi_1^2 - 1$	2
5	2	$\xi_1\xi_2$	1/3
6	2	$\xi_1\xi_3$	1/3
7	2	$\frac{1}{2}(3\xi_2^2 - 1)$	1/5
8	2	$\xi_2\xi_3$	1/9
9	2	$\frac{1}{2}(3\xi_3^2 - 1)$	1/5

Table 3.2: Input parameters and uncertainty

Ionospheric cond. layer	Mean value μ	Distribution
at 35 km	$1.62\times10^{-11}(S/m)$	Gaussian, $\sigma = 20\%$
at 50 km	$1.16\times10^{-9}(S/m)$	Uniform, $\sigma = 30\%$
at 75 km	$1.44\times10^{-6}(S/m)$	Uniform, $\sigma = 60\%$

Table 3.3: Simulation time required by the MC and the proposed PCE-based methods

Method	MC 1000 runs	PCE order=1	PCE order=2
Simulation time	10 days	1 hour 49 mins	8 hours 33 mins

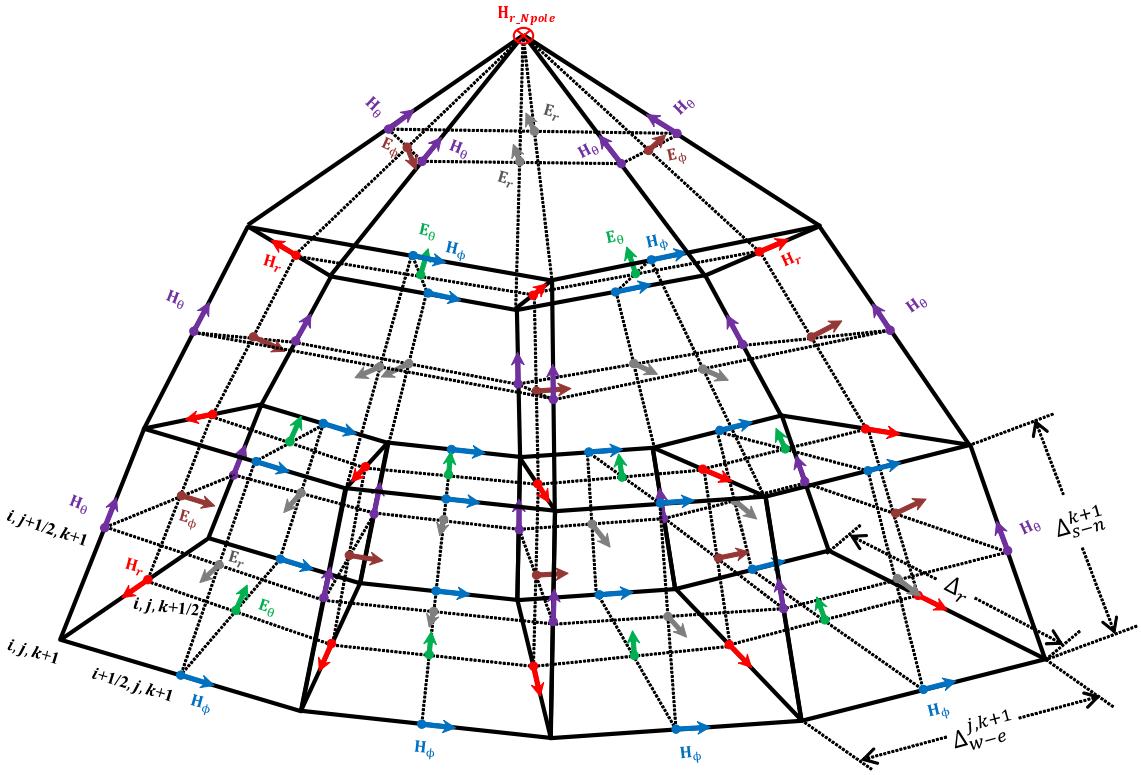

Figure 3.1: FDTD grid cells in the vicinity of the North pole.

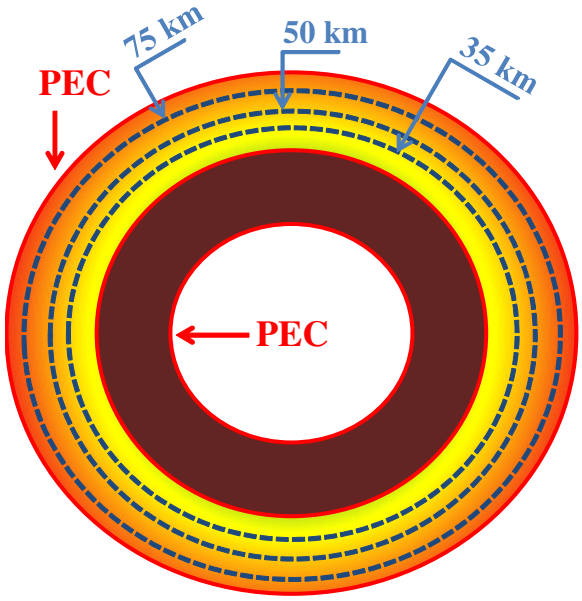

Figure 3.2: Diagram depicting the general geometry of the global FDTD model (Note: Not drawn to scale).

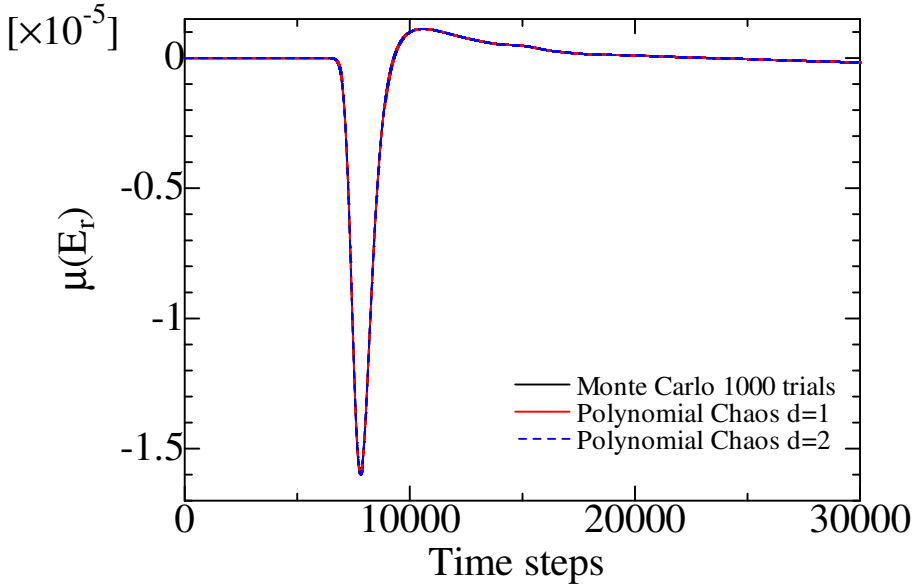

Figure 3.3: Mean value of E_r (observed at the Equator located 1/4 of the distance to the antipode).

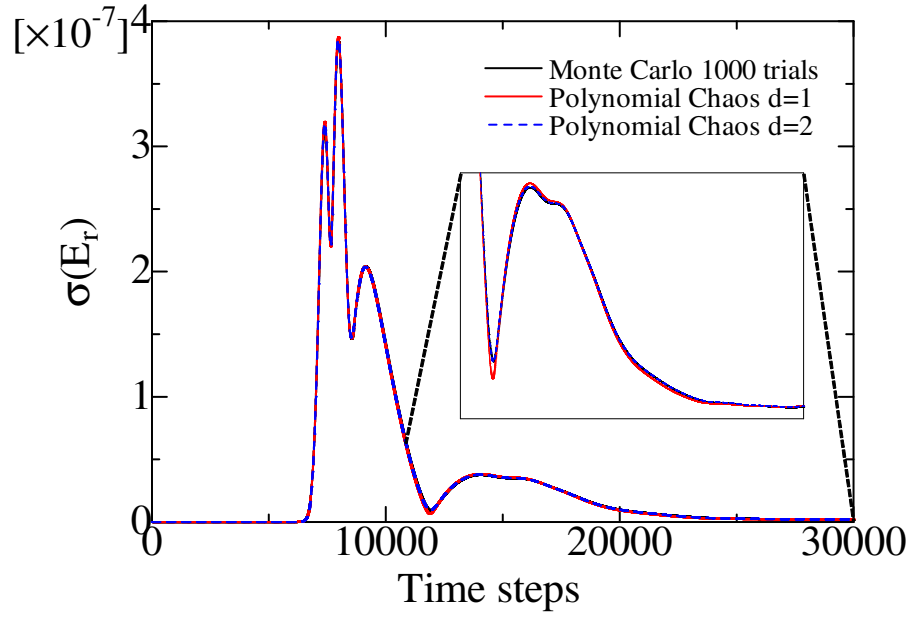

Figure 3.4: Standard deviation of E_r (observed at the Equator located 1/4 of the distance to the antipode).

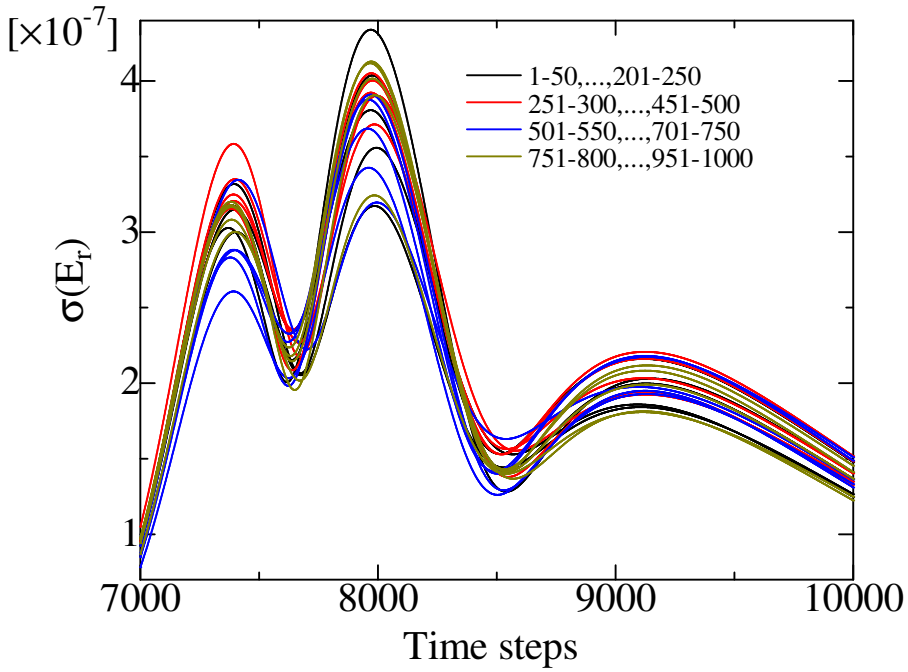

Figure 3.5: Standard deviation results obtained from each set of 50 simulations (out of the total 1000 simulations) of the Monte Carlo method.

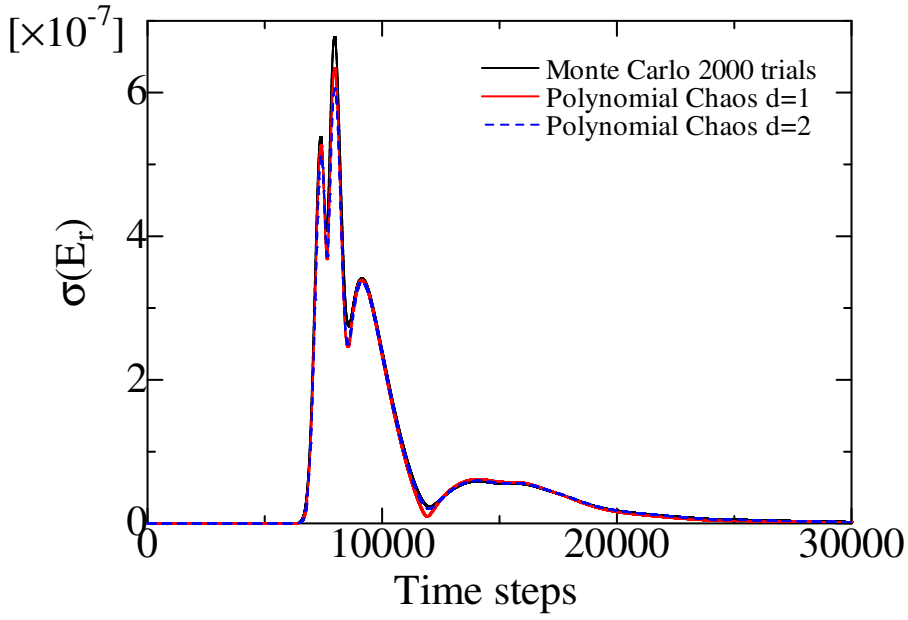

Figure 3.6: Standard deviation of E_r when the standard deviation of the conductivity layer at 50 and 75 km are increased to 50% and 100%, respectively.

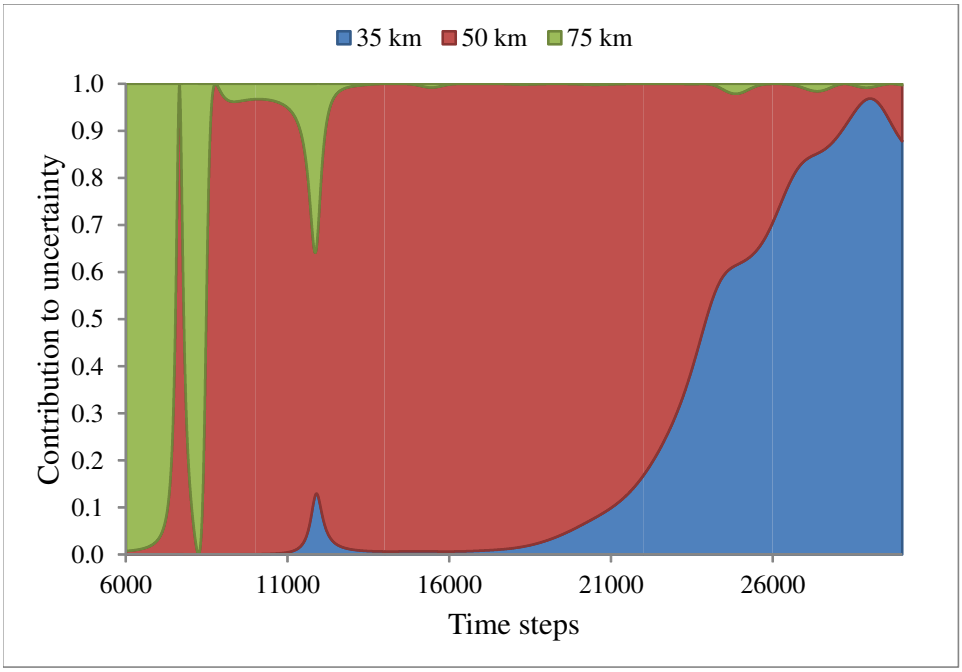

Figure 3.7: Relative contribution of each ionosphere conductivity layer to the uncertainty computed using the order $d = 2$ expansion (three layers case).

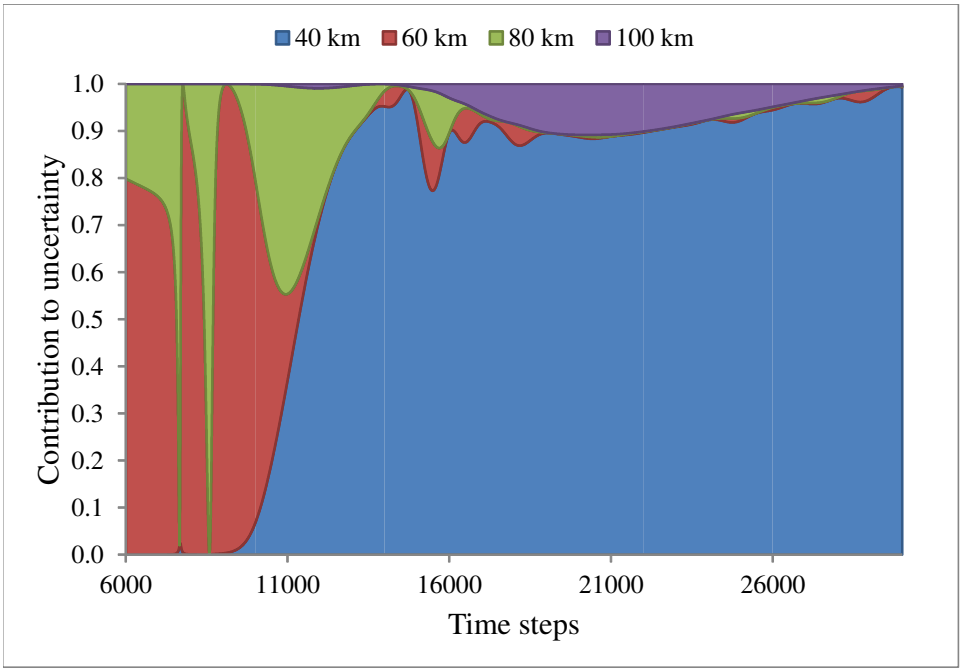

Figure 3.8: Relative contribution of each ionosphere conductivity layer to the uncertainty computed using the order $d = 2$ expansion (fours layers case).

CHAPTER 4

ANALYSIS OF ELECTROMAGNETIC WAVE PROPAGATION IN VARIABLE MAGNETIZED PLASMA VIA THE POLYNOMIAL CHAOS EXPANSION METHOD

4.1 Introduction

In 1837, W. R. Hamilton introduced a system of differential equations describing ray paths through general anisotropic media [73]. In 1954, J. Haselgrove proposed that Hamilton's equations were suitable for numerical integration on electronic computers and could provide a means of calculating ray paths in the ionosphere [74]. In 1960, C. Haselgrove and J. Haselgrove implemented such a ray-tracing program to calculate "twisted ray paths" through a model ionosphere using Cartesian coordinates [75], [76].

In 1975, R. M. Jones and J. J. Stephenson generated "an accurate, versatile FORTRAN computer program for tracing rays through an anisotropic medium whose index of refraction varies continuously in three dimensions" [77]. This model and variations of it are still in use today, and have been applied to such applications as over-the-horizon radar [76]. Additionally, many other related techniques have now been generated especially for higher frequency scintillation studies, including the phase screen [78] or Rytov approximation, parabolic equation method [79], and even hybrid methods, such as combining the complex phase method and the technique of a random screen [80].

These techniques, however, are only valid under certain conditions. The complex phase method, for example, is only valid for EM wave propagation above 1 GHz. The phase screen or Rytov approximation is only valid for weak fluctuations of the ionosphere. And for all of these methods involving ray tracing, as the frequency of the EM wave is reduced and its wavelength increases, the calculated results diverge from the true solution as the physical reality departs from the short-wavelength asymptotic assumptions underlying geometrical optics and ray tracing [14].

An alternative to ray tracing is full-vector Maxwell's equations FDTD modeling, which is not limited by the above issues. To study the performance capability of an example FDTD plasma algorithm, FDTD plasma model results have previously been compared to ray-tracing results for the application of reducing the radar cross-section of targets [81]. Although Chaudhury and Chaturvedi limited their study to unmagnetized, collisional cold plasmas, they conclude that FDTD is more accurate and less restrictive than ray tracing, at the cost of being more computationally demanding. For example, they determine that ray tracing only yields accurate results in their study when both the density scale length is long compared to the free-space wavelength of the incident wave, and when the conduction current is small as compared to the displacement current in the medium. Additionally, ray tracing provides solutions at only individual frequencies (i.e., for sinusoidal steady-state signals, not for pulses).

FDTD plasma models have been developed by a number of groups (e.g., [5], [6], [11]). However, all of these models require large amounts of computer memory, require very small time steps linked to the plasma parameters rather than the Courant limit, or produce nonphysically spurious electrostatic waves (of numerical origin) due to the spatially non-collocated status of electric fields and current densities, resulting in late-time instabilities [14].

In recent years, FDTD anisotropic magnetized ionospheric plasma models have been incorporated into global FDTD models to extend their capabilities (note that it is straightforward to apply these formulations on a local scale as well). Specifically, a fully three-dimensional (3-D) Cartesian plasma model developed in [14] was applied to the 3-D FDTD latitude-longitude global spherical grid [15] of [9]. By accounting for 3-D magnetized ionospheric plasma physics, [14] was the first global FDTD model to include the calculation of all important ionospheric effects on signals, including absorption, refraction, phase and group delay, frequency shift, polarization, and Faraday rotation. Subsequently, a more efficient magnetized plasma algorithm that avoids the complex matrix formulation used in [15] was published and adapted to the 3-D FDTD latitude-longitude global model [16]. Two FDTD plasma models in [14], [16] are utilized to develop stochastic FDTD plasma models described in Chapter 4 and 5 since these models do not suffer from the previous models' drawbacks. More specifically, the polynomial chaos expansion (PCE) method is

applied to the model in [16] while the delta method is applied to the model in [14]. These selections are simply based on mathematical compatibility of each pair.

All of the above FDTD plasma models, however, account for only average (mean) composition values of the lithosphere and ionosphere and then solve for only expected (mean) electric and magnetic fields without considering the associated uncertainties in these physical quantities. Not accounting for the variability of the lithosphere and ionosphere content can limit the utility of EM propagation modeling for communications, surveillance, navigation, and geophysical applications. As one example, the ionosphere strongly effects trans-ionospheric EM propagation: the irregularities in the electron density distribution can cause highly complex phase and amplitude scintillation. In these situations, it is highly desirable to consider models which account for random variability within the propagation media.

The ionosphere may be treated as a random medium to account for the variable / uncertain composition and dynamics resulting from solar and geomagnetic activities. Past and recent investigations (e.g., [82]–[86]) on the temporal and spatial ionospheric variations have improved our understanding of the dynamics of the ionosphere under normal and disturbed conditions. This knowledge should be incorporated into numerical EM propagation models. The Monte Carlo method is a widely used brute force technique for evaluating random medium problems via multiple realizations. However, a well-known disadvantage of the Monte Carlo method is that it is computationally expensive, and quickly becomes computationally infeasible for 3-D problems.

This chapter uses the spectral expansion or the PCE method to represent the stochastic variability of the EM wave propagation in the magnetized cold plasma medium model. Polynomial chaos has previously been applied to computational fluid dynamics [87], [88] and some specific computational EM problems (e.g., [28], [61], [62], [89], [90]). Recently, the PCE method was applied to investigate the impact of fire on the indoor wireless channel where fire is modeled as a cold plasma medium without considering the ambient magnetic field $\mathbf{B}$ (i.e., isotropic unmagnetized plasma) [91].

Here, this chapter applies the PCE method to EM propagation in the ionosphere in the presence of a magnetic field, $\mathbf{B}$. Specifically, realistic ionospheric electron densities and collision frequencies are used, but the ambient $\mathbf{B}$ is stronger than the Earth's actual

magnetic field so that it will alter particle trajectories over a relatively short distance (i.e., behave as an anisotropic magnetized plasma). Using a larger **B** allows the use of smaller FDTD grids, which makes a comparison with Monte Carlo results more feasible.

In considering the variability of the ionosphere content, the **B** is also treated as a 3-D random parameter since the Earth's magnetic field changes over time. The variation of **B** arises from the variation of currents in the ionosphere and magnetosphere or from the motion of molten iron alloys in its outer core. Our ultimate objective is to develop an optimal (efficient and accurate) stochastic FDTD-based algorithm that is well-suited for large uncertainty quantification of the ionosphere and Earth's magnetic field. Note that although only electrons are considered in this chapter, the PCE formulation presented here is identical for handling positive or negative ions as well.

4.2 Formulation

This Section presents the primary relevant aspects of the magnetized collisional ionospheric plasma algorithm of [16] (presented in Section 4.2.1) that are needed to understand the PCE magnetized plasma formulation (presented in Section 4.2.2). The importance of choosing the plasma formulation of [16] over the formulation of [14] for the PCE stochastic model is included in Section 4.2.1. Finally, the methodology for calculating the global sensitivities of each input parameter on the EM fields is provided in Section 4.2.3.

4.2.1 3D-FDTD collisional magnetized plasma formulation

The magnetized (anisotropic) cold plasma governing equations are cast in terms of Maxwell's equations coupled to current equations derived from the Lorentz equation of motion [14]. The resulting whole governing equation set is given by

$$\nabla \times \mathbf{E} = -\mu_0 \frac{\partial \mathbf{H}}{\partial t} \tag{4.1}$$

$$\nabla \times \mathbf{H} = \epsilon_0 \frac{\partial \mathbf{E}}{\partial t} + \mathbf{J}_e \tag{4.2}$$

$$\frac{\partial \mathbf{J}_e}{\partial t} + v_e \mathbf{J}_e = \epsilon_0 \omega_{Pe}^2 \mathbf{E} + \boldsymbol{\omega}_{Ce} \times \mathbf{J}_e \tag{4.3}$$

Here v_e, J_e, $\boldsymbol{\omega}_{Ce}$, and ω_{Pe} are the collision frequency, the current density, the cyclotron frequency and the plasma frequency of the electrons, respectively. The plasma frequency is a function of the electron density n_e given by

$$\omega_{Pe} = \sqrt{\frac{q_e^2 n_e}{\epsilon_0 m_e}} \tag{4.4}$$

The cyclotron frequency of the electrons is given by $\boldsymbol{\omega}_{Ce} = |q_e|\mathbf{B}/m_e$ where $\mathbf{B}$ is the applied magnetic field. The equations (4.2) and (4.3) imply that this scheme is implicit. As a result, the governing stochastic equations take the form of a large, complex matrix [14]. Unfortunately, the PCE method cannot be applied to this complex matrix equation model because it is not possible to obtain the derivation of the explicit equations for the PCE coefficients. Therefore, a different methodology for solving EM wave propagation in magnetized plasma must be used so that the PCE method can be applied.

Instead, the more efficient 3-D FDTD magnetized plasma algorithm developed in [16] may be used. This formulation takes advantage of the Boris algorithm originally applied to particle-in-cell plasma modeling [92], [93]. In this case, the Lorentz equation is solved explicitly and is easily incorporated into the traditional FDTD Maxwell's equations. However, in the collisional regime, the presence of the collision term in the Lorentz equation of motion makes it infeasible to apply the Boris algorithm directly, since it requires the current density vector at time step $n + 1/2$, which is not yet known. An effective way to overcome this problem is based on the use of the MacCormack predictor-corrector method [94], [95]. Applying the MacCormack method to the Lorentz equation results in a two-step approach involving a predictor step and a corrector step.

First, the discrete form of the Lorentz equation for the predictor step uses the current density vector at $n - 1/2$ to predict the current density vector at $n + 1/2$

$$\frac{\mathbf{J}_{e,p}^{n+1/2} - \mathbf{J}_e^{n-1/2}}{\Delta t} + v_e \mathbf{J}_e^{n-1/2} = \epsilon_0 \omega_{Pe}^2 \mathbf{E}^n - \boldsymbol{\omega}_{Ce} \times \left(\frac{\mathbf{J}_{e,p}^{n+1/2} + \mathbf{J}_e^{n-1/2}}{2} \right) \tag{4.5}$$

The Boris scheme for the predictor step uses two auxiliary current density vectors as follows

$$\mathbf{J}_{e,p}^{+} = \mathbf{J}_{e,p}^{n+1/2} - \frac{\Delta t \epsilon_0 \omega_{Pe}^2 \mathbf{E}^n}{2} + \frac{\Delta t v_e \mathbf{J}_e^{n-1/2}}{2} \tag{4.6}$$

$$\mathbf{J}_{e,p}^{-} = \mathbf{J}_e^{n-1/2} + \frac{\Delta t \epsilon_0 \omega_{Pe}^2 \mathbf{E}^n}{2} - \frac{\Delta t v_e \mathbf{J}_e^{n-1/2}}{2} \tag{4.7}$$

Equation (4.5) is then simplified to

$$\frac{\mathbf{J}_{e,p}^{+} - \mathbf{J}_{e,p}^{-}}{2} = -\boldsymbol{\omega}_{Ce} \times \left(\frac{\mathbf{J}_{e,p}^{+} + \mathbf{J}_{e,p}^{-}}{2} \right) \tag{4.8}$$

Then $\mathbf{J}_{e,p}^{+}$ is calculated from equation (4.8) by rotating $\mathbf{J}_{e,p}^{-}$ by an angle θ as shown in Figure 4.1 via the following equation

$$\mathbf{J}_{e,p}^{+} = \mathbf{J}_{e,p}^{-} + [\mathbf{J}_{e,p}^{-} + (\mathbf{J}_{e,p}^{-} \times \mathbf{t})] \times \mathbf{s} \tag{4.9}$$

where

$$\mathbf{t} = \frac{-\boldsymbol{\omega}_{Ce}}{|\boldsymbol{\omega}_{Ce}|}\tan\frac{\theta}{2};\ \ \mathbf{s} = \frac{-\boldsymbol{\omega}_{Ce}}{|\boldsymbol{\omega}_{Ce}|}\sin\theta;\ \ \frac{\theta}{2} = \tan^{-1}\frac{|\boldsymbol{\omega}_{Ce}|\Delta t}{2}$$

Second, the predicted current density obtained from (4.9) is used to calculate the corrector current density vector in the corrector step according to

$$\frac{\mathbf{J}_{e,c}^{n+1/2} - \mathbf{J}_{e}^{n-1/2}}{\Delta t} + v_e \mathbf{J}_{e,p}^{n+1/2} = \epsilon_0 \omega_{Pe}^2 \mathbf{E}^n - \boldsymbol{\omega}_{Ce} \times \left(\frac{\mathbf{J}_{e,c}^{n+1/2} + \mathbf{J}_{e}^{n-1/2}}{2} \right) \tag{4.10}$$

Following an analogous derivation for the predictor current density vector, the corrector current density vector is obtained. Then, the final current density vector at $n + 1/2$ is the average of the predicted current density vector and the corrected current density vector at $n + 1/2$

$$\mathbf{J}_{e}^{n+1/2} = \frac{\mathbf{J}_{e,p}^{n+1/2} + \mathbf{J}_{e,c}^{n+1/2}}{2} \tag{4.11}$$

At this point, all of the governing equations are solved explicitly and may be derived in discrete form (e.g., as an example, the x-component equations are provided in (4.12)-(4.15)).

Regular H-field update:

$$\begin{aligned} H_x|_{i,j+1/2,k+1/2}^{n+1/2} &= H_x|_{i,j+1/2,k+1/2}^{n-1/2} \\ &+ \frac{\Delta t}{\mu_0}\left[\frac{E_y|_{i,j+1/2,k+1}^{n} - E_y|_{i,j+1/2,k}^{n}}{\Delta z} - \frac{E_z|_{i,j+1,k+1/2}^{n} - E_z|_{i,j,k+1/2}^{n}}{\Delta y} \right] \end{aligned} \tag{4.12}$$

J-field update for the Predictor step (refer to Appendix B for more detailed derivation):

$$\begin{aligned}
J_{ex,p}|^{n+1/2}_{i+1/2,j,k} = J_{ex}|^{n-1/2}_{i+1/2,j,k} + \Delta t\epsilon_0\omega^2_{Pe}E_x|^{n}_{i+1/2,j,k} - \Delta t v_e J_{ex}|^{n-1/2}_{i+1/2,j,k} \\
- \frac{\sin\theta}{|\omega_{Ce}|}\left(J_{ey}|^{n-1/2}_{i+1/2,j,k}\omega_{Cez} - J_{ez}|^{n-1/2}_{i+1/2,j,k}\omega_{Cey}\right) \\
- \frac{\Delta t\epsilon_0\sin\theta}{2|\omega_{Ce}|}\omega^2_{Pe}\left(E_y|^{n}_{i+1/2,j,k}\omega_{Cez} - E_z|^{n}_{i+1/2,j,k}\omega_{Cey}\right) \\
+ \frac{\Delta t\sin\theta}{2|\omega_{Ce}|}v_e\left(J_{ey}|^{n-1/2}_{i+1/2,j,k}\omega_{Cez} - J_{ez}|^{n-1/2}_{i+1/2,j,k}\omega_{Cey}\right) \\
+ \frac{\tan\frac{\theta}{2}\sin\theta}{|\omega_{Ce}|^2}\left[\left(J_{ez}|^{n-1/2}_{i+1/2,j,k}\omega_{Cex} - J_{ex}|^{n-1/2}_{i+1/2,j,k}\omega_{Cez}\right)\omega_{Cez}\right. \\
\left. - \left(J_{ex}|^{n-1/2}_{i+1/2,j,k}\omega_{Cey} - J_{ey}|^{n-1/2}_{i+1/2,j,k}\omega_{Cex}\right)\omega_{Cey}\right] \\
+ \frac{\Delta t\epsilon_0\tan\frac{\theta}{2}\sin\theta}{2|\omega_{Ce}|^2}\omega^2_{Pe}\left[\left(E_z|^{n}_{i+1/2,j,k}\omega_{Cex} - E_x|^{n}_{i+1/2,j,k}\omega_{Cez}\right)\omega_{Cez}\right. \\
\left. - \left(E_x|^{n}_{i+1/2,j,k}\omega_{Cey} - E_y|^{n}_{i+1/2,j,k}\omega_{Cex}\right)\omega_{Cey}\right] \\
- \frac{\Delta t\tan\frac{\theta}{2}\sin\theta}{2|\omega_{Ce}|^2}v_e\left[\left(J_{ez}|^{n-1/2}_{i+1/2,j,k}\omega_{Cex} - J_{ex}|^{n-1/2}_{i+1/2,j,k}\omega_{Cez}\right)\omega_{Cez}\right. \\
\left. - \left(J_{ex}|^{n-1/2}_{i+1/2,j,k}\omega_{Cey} - J_{ey}|^{n-1/2}_{i+1/2,j,k}\omega_{Cex}\right)\omega_{Cey}\right]
\end{aligned} \tag{4.13}$$

J-field update for the Corrector step:

$$\begin{aligned}
J_{ex,c}|^{n+1/2}_{i+1/2,j,k} = J_{ex}|^{n-1/2}_{i+1/2,j,k} + \Delta t\epsilon_0\omega^2_{Pe}E_x|^{n}_{i+1/2,j,k} - \Delta t v_e J_{ex,p}|^{n+1/2}_{i+1/2,j,k} \\
- \frac{\sin\theta}{|\omega_{Ce}|}\left(J_{ey}|^{n-1/2}_{i+1/2,j,k}\omega_{Cez} - J_{ez}|^{n-1/2}_{i+1/2,j,k}\omega_{Cey}\right) \\
- \frac{\Delta t\epsilon_0\sin\theta}{2|\omega_{Ce}|}\omega^2_{Pe}\left(E_y|^{n}_{i+1/2,j,k}\omega_{Cez} - E_z|^{n}_{i+1/2,j,k}\omega_{Cey}\right) \\
+ \frac{\Delta t\sin\theta}{2|\omega_{Ce}|}v_e\left(J_{ey,p}|^{n+1/2}_{i+1/2,j,k}\omega_{Cez} - J_{ez,p}|^{n+1/2}_{i+1/2,j,k}\omega_{Cey}\right) \\
+ \frac{\tan\frac{\theta}{2}\sin\theta}{|\omega_{Ce}|^2}\left[\left(J_{ez}|^{n-1/2}_{i+1/2,j,k}\omega_{Cex} - J_{ex}|^{n-1/2}_{i+1/2,j,k}\omega_{Cez}\right)\omega_{Cez}\right. \\
\left. - \left(J_{ex}|^{n-1/2}_{i+1/2,j,k}\omega_{Cey} - J_{ey}|^{n-1/2}_{i+1/2,j,k}\omega_{Cex}\right)\omega_{Cey}\right] \\
+ \frac{\Delta t\epsilon_0\tan\frac{\theta}{2}\sin\theta}{2|\omega_{Ce}|^2}\omega^2_{Pe}\left[\left(E_z|^{n}_{i+1/2,j,k}\omega_{Cex} - E_x|^{n}_{i+1/2,j,k}\omega_{Cez}\right)\omega_{Cez}\right. \\
\left. - \left(E_x|^{n}_{i+1/2,j,k}\omega_{Cey} - E_y|^{n}_{i+1/2,j,k}\omega_{Cex}\right)\omega_{Cey}\right] \\
- \frac{\Delta t\tan\frac{\theta}{2}\sin\theta}{2|\omega_{Ce}|^2}v_e\left[\left(J_{ez,p}|^{n+1/2}_{i+1/2,j,k}\omega_{Cex} - J_{ex,p}|^{n+1/2}_{i+1/2,j,k}\omega_{Cez}\right)\omega_{Cez}\right. \\
\left. - \left(J_{ex,p}|^{n+1/2}_{i+1/2,j,k}\omega_{Cey} - J_{ey,p}|^{n+1/2}_{i+1/2,j,k}\omega_{Cex}\right)\omega_{Cey}\right]
\end{aligned} \tag{4.14}$$

E-field update:

$$E_x|^{n+1}_{i+1/2,j,k} = E_x|^{n}_{i+1/2,j,k} + \frac{\Delta t}{\epsilon_0}\left[\frac{H_z|^{n+1/2}_{i+1/2,j+1/2,k} - H_z|^{n+1/2}_{i+1/2,j-1/2,k}}{\Delta y} - \frac{H_y|^{n+1/2}_{i+1/2,j,k+1/2} - H_y|^{n+1/2}_{i+1/2,j,k-1/2}}{\Delta z} - J_{ex}|^{n+1/2}_{i+1/2,j,k}\right] \tag{4.15}$$

Note that in this algorithm, all three current density vector components are collocated in space with an electric field component (we have chosen E_x), but the current density vectors are calculated at the same time step as the magnetic field components. As needed, four neighboring current densities (or electric field components) are averaged to obtain their corresponding values at other positions. Figure 4.2 illustrates the positions of the EM field and current density components in the Yee cell, where all of the current density components are solved at the position of E_x. More details on this algorithm may be found in [16].

4.2.2 3D-PCE-FDTD collisional magnetized plasma formulation

Ionosphere electron densities vary in a complex manner as a function of location and time. Previous studies showed that the ionosphere content, i.e., the electron density and the collision frequency, vary in the ionosphere according to solar activity, e.g., [84]–[86]. Similarly, the Earth's magnetic field which extends from the Earth's interior out into space may also change over short time scales (ms) due to disturbed currents in the ionosphere and over long time scale (years) due to changes in the Earth's interior, particularly the iron-rich core [96]. The electron densities, collision frequencies, and geomagnetic field intensity are considered here as random variables, each having its own statistical variation. This variability in the ionosphere structure and geomagnetic field causes variability in the EM fields and current densities (**E**, **H**, and $\mathbf{J}_e$), which in turn are treated as output random variables. The exact distributions of the electron densities, the collision frequencies and the geomagnetic field intensities are unknown, so these input parameters are assumed to be characterized by a normal (Gaussian) or uniform probability distribution. For example, the electron density n_e, the collision frequency v_e, and the geomagnetic field intensity B are defined by

$$\begin{cases} n_e(\xi_1) = \mu_{n_e} + \sigma_{n_e}\xi_1 \\ v_e(\xi_2) = \mu_{v_e} + \sigma_{v_e}\xi_2 \\ B(\xi_3) = \mu_B + \sigma_B\xi_3 \end{cases} \tag{4.16}$$

where μ_{n_e}, μ_{v_e}, and μ_B are the mean value of the parameters, σ_{n_e}, σ_{v_e}, and σ_B are the standard deviation values, and ξ_1, ξ_2, and ξ_3 are independent normalized Gaussian random variables with a zero mean and unit standard deviation.

In order to implement the PCE method, the uncertain fields are expanded as follows (only the x-components are shown as an example)

$$H_x = \sum_{a=0}^{P} h_x^a \psi_a(\boldsymbol{\xi}) \tag{4.17}$$

$$J_{ex} = \sum_{a=0}^{P} j_{ex}^a \psi_a(\boldsymbol{\xi}) \tag{4.18}$$

$$E_x = \sum_{a=0}^{P} e_x^a \psi_a(\boldsymbol{\xi}) \tag{4.19}$$

where h_x^a, j_{ex}^a, e_x^a are the weighting coefficients, $\boldsymbol{\xi} = [\xi_1, \xi_2, ..., \xi_n]$ represents a vector containing an n number of independent random variables, and ψ are Hermite polynomials. By expanding the uncertain values in this manner, the dependence of the output fields on the random parameter $\boldsymbol{\xi}$ is separated from their dependence on time and spatial position. The choice of the orthogonal basis functions depends on the distribution of the random variables being considered. In this case, Hermite polynomials correspond with a normal distribution.

The number of terms is given by

$$P + 1 = \frac{(n+d)!}{n!d!} \tag{4.20}$$

where d is the order of the highest order Hermite polynomial used in the expansion and n is the number of random variables.

There are two main approaches for evaluating the coefficients h_x^a, j_{ex}^a, e_x^a: (1) the Galerkin (intrusive) method; and (2) the collocation (nonintrusive) method. Here, the Galerkin method is chosen over the collocation method since the modeling of EM wave propagation in magnetized plasma is a large-scale problem wherein a single deterministic computation is already time consuming. Also, the Galerkin method typically offers more accurate and efficient solutions from a single simulation run, even though it is more cumbersome to implement. The expansions of H_x, J_{ex} and E_x are substituted into (4.12)-(4.15). Then the

Galerkin procedure is applied by taking the inner products of the expansion equations with the test function $\psi_b(\boldsymbol{\xi})$, where $b = 0, ..., P$. Then the orthogonality condition

$$\langle \psi_a(\boldsymbol{\xi}), \psi_b(\boldsymbol{\xi}) \rangle = \left\langle \psi_b^2(\boldsymbol{\xi}) \right\rangle \delta_{a,b} \tag{4.21}$$

is used where $\delta_{a,b}$ is the Kronecker delta function ($\delta_{a,b} = 0$ if $a \neq b$ and $\delta_{a,b} = 1$ if $a = b$). This orthogonality reduces the expansion equations to a set of $(P+1)$ uncoupled and deterministic equations as shown in (4.22)-(4.23) for the H_x-field and E_x-field updates, and in (4.24)-(4.25) for the J_{ex}-field updates.

$$\begin{aligned} h_x^b|_{i,j+1/2,k+1/2}^{n+1/2} &= h_x^b|_{i,j+1/2,k+1/2}^{n-1/2} \\ &+ \frac{\Delta t}{\mu_0} \left[\frac{e_y^b|_{i,j+1/2,k+1}^{n} - e_y^b|_{i,j+1/2,k}^{n}}{\Delta z} - \frac{e_z^b|_{i,j+1,k+1/2}^{n} - e_z^b|_{i,j,k+1/2}^{n}}{\Delta y} \right] \end{aligned} \tag{4.22}$$

$$\begin{aligned} e_x^b|_{i+1/2,j,k}^{n+1} &= e_x^b|_{i+1/2,j,k}^{n} + \frac{\Delta t}{\epsilon_0} \left[\frac{h_z^b|_{i+1/2,j+1/2,k}^{n+1/2} - h_z^b|_{i+1/2,j-1/2,k}^{n+1/2}}{\Delta y} \right. \\ &\left. - \frac{h_y^b|_{i+1/2,j,k+1/2}^{n+1/2} - h_y^b|_{i+1/2,j,k-1/2}^{n+1/2}}{\Delta z} - j_{ex}^b|_{i+1/2,j,k}^{n+1/2} \right] \end{aligned} \tag{4.23}$$

For the Predictor step:

$$
\begin{aligned}
j^b_{ex,p}|^{n+1/2}_{i+1/2,j,k} = j^b_{ex}|^{n-1/2}_{i+1/2,j,k} &- \frac{1}{\langle \psi_b^2 \rangle} \sum_{a=0}^{P} \left(\left\langle \sin\theta \frac{\omega_{Cez}}{|\omega_{Ce}|} \psi_a(\xi)\psi_b(\xi) \right\rangle j^a_{ey}|^{n-1/2}_{i+1/2,j,k} \right. \\
&\left. - \left\langle \sin\theta \frac{\omega_{Cey}}{|\omega_{Ce}|} \psi_a(\xi)\psi_b(\xi) \right\rangle j^a_{ez}|^{n-1/2}_{i+1/2,j,k} \right) \\
&+ \frac{1}{\langle \psi_b^2 \rangle} \sum_{a=0}^{P} \left(\left\langle \tan\frac{\theta}{2}\sin\theta \frac{\omega_{Cez}\omega_{Cex}}{|\omega_{Ce}|^2} \psi_a(\xi)\psi_b(\xi) \right\rangle j^a_{ez}|^{n-1/2}_{i+1/2,j,k} \right. \\
&\left. - \left\langle \tan\frac{\theta}{2}\sin\theta \frac{\omega_{Cez}\omega_{Cez}}{|\omega_{Ce}|^2} \psi_a(\xi)\psi_b(\xi) \right\rangle j^a_{ex}|^{n-1/2}_{i+1/2,j,k} \right) \\
&- \frac{1}{\langle \psi_b^2 \rangle} \sum_{a=0}^{P} \left(\left\langle \tan\frac{\theta}{2}\sin\theta \frac{\omega_{Cey}\omega_{Cey}}{|\omega_{Ce}|^2} \psi_a(\xi)\psi_b(\xi) \right\rangle j^a_{ex}|^{n-1/2}_{i+1/2,j,k} \right. \\
&\left. - \left\langle \tan\frac{\theta}{2}\sin\theta \frac{\omega_{Cex}\omega_{Cey}}{|\omega_{Ce}|^2} \psi_a(\xi)\psi_b(\xi) \right\rangle j^a_{ey}|^{n-1/2}_{i+1/2,j,k} \right) \\
&+ \frac{\Delta t \epsilon_0}{\langle \psi_b^2 \rangle} \sum_{a=0}^{P} \left[\langle \omega_{Pe}^2 \psi_a(\xi)\psi_b(\xi) \rangle \, e^a_x|^n_{i+1/2,j,k} \right. \\
&\left. - \frac{1}{2} \left(\left\langle \omega_{Pe}^2 \sin\theta \frac{\omega_{Cez}}{|\omega_{Ce}|} \psi_a(\xi)\psi_b(\xi) \right\rangle e^a_y|^n_{i+1/2,j,k} - \left\langle \omega_{Pe}^2 \sin\theta \frac{\omega_{Cey}}{|\omega_{Ce}|} \psi_a(\xi)\psi_b(\xi) \right\rangle e^a_z|^n_{i+1/2,j,k} \right) \right] \\
&+ \frac{\Delta t \epsilon_0}{2\langle \psi_b^2 \rangle} \sum_{a=0}^{P} \left(\left\langle \omega_{Pe}^2 \tan\frac{\theta}{2}\sin\theta \frac{\omega_{Cez}\omega_{Cex}}{|\omega_{Ce}|^2} \psi_a(\xi)\psi_b(\xi) \right\rangle e^a_z|^n_{i+1/2,j,k} \right. \\
&\left. - \left\langle \omega_{Pe}^2 \tan\frac{\theta}{2}\sin\theta \frac{\omega_{Cez}\omega_{Cez}}{|\omega_{Ce}|^2} \psi_a(\xi)\psi_b(\xi) \right\rangle e^a_x|^n_{i+1/2,j,k} \right) \\
&- \frac{\Delta t \epsilon_0}{2\langle \psi_b^2 \rangle} \sum_{a=0}^{P} \left(\left\langle \omega_{Pe}^2 \tan\frac{\theta}{2}\sin\theta \frac{\omega_{Cey}\omega_{Cey}}{|\omega_{Ce}|^2} \psi_a(\xi)\psi_b(\xi) \right\rangle e^a_x|^n_{i+1/2,j,k} \right. \\
&\left. - \left\langle \omega_{Pe}^2 \tan\frac{\theta}{2}\sin\theta \frac{\omega_{Cex}\omega_{Cey}}{|\omega_{Ce}|^2} \psi_a(\xi)\psi_b(\xi) \right\rangle e^a_y|^n_{i+1/2,j,k} \right) \\
&+ \frac{\Delta t}{\langle \psi_b^2 \rangle} \sum_{a=0}^{P} \left[\langle v_e \psi_a(\xi)\psi_b(\xi) \rangle \, j^a_{ex}|^{n-1/2}_{i+1/2,j,k} \right. \\
&\left. - \frac{1}{2} \left(\left\langle v_e \sin\theta \frac{\omega_{Cez}}{|\omega_{Ce}|} \psi_a(\xi)\psi_b(\xi) \right\rangle j^a_{ey}|^{n-1/2}_{i+1/2,j,k} - \left\langle v_e \sin\theta \frac{\omega_{Cey}}{|\omega_{Ce}|} \psi_a(\xi)\psi_b(\xi) \right\rangle j^a_{ez}|^{n-1/2}_{i+1/2,j,k} \right) \right] \\
&+ \frac{\Delta t}{2\langle \psi_b^2 \rangle} \sum_{a=0}^{P} \left(\left\langle v_e \tan\frac{\theta}{2}\sin\theta \frac{\omega_{Cez}\omega_{Cex}}{|\omega_{Ce}|^2} \psi_a(\xi)\psi_b(\xi) \right\rangle j^a_{ez}|^{n-1/2}_{i+1/2,j,k} \right. \\
&\left. - \left\langle v_e \tan\frac{\theta}{2}\sin\theta \frac{\omega_{Cez}\omega_{Cez}}{|\omega_{Ce}|^2} \psi_a(\xi)\psi_b(\xi) \right\rangle j^a_{ex}|^{n-1/2}_{i+1/2,j,k} \right) \\
&- \frac{\Delta t}{2\langle \psi_b^2 \rangle} \sum_{a=0}^{P} \left(\left\langle v_e \tan\frac{\theta}{2}\sin\theta \frac{\omega_{Cey}\omega_{Cey}}{|\omega_{Ce}|^2} \psi_a(\xi)\psi_b(\xi) \right\rangle j^a_{ex}|^{n-1/2}_{i+1/2,j,k} \right. \\
&\left. - \left\langle v_e \tan\frac{\theta}{2}\sin\theta \frac{\omega_{Cex}\omega_{Cey}}{|\omega_{Ce}|^2} \psi_a(\xi)\psi_b(\xi) \right\rangle j^a_{ey}|^{n-1/2}_{i+1/2,j,k} \right)
\end{aligned}
\tag{4.24}
$$

For the Corrector step:

$$
\begin{aligned}
j^b_{ex,c}|^{n+1/2}_{i+1/2,j,k} = j^b_{ex}|^{n-1/2}_{i+1/2,j,k} &- \frac{1}{\langle \psi_b^2 \rangle} \sum_{a=0}^{P} \left(\left\langle \sin\theta \frac{\omega_{Cez}}{|\omega_{Ce}|} \psi_a(\xi)\psi_b(\xi) \right\rangle j^a_{ey}|^{n-1/2}_{i+1/2,j,k} \right. \\
&\left. - \left\langle \sin\theta \frac{\omega_{Cey}}{|\omega_{Ce}|} \psi_a(\xi)\psi_b(\xi) \right\rangle j^a_{ez}|^{n-1/2}_{i+1/2,j,k} \right) \\
&+ \frac{1}{\langle \psi_b^2 \rangle} \sum_{a=0}^{P} \left(\left\langle \tan\frac{\theta}{2}\sin\theta \frac{\omega_{Cez}\omega_{Cex}}{|\omega_{Ce}|^2} \psi_a(\xi)\psi_b(\xi) \right\rangle j^a_{ez}|^{n-1/2}_{i+1/2,j,k} \right. \\
&\left. - \left\langle \tan\frac{\theta}{2}\sin\theta \frac{\omega_{Cez}\omega_{Cez}}{|\omega_{Ce}|^2} \psi_a(\xi)\psi_b(\xi) \right\rangle j^a_{ex}|^{n-1/2}_{i+1/2,j,k} \right) \\
&- \frac{1}{\langle \psi_b^2 \rangle} \sum_{a=0}^{P} \left(\left\langle \tan\frac{\theta}{2}\sin\theta \frac{\omega_{Cey}\omega_{Cey}}{|\omega_{Ce}|^2} \psi_a(\xi)\psi_b(\xi) \right\rangle j^a_{ex}|^{n-1/2}_{i+1/2,j,k} \right. \\
&\left. - \left\langle \tan\frac{\theta}{2}\sin\theta \frac{\omega_{Cex}\omega_{Cey}}{|\omega_{Ce}|^2} \psi_a(\xi)\psi_b(\xi) \right\rangle j^a_{ey}|^{n-1/2}_{i+1/2,j,k} \right) \\
&+ \frac{\Delta t \epsilon_0}{\langle \psi_b^2 \rangle} \sum_{a=0}^{P} \left[\langle \omega_{Pe}^2 \psi_a(\xi)\psi_b(\xi) \rangle \, e^a_x|^n_{i+1/2,j,k} \right. \\
&\left. - \frac{1}{2} \left(\left\langle \omega_{Pe}^2 \sin\theta \frac{\omega_{Cez}}{|\omega_{Ce}|} \psi_a(\xi)\psi_b(\xi) \right\rangle e^a_y|^n_{i+1/2,j,k} - \left\langle \omega_{Pe}^2 \sin\theta \frac{\omega_{Cey}}{|\omega_{Ce}|} \psi_a(\xi)\psi_b(\xi) \right\rangle e^a_z|^n_{i+1/2,j,k} \right) \right] \\
&+ \frac{\Delta t \epsilon_0}{2\langle \psi_b^2 \rangle} \sum_{a=0}^{P} \left(\left\langle \omega_{Pe}^2 \tan\frac{\theta}{2}\sin\theta \frac{\omega_{Cez}\omega_{Cex}}{|\omega_{Ce}|^2} \psi_a(\xi)\psi_b(\xi) \right\rangle e^a_z|^n_{i+1/2,j,k} \right. \\
&\left. - \left\langle \omega_{Pe}^2 \tan\frac{\theta}{2}\sin\theta \frac{\omega_{Cez}\omega_{Cez}}{|\omega_{Ce}|^2} \psi_a(\xi)\psi_b(\xi) \right\rangle e^a_x|^n_{i+1/2,j,k} \right) \\
&- \frac{\Delta t \epsilon_0}{2\langle \psi_b^2 \rangle} \sum_{a=0}^{P} \left(\left\langle \omega_{Pe}^2 \tan\frac{\theta}{2}\sin\theta \frac{\omega_{Cey}\omega_{Cey}}{|\omega_{Ce}|^2} \psi_a(\xi)\psi_b(\xi) \right\rangle e^a_x|^n_{i+1/2,j,k} \right. \\
&\left. - \left\langle \omega_{Pe}^2 \tan\frac{\theta}{2}\sin\theta \frac{\omega_{Cex}\omega_{Cey}}{|\omega_{Ce}|^2} \psi_a(\xi)\psi_b(\xi) \right\rangle e^a_y|^n_{i+1/2,j,k} \right) \\
&+ \frac{\Delta t}{\langle \psi_b^2 \rangle} \sum_{a=0}^{P} \left[\langle v_e \psi_a(\xi)\psi_b(\xi) \rangle \, j^a_{ex,p}|^{n-1/2}_{i+1/2,j,k} \right. \\
&\left. - \frac{1}{2} \left(\left\langle v_e \sin\theta \frac{\omega_{Cez}}{|\omega_{Ce}|} \psi_a(\xi)\psi_b(\xi) \right\rangle j^a_{ey,p}|^{n-1/2}_{i+1/2,j,k} - \left\langle v_e \sin\theta \frac{\omega_{Cey}}{|\omega_{Ce}|} \psi_a(\xi)\psi_b(\xi) \right\rangle j^a_{ez,p}|^{n-1/2}_{i+1/2,j,k} \right) \right] \\
&+ \frac{\Delta t}{2\langle \psi_b^2 \rangle} \sum_{a=0}^{P} \left(\left\langle v_e \tan\frac{\theta}{2}\sin\theta \frac{\omega_{Cez}\omega_{Cex}}{|\omega_{Ce}|^2} \psi_a(\xi)\psi_b(\xi) \right\rangle j^a_{ez,p}|^{n-1/2}_{i+1/2,j,k} \right. \\
&\left. - \left\langle v_e \tan\frac{\theta}{2}\sin\theta \frac{\omega_{Cez}\omega_{Cez}}{|\omega_{Ce}|^2} \psi_a(\xi)\psi_b(\xi) \right\rangle j^a_{ex,p}|^{n-1/2}_{i+1/2,j,k} \right) \\
&- \frac{\Delta t}{2\langle \psi_b^2 \rangle} \sum_{a=0}^{P} \left(\left\langle v_e \tan\frac{\theta}{2}\sin\theta \frac{\omega_{Cey}\omega_{Cey}}{|\omega_{Ce}|^2} \psi_a(\xi)\psi_b(\xi) \right\rangle j^a_{ex,p}|^{n-1/2}_{i+1/2,j,k} \right. \\
&\left. - \left\langle v_e \tan\frac{\theta}{2}\sin\theta \frac{\omega_{Cex}\omega_{Cey}}{|\omega_{Ce}|^2} \psi_a(\xi)\psi_b(\xi) \right\rangle j^a_{ey,p}|^{n-1/2}_{i+1/2,j,k} \right)
\end{aligned}
\tag{4.25}
$$

Here, all inner products should be pre-calculated for all $a, b = 0, ..., P$ using numerical integration. Note that the multivariate polynomial chaos basis functions are constructed from tensor products of the univariate polynomials as follows

$$\psi_b(\boldsymbol{\xi}) = \prod_{i=1}^{n} \phi_{m_i^b}(\xi_i) \tag{4.26}$$

where $\phi_{m_i^b}(\xi_i)$ is a univariate orthogonal basis in ξ_i, and $m^b = \left[m_1^b, ..., m_n^b\right]$ is the multi-index of the polynomial ψ_b. Also, by using the multi-index definition and due to the statistical independence of the ξ's, the multivariate triple/quadruple products can be determined from the univariate triple/quadruple products. For example

$$\begin{aligned} &\langle v_e(\boldsymbol{\xi})\psi_b(\boldsymbol{\xi})\psi_c(\boldsymbol{\xi})\rangle \\ &= \left\langle \left(\prod_{i=1}^{n} v_e^i(\xi_i)\right)\left(\prod_{i=1}^{n} \phi_{m_i^a}(\xi_i)\right)\left(\prod_{i=1}^{n} \phi_{m_i^b}(\xi_i)\right)\right\rangle \\ &= \prod_{i=1}^{n} \left\langle v_e^i(\xi_i)\phi_{m_i^a}(\xi_i)\phi_{m_i^b}(\xi_i)\right\rangle \end{aligned} \tag{4.27}$$

where $v_e^i = \mu_{v_e} + \sigma_{v_e}\xi_2$ with $i = 2$ and $v_e^i = 1$ with $i \neq 2$. Now, the calculation of these inner products must be performed only once. Once the coefficients $e_u^a, h_u^a, j_u^a (u = x, y, z)$ are found, the mean and variance of the output fields can be obtained. The E_x field is provided as an example as

$$\mu\left[E_{x,i+1/2,j,k}(\boldsymbol{\xi})\right] = e^0_{x,i+1/2,j,k} \tag{4.28}$$

$$\sigma^2\left[E_{x,i+1/2,j,k}(\boldsymbol{\xi})\right] = \sum_{a=1}^{P} (e^a_{x,i+1/2,j,k})^2 \left\langle \psi_a^2 \right\rangle \tag{4.29}$$

4.2.3 Global sensitivities

Global sensitivities are calculated to assess the relative impact of each input parameter on the output electromagnetic fields of the PCE plasma model. Sobol indices are widely used in this context [97]. It is straightforward to compute global sensitivity indices of the model response related to the input parameters with a minimum computational cost via polynomial chaos expansion [64], [65]. The Sobol indices, for the output field E_x and the set of inputs u are given by [65]

$$S_u = \frac{\sum_{m \in K_u} (e^m_{x,i+1/2,j,k})^2 \left\langle \psi_m^2 \right\rangle}{\sigma^2\left[E_{x,i+1/2,j,k}(\boldsymbol{\xi})\right]} \tag{4.30}$$

where K_u is an index to the terms in (4.19) that contain u. For n input variables, (4.30) yields $2^n - 1$ indices and they all sum up to 1

$$\sum_{u \subseteq \{1,2,...,n\}} S_u = \sum_{i=1}^{n} S_i + \sum_{1 \leq i < j \leq n} S_{ij} + ... + S_{1,2,...,n} = 1 \tag{4.31}$$

Since this number becomes quickly large when n increases, and in order to avoid the need to consider too many sensitivity measures, in practice, it is more useful to define the total indices [98], namely S_{T_i} (which express the total sensitivity of the variance of the output field E_x due to each input variable ξ_i alone) and all its interactions with the other variables

$$S_{T_i} = \sum_{u \ni i} S_u \tag{4.32}$$

For example, in the case of three input parameters $n = 3$, we have $S_{T_1} = S_1 + S_{1,2} + S_{1,3} + S_{1,2,3}$.

4.3 Numerical examples

The performance of the PCE-based stochastic Galerkin approach for modeling uncertainty propagation in the fully 3D-FDTD magnetized cold plasma of Section 4.2.2 is evaluated by running a similar validation test as for the FDTD plasma model of [14]. An x-polarized, z-directed Gaussian-pulsed plane wave is implemented. Assuming that there is no uncertainty in the source, then the weighting coefficients of the source are implemented as

$$e^a_{x,source} = \begin{cases} \exp\left[\frac{-(t-50\Delta t)^2}{2(7\Delta t)^2}\right] & \text{if } a = 0 \\ 0 & \text{if } a > 0 \end{cases}$$

The lattice space increments in each Cartesian direction of the grid are $\Delta x = \Delta y = \Delta z = 1mm$, the time step $\Delta t = \Delta x/(c \times 0.55)$. A mean value of magnetic field $B = 0.06T$ is applied to the plasma (a large value so that we may observe an effect of the plasma over a short distance for validation purposes).

For validation, Monte Carlo simulations are used to predict the actual mean and standard deviation of the fields. First, the input electron densities n_e, collision frequency v_e and intensity of geomagnetic field B for each simulation are generated in a random manner with a normal distribution given by Table 4.1 (the standard deviation σ in the table is defined by $\%\sigma/\mu$). All of the simulation responses are collected and analyzed to obtain their

statistical properties (mean and standard deviation values). Then, using the PCE-based FDTD model, three separate simulation cases are run using Hermite polynomials of order $d = \{1, 2, 4\}$.

Figure 4.3 shows good agreement between the Monte Carlo and all three PCE-FDTD model results for the mean electric field E_x time-domain waveform as recorded 40 cells away from the source in the z-direction for the "small deviation" case of Table 4.1. The corresponding standard deviations for each case are shown in Figure 4.4. The results in Figure 4.4 indicate that in the early time, an order higher than $d = 2$ does not yield much improvement in the standard deviation agreement between the PCE model results and the Monte Carlo results. This is highlighted in Figure 4.5, which is a zoomed-in view of the early time results of Figure 4.4. The $d = 2$ and $d = 4$ results in Figure 4.4 are nearly identical, but the $d = 2$ case has the advantage of running faster than the $d = 4$ case. Finally, the late time results of Figure 4.4 illustrate that the late-time results are improved by using a higher-order PCE model. As the order is increased, however, the simulation time increases and eventually can be as long or longer than all of the Monte Carlo simulations.

Next, Figures 4.6 and 4.7 show the mean and standard deviation, respectively, of the electric field E_x recorded 40 cells away from the source in the z-direction when the deviation of each input parameter is increased by a factor of 5, corresponding to the "large deviation" case of Table 4.1. First, as would be expected, the standard deviation in Figure 4.7 has a higher amplitude than the "small deviation" standard deviation of Figure 4.4. Next, in the early time of Figures 4.6 and 4.7, at least an order $d = 4$ is required for the mean and the standard deviation to agree well with the Monte Carlo results. This is better shown in Figures 4.8 and 4.9, which are zoomed-in views of Figures 4.6 and 4.7, respectively. This finding is similar to the Monte Carlo method wherein higher standard deviations require an increased number of Monte Carlo simulations to converge to the same level of error. However, for the PCE-based Galerkin approach, only a single simulation is needed to obtain the complete statistical characterization of the fields, and only the accuracy depends on the order of the PCE (higher order leads to higher accuracy). Lastly, as time progresses, higher order PCE simulations may be desirable in order to obtain better agreement with the Monte Carlo results. This should only be pursued when long time-spans are of in-

terest, however, because the simulation time of the PCE models increases as the order is increased.

Using the methodology of 4.2.3, global sensitivities are calculated. Figure 4.10 shows the relative contribution of each input parameter to the uncertainty in E_x computed via (4.32). The uncertainty in E_x is dominated by the electron density n_e in the early time; whereas the geomagnetic field B has a greater impact in later times. Also, the modeling results indicate that the collision frequency variations influence the propagating electromagnetic waves far less than the geomagnetic field and the electron density variations. This agrees with the observations in [99], [100]. The figure also clearly demonstrates that the model is nonadditive and there is significant interactions between the parameters (as indicated by the contributions to the uncertainty extending above 1 on the y-axis). In other words, both the geomagnetic field and electron density are important, either when taken alone (i.e., first-order indices) or together (i.e higher-order indices). This may indicate that a higher order of the expansion in the PCE model and more Monte Carlo simulations may be required to improve accuracy of the results.

Table 4.2 compares the computational performance of the two methods. All simulations were performed on the Blue Waters supercomputer at the University of Illinois Urbana-Champaign using 1024 computational cores as well as identical time step increments and grid sizes in order to obtain a fair comparison. As seen in Table 4.2, the Monte Carlo method takes more than 10 times longer compared to the proposed PCE method in order to obtain reasonable agreement (comparing 1000 Monte Carlo simulations with the PCE simulation of order 2 for the "small deviation" case, and 5000 Monte Carlo simulations with the PCE simulation of order 4 for the "large deviation" case).

Until this point, a general multivariate PCE method has been considered that involves the variability of three input parameters: the electron density, the collision frequency and the geomagnetic field. For cases in which fewer variable input parameters are needed, the stochastic Lorentz equation for the predictor and corrector steps may be simplified. For example, when only electron density is modeled as an uncertain input parameter, then the equation reduces to the univariate random input parameter of the electron density as shown in (4.33) and (4.34). Accounting for only one random input variable (the electron density) greatly enhances the computational performance. For the PCE method, the mem-

ory consumption generally increases by a factor of $P+1$ and the simulation time increases by a factor of $(P+1)^2$.

4.4 Summary

The polynomial chaos expansion-based Galerkin approach was developed and applied to uncertainty quantification of electromagnetic wave propagation in magnetized cold plasma. The statistical characteristics (mean and standard deviation) of the electric and magnetic fields were studied under the effect of geomagnetic field and ionosphere content (i.e., electron density and collision frequency) variability. The PCE-FDTD results showed very good agreement with Monte Carlo results, especially in the early time results. In cases where late-time accuracy is needed, a higher order PCE model may be used. For the simulations in this chapter, the PCE-FDTD models ran more than 10 times faster than the corresponding Monte Carlo group of runs.

The tests of this chapter involved relatively large values (high amplitude background magnetic field) in order to efficiently observe effects of the magnetized plasma on the propagating electromagnetic wave over a short distance. However, the geomagnetic field in the PCE-FDTD model may be scaled in a straight-forward manner to actual geomagnetic field amplitudes in order to model electromagnetic wave propagation in the Earth-ionosphere waveguide. It may therefore serve as an important tool for reliably estimating electromagnetic wave propagation in an uncertain / variable ionosphere, especially for large 3-D plasma scenarios wherein Monte Carlo simulations would be impractical to run.

For the Predictor step:

$$
\begin{aligned}
j^c_{ex,p}|^{n+1/2}_{i+1/2,j,k} = j^c_{ex}|^{n-1/2}_{i+1/2,j,k} &- \frac{\sin\theta}{|\omega_{Ce}|}\left(j^c_{ey}|^{n-1/2}_{i+1/2,j,k}\omega_{Cez} - j^c_{ez}|^{n-1/2}_{i+1/2,j,k}\omega_{Cey}\right) \\
&+ \frac{\tan\frac{\theta}{2}\sin\theta}{|\omega_{Ce}|^2}\left[\left(j^c_{ez}|^{n-1/2}_{i+1/2,j,k}\omega_{Cex} - j^c_{ex}|^{n-1/2}_{i+1/2,j,k}\omega_{Cez}\right)\omega_{Cez}\right. \\
&\left. - \left(j^c_{ex}|^{n-1/2}_{i+1/2,j,k}\omega_{Cey} - j^c_{ey}|^{n-1/2}_{i+1/2,j,k}\omega_{Cex}\right)\omega_{Cey}\right] \\
-\Delta t v_e \left\{ j^c_{ex}|^{n-1/2}_{i+1/2,j,k} - \frac{\sin\theta}{2|\omega_{Ce}|}\right.&\left(j^c_{ey}|^{n-1/2}_{i+1/2,j,k}\omega_{Cez} - j^c_{ez}|^{n-1/2}_{i+1/2,j,k}\omega_{Cey}\right) \\
&+ \frac{\tan\frac{\theta}{2}\sin\theta}{2|\omega_{Ce}|^2}\left[\left(j^c_{ez}|^{n-1/2}_{i+1/2,j,k}\omega_{Cex} - j^c_{ex}|^{n-1/2}_{i+1/2,j,k}\omega_{Cez}\right)\omega_{Cez}\right. \\
&\left.\left. - \left(j^c_{ex}|^{n-1/2}_{i+1/2,j,k}\omega_{Cey} - j^c_{ey}|^{n-1/2}_{i+1/2,j,k}\omega_{Cex}\right)\omega_{Cey}\right]\right\} \\
+\frac{\Delta t q_e^2}{m_e\langle\psi_c^2\rangle}\sum_{a=0}^{P}\sum_{b=0}^{P} n_e^b\langle\psi_a(\xi)\psi_b(\xi)\psi_c(\xi)\rangle &\left\{ e^a_x|^n_{i+1/2,j,k} - \frac{\sin\theta}{2|\omega_{Ce}|}\left(e^a_y|^n_{i+1/2,j,k}\omega_{Cez} - e^a_z|^n_{i+1/2,j,k}\omega_{Cey}\right)\right. \\
&+ \frac{\tan\frac{\theta}{2}\sin\theta}{2|\omega_{Ce}|^2}\left[\left(e^a_z|^n_{i+1/2,j,k}\omega_{Cex} - e^a_x|^n_{i+1/2,j,k}\omega_{Cez}\right)\omega_{Cez}\right. \\
&\left.\left. - \left(e^a_x|^n_{i+1/2,j,k}\omega_{Cey} - e^a_y|^n_{i+1/2,j,k}\omega_{Cex}\right)\omega_{Cey}\right]\right\}
\end{aligned}
\tag{4.33}
$$

For the Corrector step:

$$
\begin{aligned}
j^c_{ex,c}|^{n+1/2}_{i+1/2,j,k} = j^c_{ex}|^{n-1/2}_{i+1/2,j,k} &- \frac{\sin\theta}{|\omega_{Ce}|}\left(j^c_{ey}|^{n-1/2}_{i+1/2,j,k}\omega_{Cez} - j^c_{ez}|^{n-1/2}_{i+1/2,j,k}\omega_{Cey}\right) \\
&+ \frac{\tan\frac{\theta}{2}\sin\theta}{|\omega_{Ce}|^2}\left[\left(j^c_{ez}|^{n-1/2}_{i+1/2,j,k}\omega_{Cex} - j^c_{ex}|^{n-1/2}_{i+1/2,j,k}\omega_{Cez}\right)\omega_{Cez}\right. \\
&\left. - \left(j^c_{ex}|^{n-1/2}_{i+1/2,j,k}\omega_{Cey} - j^c_{ey}|^{n-1/2}_{i+1/2,j,k}\omega_{Cex}\right)\omega_{Cey}\right] \\
-\Delta t v_e \left\{ j^c_{ex,p}|^{n+1/2}_{i+1/2,j,k} - \frac{\sin\theta}{2|\omega_{Ce}|}\right.&\left(j^c_{ey,p}|^{n+1/2}_{i+1/2,j,k}\omega_{Cez} - j^c_{ez,p}|^{n+1/2}_{i+1/2,j,k}\omega_{Cey}\right) \\
&+ \frac{\tan\frac{\theta}{2}\sin\theta}{2|\omega_{Ce}|^2}\left[\left(j^c_{ez,p}|^{n+1/2}_{i+1/2,j,k}\omega_{Cex} - j^c_{ex,p}|^{n+1/2}_{i+1/2,j,k}\omega_{Cez}\right)\omega_{Cez}\right. \\
&\left.\left. - \left(j^c_{ex,p}|^{n+1/2}_{i+1/2,j,k}\omega_{Cey} - j^c_{ey,p}|^{n+1/2}_{i+1/2,j,k}\omega_{Cex}\right)\omega_{Cey}\right]\right\} \\
+\frac{\Delta t q_e^2}{m_e\langle\psi_c^2\rangle}\sum_{a=0}^{P}\sum_{b=0}^{P} n_e^b\langle\psi_a(\xi)\psi_b(\xi)\psi_c(\xi)\rangle &\left\{ e^a_x|^n_{i+1/2,j,k} - \frac{\sin\theta}{2|\omega_{Ce}|}\left(e^a_y|^n_{i+1/2,j,k}\omega_{Cez} - e^a_z|^n_{i+1/2,j,k}\omega_{Cey}\right)\right. \\
&+ \frac{\tan\frac{\theta}{2}\sin\theta}{2|\omega_{Ce}|^2}\left[\left(e^a_z|^n_{i+1/2,j,k}\omega_{Cex} - e^a_x|^n_{i+1/2,j,k}\omega_{Cez}\right)\omega_{Cez}\right. \\
&\left.\left. - \left(e^a_x|^n_{i+1/2,j,k}\omega_{Cey} - e^a_y|^n_{i+1/2,j,k}\omega_{Cex}\right)\omega_{Cey}\right]\right\}
\end{aligned}
\tag{4.34}
$$

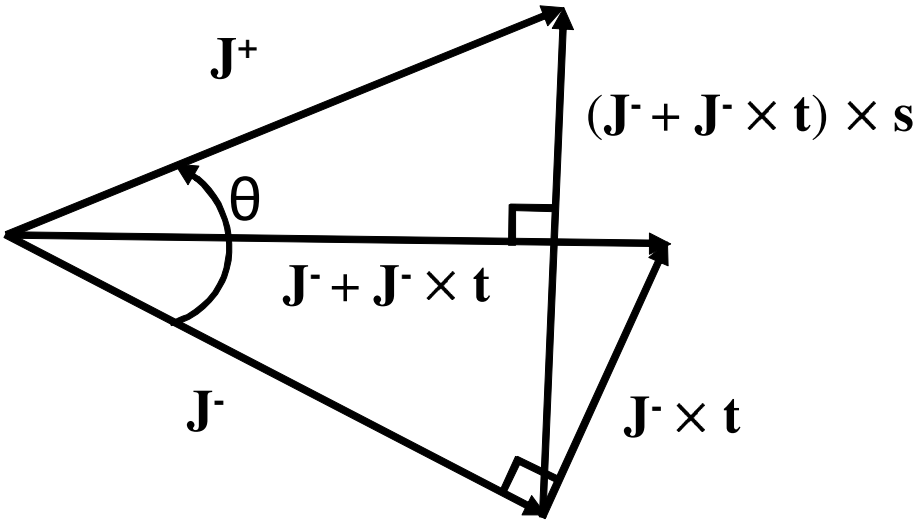

Figure 4.1: Rotation of current density vector.

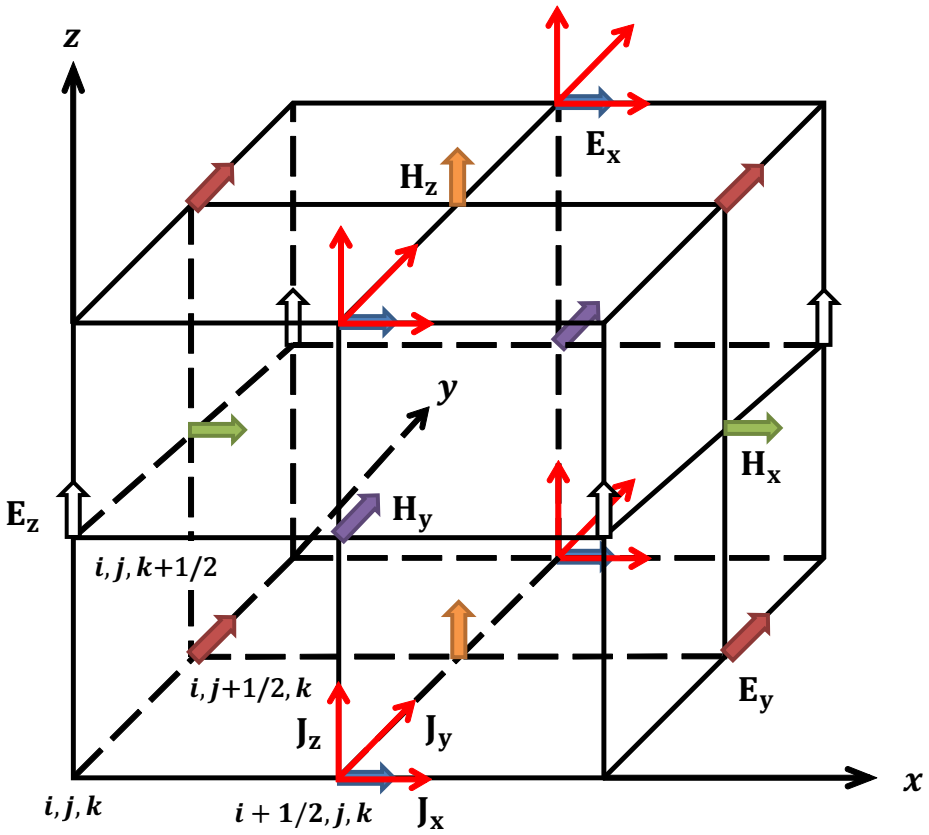

Figure 4.2: Yee cell illustrating the spatial positioning of the magnetized plasma field components.

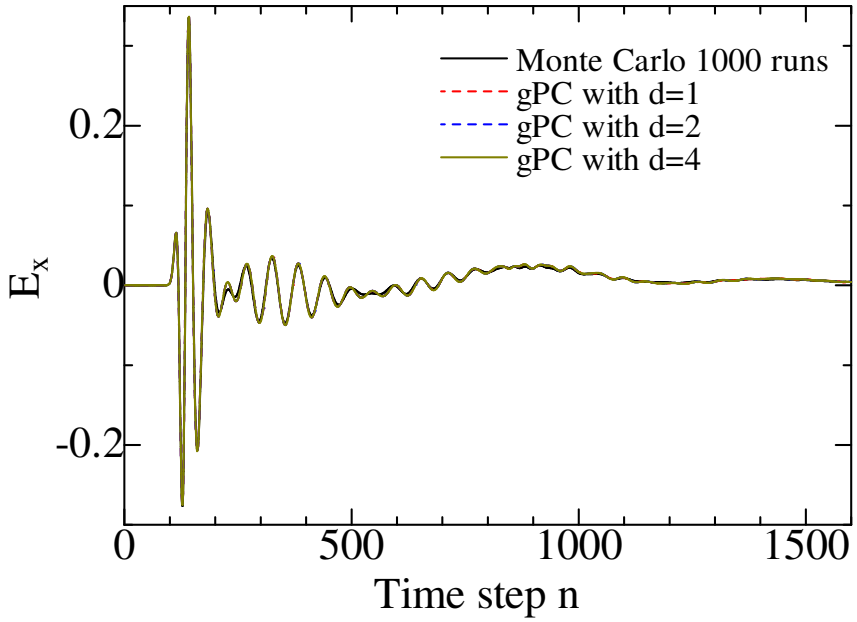

Figure 4.3: Mean of E_x for small input deviation case (observed at a point 40 cells away from the source).

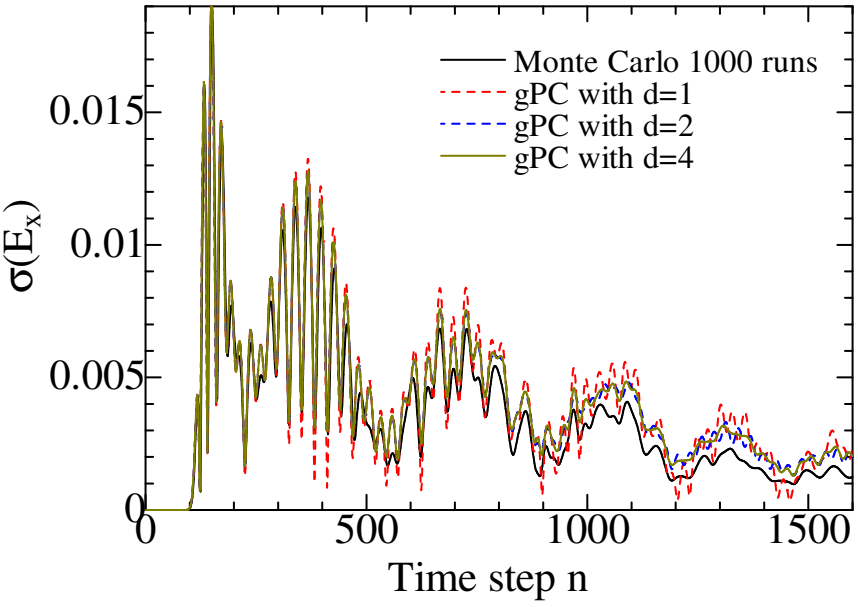

Figure 4.4: Standard deviation of E_x for small input deviation case (observed at a point 40 cells away from the source).

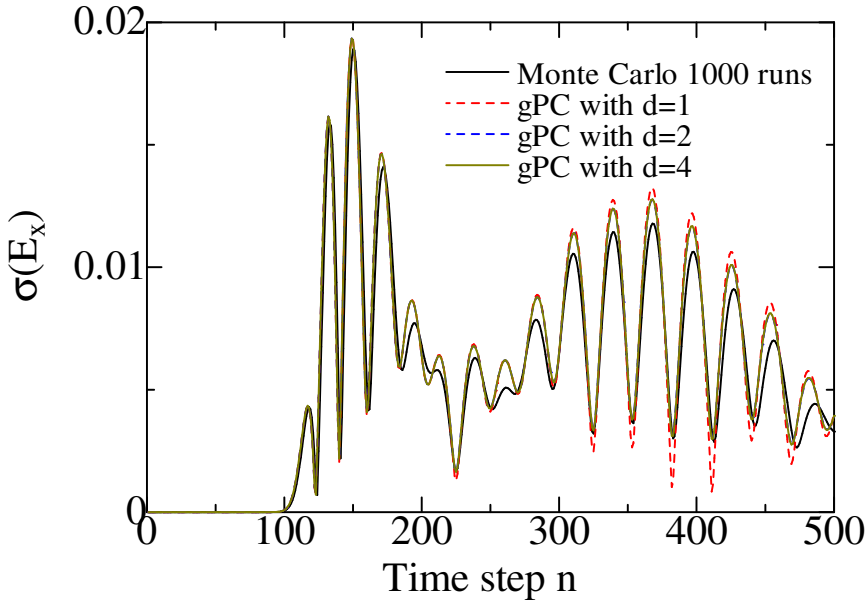

Figure 4.5: Standard deviation of E_x for small input deviation case at early time steps (observed at a point 40 cells away from the source).

Table 4.1: Input parameters and uncertainty

Case	Parameter	Mean value μ	Distribution
Small deviation	n_e	$1.0\times10^{18}(m^{-3})$	Gaussian, $\sigma = 2\%$
	v_e	$1.0\times10^{9}(1/s)$	Gaussian, $\sigma = 6\%$
	B	0.06 (T)	Gaussian, $\sigma = 4\%$
Large deviation	n_e	$1.0\times10^{18}(m^{-3})$	Gaussian, $\sigma = 10\%$
	v_e	$1.0\times10^{9}(1/s)$	Gaussian, $\sigma = 30\%$
	B	0.06 (T)	Gaussian, $\sigma = 20\%$

Table 4.2: Simulation time required by the MC and the proposed PCE-based methods

Method	Runs	Order d	Cores	Simulation time
MC	1000	-	1024	2 days 12 hours
MC	5000	-	1024	12 days 12 hours
PCE	1	1	1024	1 hour 03 mins
PCE	1	2	1024	5 hours 51 mins
PCE	1	4	1024	1 day 18 hours

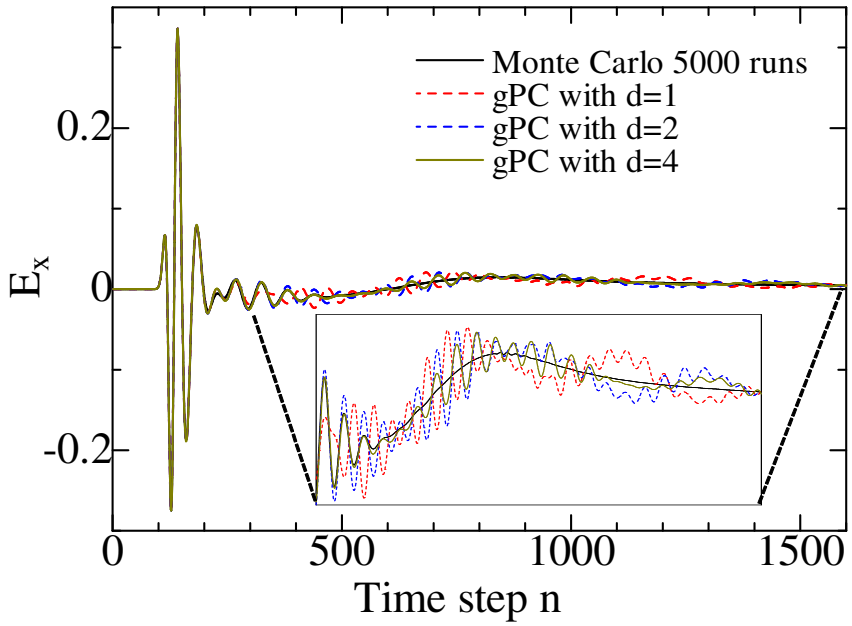

Figure 4.6: Mean of E_x for large input deviation case (observed at a point 40 cells away from the source).

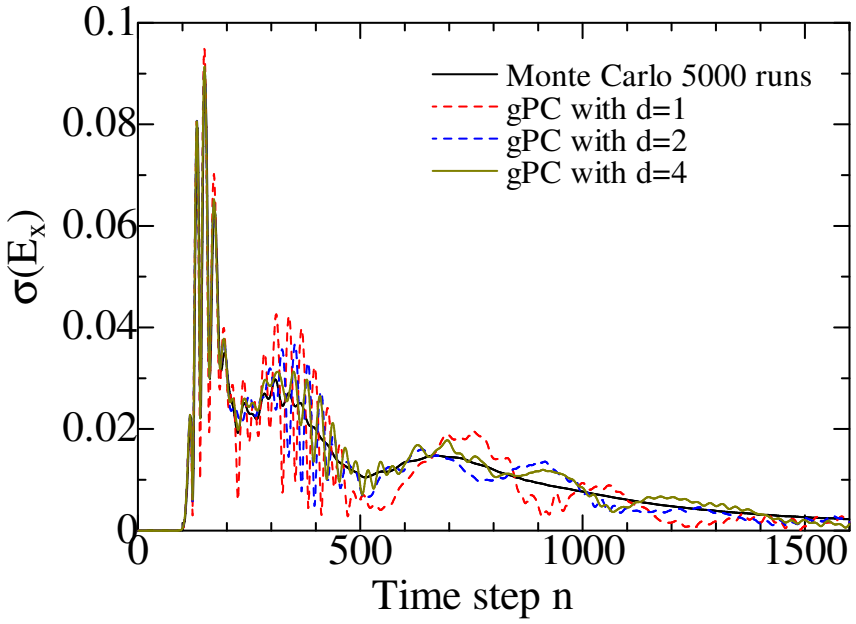

Figure 4.7: Standard deviation of E_x for large input deviation case (observed at a point 40 cells away from the source).

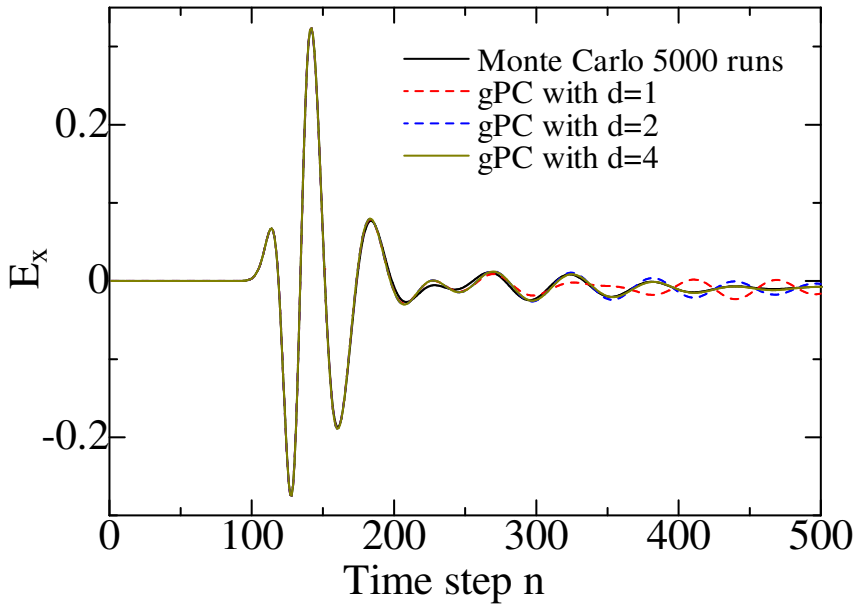

Figure 4.8: Mean of E_x for large input deviation case at early time steps (observed at a point 40 cells away from the source).

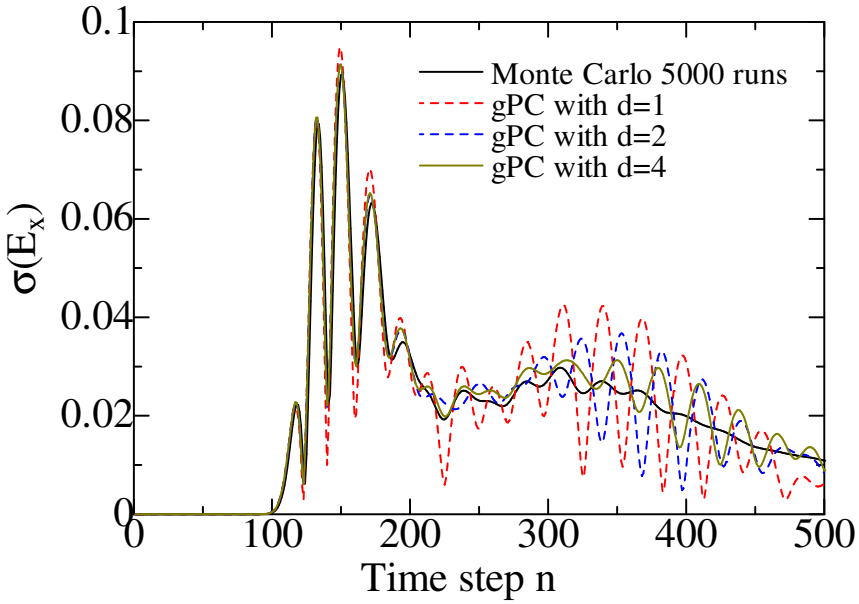

Figure 4.9: Standard deviation of E_x for large input deviation case at early time steps (observed at a point 40 cells away from the source).

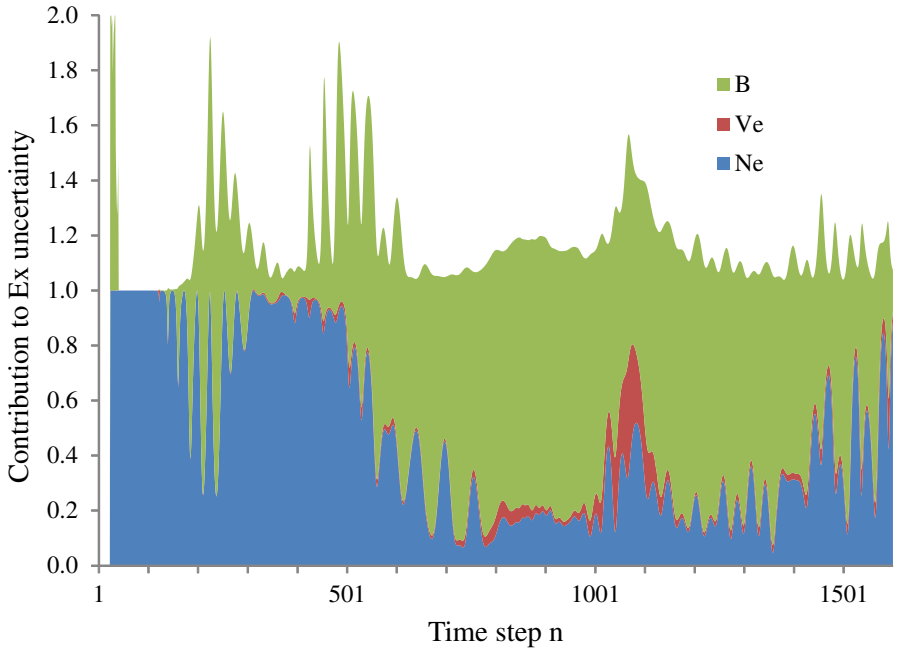

Figure 4.10: Relative contribution of each input parameter to the uncertainty computed using the order $d = 4$ expansion for large input deviation case.

CHAPTER 5

ANALYSIS OF ELECTROMAGNETIC WAVE PROPAGATION IN VARIABLE MAGNETIZED PLASMA VIA THE DELTA METHOD

5.1 Introduction

Several techniques have been proposed recently to solve uncertainty quantification problems involving the FDTD solution to Maxwell's equations. The approach in [101] proposes a single-realization scheme to obtain the ensemble average of the scattered fields. The advantage of the approach of [101] is that it makes use of an iterative technique to reformulate a multiplicative noise into an additive noise. However, the limitation of this algorithm is that it must meet the condition of a weakly scattering random medium, wherein the deviation from the mean electrical material values is small.

Another approach, e.g., [28], [62] and the works described in Chapter 3 and 4 of this dissertation, makes use of the generalized polynomial chaos (gPC) method, which is an extension of homogeneous chaos introduced by Wiener in 1938. The gPC expands the time-domain electric and magnetic fields in terms of orthogonal polynomial basis functions of the uncertain variables. The infinite sum of the polynomial chaos expansion is truncated to a finite number of terms P of orthogonal basis functions. The number of terms P is given by: $P+1 = (n+d)!/(n!d!)$, where d is the highest polynomial order in the expansion and n is number of random variables. It follows that P grows very quickly with the dimension and order of the decomposition. In general, the gPC method increases memory consumption by a factor $P+1$ and the simulation time proportional to $(P+1)^2$. The gPC results, however, typically converge significantly faster than the Monte Carlo method in a number of applications. It is also a mathematically robust method and has been proved to be effective in solving stochastic problems with Gaussian inputs as well as general non-Gaussian inputs. However, the method has an inherent limitation. It can

handle only a limited number of uncertain inputs. For large numbers of random variables, polynomial chaos becomes very computationally expensive and Monte-Carlo methods are typically more feasible.

Stochastic FDTD, namely S-FDTD, is an efficient formulation that makes use of the delta method [102] and runs the ensemble averages in a single realization scheme [103]. Reference [103] provides a direct estimate of both the mean and variance of the electromagnetic fields within layered biological media at every point in space and time. The advantage of this method is that it requires only about twice as much computer simulation time and memory as a traditional FDTD simulation regardless of the number of random variables. On the other hand, its limitation is that it can only bound the field variances according to a best estimate approximation for the cross correlation coefficients.

In summary, each of the above approaches has its own strengths and limitations. Given the fact that the ionosphere content can vary even up to 100% or more, the gPC method and the S-FDTD method proposed in [103] are good candidates for electromagnetic wave propagation modeling in ionosphere plasma. This chapter presents an alternative approach to the gPC method described in Chapter 4 and instead uses S-FDTD to represent the stochastic variability of the EM wave propagation in the magnetized cold plasma medium model.

An FDTD fully three-dimensional (3-D) anisotropic magnetized plasma model is reported in [14] for application to electromagnetic wave propagation in the ionosphere. This model solves Maxwell's equations coupled to current equations derived from the Lorentz equation of motion. By providing 3-D solutions, it yields the ability to simulate Faraday rotation and the complete 3-D spatial variations of the magnetized cold plasma. The accuracy, stability and formulation of this method is fully described in Sections I and II of [14]. In [15], the Cartesian magnetized plasma ionosphere algorithm of [14] is extended to the global latitude-longitude FDTD model of the Earth-ionosphere waveguide.

This chapter extends the methodology of Maxwell's equations S-FDTD [103] to Maxwell's equations coupled to the Lorentz equation of motion as in the 3-D FDTD magnetized plasma algorithm of [14]. We also propose an initial method for determining a good approximation for the cross correlation coefficients.

Although some previous works show that the collision frequencies vary in the lower

ionosphere due to solar activity, e.g., [85], [86], these variations are very small and affect the propagation of electromagnetic wave far less than the variation of electron density [99]. This statement is confirmed by the numerical result described in Chapter 4 of this dissertation. The modeling result in [100] also indicates a very small effect on sferic propagation when changing the collision frequencies by factor of 2. Moreover, in some aspects of space wave propagation, particularly in the higher ionosphere or magnetosphere where density of particles is low enough, the collision frequencies between charge particles can be negligible. In addition, this chapter only considers the wave propagation at early time steps in which the variation in E_x is dominated by the electron density n_e as shown in Chapter 4. Therefore, for the sake of simplicity, this chapter will do not consider variations of collision frequency and Earth's magnetic field, and electron density n_e is only random input parameter.

The new S-FDTD ionosphere plasma model presented here has broad potential applicability. The ability to determine not only the mean values of the ionospheric EM fields but also their variance will, for example, provide the capability of determining the confidence level that a communications / remote sensing / radar system will operate as expected under abnormal ionospheric conditions. It may also be useful in a wide variety of geophysical studies.

5.2 Methodology

5.2.1 Governing equations

The plasma algorithm methodology presented in [14] is identical for each electron, positive and negative ion species within the ionosphere. Since the effect of ions on EM wave propagation may sometimes be neglected, and to simplify the presentation of the S-FDTD ionosphere algorithm in this chapter, we will consider a simplified case of a plasma comprised of only electrons. The cold plasma is characterized by a free space permittivity and a free space permeability that is biased by an applied magnetic field, B.

The magnetized cold plasma governing equations are cast in terms of Maxwell's equations coupled to current equations derived from the Lorentz equation of motion. The resulting whole governing equation set is repeated here for convenience

$$\nabla \times \mathbf{E} = -\mu_0 \frac{\partial \mathbf{H}}{\partial t} \tag{5.1}$$

$$\nabla \times \mathbf{H} = \epsilon_0 \frac{\partial \mathbf{E}}{\partial t} + \mathbf{J}_e \tag{5.2}$$

$$\frac{\partial \mathbf{J}_e}{\partial t} + v_e \mathbf{J}_e = \epsilon_0 \omega_{Pe}^2 \mathbf{E} + \boldsymbol{\omega}_{Ce} \times \mathbf{J}_e \tag{5.3}$$

Here v_e, J_e, and ω_{Pe} are the collision frequency, the current density and the plasma frequency of electrons, respectively. The plasma frequency is given by

$$\omega_{Pe} = \sqrt{\frac{q_e^2 n_e}{\epsilon_0 m_e}} \tag{5.4}$$

It should be noted that the electron plasma frequency is a function of the electron density n_e. Ionosphere electron densities vary in a complex manner as a function of location and time. Thus, we consider the electron density as a random variable with its own statistical variation. This variability in the electron density causes variability in the EM fields, which will also be treated as random variables.

The current density can be written using Cartesian coordinates as

$$\mathbf{J}_e = J_{ex}\hat{x} + J_{ex}\hat{y} + J_{ex}\hat{z} \tag{5.5}$$

ω_{Ce} is the cyclotron frequency of the electrons given by $\boldsymbol{\omega}_{Ce} = |q_e|\mathbf{B}/m_e$ with a Cartesian coordinate expressions as

$$\boldsymbol{\omega}_{Ce} = \omega_{Cex}\hat{x} + \omega_{Cex}\hat{y} + \omega_{Cex}\hat{z} \tag{5.6}$$

Note also that the cyclotron frequency is a function of the applied magnetic field which is taken to be constant. Thus, the cross-product terms in (5.3) makes the plasma anisotropic so that the wave behavior depends on its propagation direction relative to the direction of the magnetic field.

5.2.2 Mean field equations

For the S-FDTD derivation, there are initially three stochastic equations (5.1), (5.2), and (5.3) that for Cartesian coordinates contain ten random variables for the 3-D case: E_x, E_y, E_z, H_x, H_y, H_z, J_{ex}, J_{ey}, J_{ez}, and ω_{Pe}. By using the delta method [102], Smith and Furse demonstrated that the average (or expected) fields can be found by solving the field equations using the mean or averages of the variables [103]. Analogously, we find for the

case of the S-FDTD magnetized cold plasma model that the equations for the mean values of the EM fields and current densities are also equal to those of the regular 3-D FDTD magnetized cold plasma model equations presented in [14], [104] (corresponding for the x-component case to equations (5.7), (5.8), and (5.9) of [104]), as follows

$$H_x|_{i,j+1/2,k+1/2}^{n+1/2} = H_x|_{i,j+1/2,k+1/2}^{n-1/2} + \frac{\Delta t}{\mu_0}\left[\frac{E_y|_{i,j+1/2,k+1}^{n} - E_y|_{i,j+1/2,k}^{n}}{\Delta z} - \frac{E_z|_{i,j+1,k+1/2}^{n} - E_z|_{i,j,k+1/2}^{n}}{\Delta y}\right] \tag{5.7}$$

$$E_x|_{i+1/2,j,k}^{n+1} + \frac{1}{2}\widehat{J}_{ex}|_{i+1/2,j,k}^{n+1} = E_x|_{i+1/2,j,k}^{n} - \frac{1}{2}\widehat{J}_{ex}|_{i+1/2,j,k}^{n} + \frac{(\Delta t)^2}{\epsilon_0\mu_0\Delta z}\left(\frac{\Delta\widehat{H}_z}{\Delta y}\right)_{i+1/2,j,k}^{n+1/2} - \frac{(\Delta t)^2}{\epsilon_0\mu_0\Delta y}\left(\frac{\Delta\widehat{H}_y}{\Delta z}\right)_{i+1/2,j,k}^{n+1/2} \tag{5.8}$$

$$\begin{aligned} &-\frac{(\omega_{Pe}\Delta t)^2}{2}E_x|_{i+1/2,j,k}^{n+1} + \left(1+\frac{v_e\Delta t}{2}\right)\widehat{J}_{ex}|_{i+1/2,j,k}^{n+1} + \frac{\omega_{cez}\Delta t}{2}\widehat{J}_{ey}|_{i+1/2,j,k}^{n+1} - \frac{\omega_{cey}\Delta t}{2}\widehat{J}_{ez}|_{i+1/2,j,k}^{n+1} \\ &= \frac{(\omega_{Pe}\Delta t)^2}{2}E_x|_{i+1/2,j,k}^{n} + \left(1-\frac{v_e\Delta t}{2}\right)\widehat{J}_{ex}|_{i+1/2,j,k}^{n} - \frac{\omega_{cez}\Delta t}{2}\widehat{J}_{ey}|_{i+1/2,j,k}^{n} + \frac{\omega_{cey}\Delta t}{2}\widehat{J}_{ez}|_{i+1/2,j,k}^{n} \end{aligned} \tag{5.9}$$

Thus, the mean EM field and current density values are found by using the mean plasma frequency of ω_{Pe}, or equivalently, the mean of electron density n_e. Note that the magnetic fields and current densities are scaled, such that $\widehat{H}_u = (\mu_0\Delta u/\Delta t)H_u[u = x, y, z]$ and $\widehat{J} = (\Delta t/\epsilon_0)J$, to avoid instabilities and inaccuracies caused by the large iteration coefficients. Note also for brevity, we use the notation

$$\left(\frac{\Delta\widehat{H}_z}{\Delta y}\right)_{i+1/2,j,k}^{n+1/2} = \frac{\widehat{H}_z|_{i+1/2,j+1/2,k}^{n+1/2} - \widehat{H}_z|_{i+1/2,j-1/2,k}^{n+1/2}}{\Delta y}$$

Further, the mean calculations presented here are a first-order accurate single-realization ensemble average scheme. The accuracy may be improved in the future by developing higher order methods that include the higher order terms from the Taylor series. However, the validation test cases presented in this chapter have demonstrated that the first-order accurate scheme is a very good approximation for magnetized cold plasma model. Moreover, the primary purpose of S-FDTD is to quantify the variance of the fields rather than the mean field values.

5.2.3 Variance field equations

When solving only Maxwell's equations, the variance field equations can be solved separately from the mean field equations no matter the dimensionality of the problem [105]. However, in the 3-D magnetized cold plasma model, the Lorentz equation (5.3) is coupled to the Maxwell equation (5.2), which leads to a complicated but linear system as can be seen in (5.8) and (5.9). As a result, the electric field and current density variances must be computed simultaneously. When variance equations are derived, covariances are needed of the E, H fields and current density J_e in both time and space. The equations also relate the electric field to the plasma frequency of the ionosphere, resulting in additional covariance terms between the electric field and the plasma frequency. For the S-FDTD method, a critical step is to approximate the correlation coefficients.

As for the 3-D Maxwell's equations S-FDTD methodology of [105], for the 3-D S-FDTD magnetized cold plasma algorithm, the magnetic fields, electric fields, and current densities are highly correlated to each other. As such, the correlation coefficients of the E, H fields and current density J_e may be approximated as 1. The approximation of the remaining correlation coefficients between the electric field and the plasma frequency will control the accuracy of the algorithm.

In order to derive the standard deviation (or variance) equations, we must take the variance of (5.7), (5.8), and (5.9). This step results in two cases. First, if a function is formed by the sum of multiple variables (equations (5.7) and (5.8)), its variance is

$$\sigma^2\left\{\sum_{i=1}^{n} a_i X_i\right\} = \sum_{i=1}^{n} a_i^2 \sigma^2\left\{X_i\right\} + 2\sum_{1\le i<j\le n}^{\sum\sum} a_i a_j \rho_{X_i,X_j}\sigma\left\{X_i\right\}\sigma\left\{X_j\right\} \tag{5.10}$$

Here, ρ_{X_i,X_j} is the correlation coefficient $(-1 \le \rho_{X_i,X_j} \le 1)$. The closer this coefficient is to zero, the more independent the terms are from each other. If the correlation coefficients $\rho_{X_i,X_j}(1 \le i < j \le n) = 1$, we obtain

$$\sigma^2\left\{\sum_{i=1}^{n} a_i X_i\right\} = \left[\sum_{i=1}^{n} a_i \sigma\left\{X_i\right\}\right]^2 \tag{5.11}$$

$$\text{or } \sigma\left\{\sum_{i=1}^{n} a_i X_i\right\} = \sum_{i=1}^{n} a_i \sigma\left\{X_i\right\} \tag{5.12}$$

Otherwise, if a function is formed by the product of multiple variables (equation (5.9)), its variance is solved by using the delta method [102]

$$\sigma^2 \left\{ f\left(X_1, X_2, \ldots, X_m\right) g\left(X_{m+1}, X_{m+2}, \ldots, X_{m+2}\right) \right\}$$
$$= \sum_{i=1}^{m+n} \sum_{j=1}^{m+n} \frac{\partial\left(fg\right)}{\partial X_i} \frac{\partial\left(fg\right)}{\partial X_j} \bigg|_{\mu_{X1}, \ldots, \mu_{Xm+n}} Cov\left(X_i, X_j\right) \tag{5.13}$$

Equations (5.12) and (5.13) will be used in the derivation of the variance equations (5.14), (5.15), and (5.17).

Now the S-FDTD plasma update equations will be derived, starting with the H-fields. For illustration purposes, only the update equation for the x-component of the H-field will be derived. We start by rearranging (5.7) and taking its variance. This yields

$$\sigma^2 \left\{ H_x|_{i,j+1/2,k+1/2}^{n+1/2} - H_x|_{i,j+1/2,k+1/2}^{n-1/2} \right\}$$
$$= \sigma^2 \left\{ \frac{\Delta t}{\mu_0} \left[\frac{E_y|_{i,j+1/2,k+1}^{n} - E_y|_{i,j+1/2,k}^{n}}{\Delta z} - \frac{E_z|_{i,j+1,k+1/2}^{n} - E_z|_{i,j,k+1/2}^{n}}{\Delta y} \right] \right\}$$

Applying the following approximations

$$\rho_{H_x|_{i,j+1/2,k+1/2}^{n+1/2}, H_x|_{i,j+1/2,k+1/2}^{n-1/2}} \approx \rho_{E_y|_{i,j+1/2,k+1}^{n}, E_y|_{i,j+1/2,k}^{n}} \approx \rho_{E_z|_{i,j+1,k+1/2}^{n}, E_z|_{i,j,k+1/2}^{n}} \approx 1$$

$$\rho_{E_y|_{i,j+1/2,k+1}^{n}, E_z|_{i,j+1,k+1/2}^{n}} \approx \rho_{E_y|_{i,j+1/2,k+1}^{n}, E_z|_{i,j,k+1/2}^{n}}$$
$$\approx \rho_{E_y|_{i,j+1/2,k}^{n}, E_z|_{i,j,k+1/2}^{n}} \approx \rho_{E_y|_{i,j+1/2,k}^{n}, E_z|_{i,j,k+1/2}^{n}} \approx 1$$

And applying (5.12) and rearranging, the resulting equation from taking the variance of (5.7) yields

$$\sigma\left\{ H_x|_{i,j+1/2,k+1/2}^{n+1/2} \right\} = \sigma\left\{ H_x|_{i,j+1/2,k+1/2}^{n-1/2} \right\}$$
$$+ \frac{\Delta t}{\mu_0} \left[\frac{\sigma\left\{ E_y|_{i,j+1/2,k+1}^{n} \right\} - \sigma\left\{ E_y|_{i,j+1/2,k}^{n} \right\}}{\Delta z} - \frac{\sigma\left\{ E_z|_{i,j+1,k+1/2}^{n} \right\} - \sigma\left\{ E_z|_{i,j,k+1/2}^{n} \right\}}{\Delta y} \right] \tag{5.14}$$

Next, we will work with equation (5.8). Again, for illustration purposes, we will only drive the update equations for the x-component of the fields. Rearranging (5.8) and taking its variance yields

$$\sigma^2 \left\{ E_x|_{i+1/2,j,k}^{n+1} - E_x|_{i+1/2,j,k}^{n} + \frac{1}{2}\widehat{J}_{ex}|_{i+1/2,j,k}^{n+1} + \frac{1}{2}\widehat{J}_{ex}|_{i+1/2,j,k}^{n} \right\}$$
$$= \sigma^2 \left\{ \frac{(\Delta t)^2}{\epsilon_0 \mu_0 \Delta z} \left(\frac{\Delta \widehat{H}_z}{\Delta y} \right)_{i+1/2,j,k}^{n+1/2} - \frac{(\Delta t)^2}{\epsilon_0 \mu_0 \Delta y} \left(\frac{\Delta \widehat{H}_y}{\Delta z} \right)_{i+1/2,j,k}^{n+1/2} \right\}$$

Applying the following approximations

$$\rho_{E_x|^{n+1}_{i+1/2,j,k},E_x|^{n}_{i+1/2,j,k}} \approx \rho_{\widehat{J}_{ex}|^{n+1}_{i+1/2,j,k},\widehat{J}_{ex}|^{n}_{i+1/2,j,k}} \approx \rho_{\left(\frac{\Delta\widehat{H}_z}{\Delta y}\right)^{n+1/2}_{i+1/2,j,k},\left(\frac{\Delta\widehat{H}_y}{\Delta z}\right)^{n+1/2}_{i+1/2,j,k}} \approx 1$$

$$\begin{aligned}\rho_{E_x|^{n+1}_{i+1/2,j,k},\widehat{J}_{ex}|^{n+1}_{i+1/2,j,k}} &\approx \rho_{E_x|^{n+1}_{i+1/2,j,k},\widehat{J}_{ex}|^{n}_{i+1/2,j,k}} \\ &\approx \rho_{E_x|^{n}_{i+1/2,j,k},\widehat{J}_{ex}|^{n+1}_{i+1/2,j,k}} \approx \rho_{E_x|^{n}_{i+1/2,j,k},\widehat{J}_{ex}|^{n}_{i+1/2,j,k}} \approx 1\end{aligned}$$

And applying (5.12) and rearranging, the resulting equation from taking the variance of (5.8) yields

$$\begin{aligned}\sigma\left\{E_x|^{n+1}_{i+1/2,j,k}\right\} + \frac{1}{2}\sigma\left\{\widehat{J}_{ex}|^{n+1}_{i+1/2,j,k}\right\} &= \sigma\left\{E_x|^{n}_{i+1/2,j,k}\right\} - \frac{1}{2}\sigma\left\{\widehat{J}_{ex}|^{n}_{i+1/2,j,k}\right\} \\ + \frac{(\Delta t)^2}{\epsilon_0\mu_0\Delta z}\sigma\left\{\left(\frac{\Delta\widehat{H}_z}{\Delta y}\right)^{n+1/2}_{i+1/2,j,k}\right\} &- \frac{(\Delta t)^2}{\epsilon_0\mu_0\Delta y}\sigma\left\{\left(\frac{\Delta\widehat{H}_y}{\Delta z}\right)^{n+1/2}_{i+1/2,j,k}\right\}\end{aligned} \tag{5.15}$$

Finally, we will work with the x-component equation of (5.9). Rearranging (5.9) and taking its variance yields

$$\begin{aligned}&\sigma^2\left\{\frac{(\omega_{pe}\Delta t)^2}{2}\left[E_x|^{n+1}_{i+1/2,j,k} + E_x|^{n}_{i+1/2,j,k}\right]\right\} \\ &= \sigma^2\left\{\left(1+\frac{v_e\Delta t}{2}\right)\widehat{J}_{ex}|^{n+1}_{i+1/2,j,k} - \left(1-\frac{v_e\Delta t}{2}\right)\widehat{J}_{ex}|^{n}_{i+1/2,j,k}\right. \\ &\left. + \frac{\omega_{cez}\Delta t}{2}\widehat{J}_{ey}|^{n+1}_{i+1/2,j,k} + \frac{\omega_{cez}\Delta t}{2}\widehat{J}_{ey}|^{n}_{i+1/2,j,k} - \frac{\omega_{cey}\Delta t}{2}\widehat{J}_{ez}|^{n+1}_{i+1/2,j,k} - \frac{\omega_{cey}\Delta t}{2}\widehat{J}_{ez}|^{n}_{i+1/2,j,k}\right\}\end{aligned} \tag{5.16}$$

Applying the following approximations

$$\begin{aligned}\rho_{E_x|^{n+1}_{i+1/2,j,k},E_x|^{n}_{i+1/2,j,k}} &\approx \rho_{\widehat{J}_{ex}|^{n+1}_{i+1/2,j,k},\widehat{J}_{ex}|^{n}_{i+1/2,j,k}} \\ &\approx \rho_{\widehat{J}_{ey}|^{n+1}_{i+1/2,j,k},\widehat{J}_{ey}|^{n}_{i+1/2,j,k}} \approx \rho_{\widehat{J}_{ez}|^{n+1}_{i+1/2,j,k},\widehat{J}_{ez}|^{n}_{i+1/2,j,k}} \approx 1\end{aligned}$$

$$\rho_{\widehat{J}_{ex}|^{n \text{ and } n+1}_{i+1/2,j,k},\widehat{J}_{ey}|^{n \text{ and } n+1}_{i+1/2,j,k}} \approx \rho_{\widehat{J}_{ex}|^{n \text{ and } n+1}_{i+1/2,j,k},\widehat{J}_{ez}|^{n \text{ and } n+1}_{i+1/2,j,k}} \approx \rho_{\widehat{J}_{ey}|^{n \text{ and } n+1}_{i+1/2,j,k},\widehat{J}_{ez}|^{n \text{ and } n+1}_{i+1/2,j,k}} \approx 1$$

From (5.13) and setting $E_x|^{n+1}_{i+1/2,j,k} + E_x|^{n}_{i+1/2,j,k} = E_x$, the left-hand side is computed using delta method, yielding

$$\sigma^2\left\{\frac{(\omega_{Pe}\Delta t)^2}{2}E_x\right\} \approx (\omega_{Pe}\Delta t^2)^2E_x^2\sigma^2\left\{\omega_{Pe}\right\}$$
$$+\left(\frac{\omega_{Pe}^2\Delta t^2}{2}\right)^2\sigma^2\left\{E_x\right\}+2\omega_{Pe}\Delta t^2\frac{\omega_{Pe}^2\Delta t^2}{2}E_x\rho_{\omega_{Pe},E_x}\sigma\left\{\omega_{Pe}\right\}\sigma\left\{E_x\right\}$$
$$=\left(\frac{\omega_{Pe}^2\Delta t^2}{2}\right)^2\sigma^2\left\{E_x\right\}+2\omega_{Pe}\Delta t^2\frac{\omega_{Pe}^2\Delta t^2}{2}E_x\rho_{\omega_{Pe},E_x}\sigma\left\{\omega_{Pe}\right\}\sigma\left\{E_x\right\}$$
$$+(\omega_{Pe}\Delta t^2)^2E_x^2\rho_{\omega_{Pe},E_x}^2\sigma^2\left\{\omega_{Pe}\right\}-(\omega_{Pe}\Delta t^2)^2E_x^2\rho_{\omega_{Pe},E_x}^2\sigma^2\left\{\omega_{Pe}\right\}+(\omega_{Pe}\Delta t^2)^2E_x^2\sigma^2\left\{\omega_{Pe}\right\}$$
$$=\left(\frac{\omega_{Pe}^2\Delta t^2}{2}\sigma\left\{E_x\right\}+\omega_{Pe}\Delta t^2\rho_{\omega_{Pe},E_x}\sigma\left\{\omega_{Pe}\right\}E_x\right)^2+(\omega_{Pe}\Delta t^2)^2E_x^2\sigma^2\left\{\omega_{Pe}\right\}\left(1-\rho_{\omega_{Pe},E_x}^2\right)$$

Neglecting the remainder term $(\omega_{Pe}\Delta t^2)^2E_x^2\sigma^2\left\{\omega_{Pe}\right\}\left(1-\rho_{\omega_{Pe},E_x}^2\right)$ we then have

$$\sigma^2\left\{\frac{(\omega_{Pe}\Delta t)^2}{2}E_x\right\}=\left(\frac{\omega_{Pe}^2\Delta t^2}{2}\sigma\left\{E_x\right\}+\omega_{Pe}\Delta t^2\rho_{\omega_{Pe},E_x}\sigma\left\{\omega_{Pe}\right\}E_x\right)^2$$

Since $\sigma\left\{E_x\right\}=\sigma\left\{E_x|_{i+1/2,j,k}^{n+1}\right\}+\sigma\left\{E_x|_{i+1/2,j,k}^{n}\right\}$, we arrive at

$$\begin{aligned}
&\frac{(\omega_{Pe}\Delta t)^2}{2}\left[\sigma\left\{E_x|_{i+1/2,j,k}^{n+1}\right\}+\sigma\left\{E_x|_{i+1/2,j,k}^{n}\right\}\right]\\
&\quad+\omega_{Pe}\Delta t^2\rho_{\omega_{Pe},E_x}\sigma\left\{\omega_{Pe}\right\}\left(E_x|_{i+1/2,j,k}^{n+1}+E_x|_{i+1/2,j,k}^{n}\right)\\
=&\quad\left(1+\frac{v_e\Delta t}{2}\right)\sigma\left\{\widehat{J}_{ex}|_{i+1/2,j,k}^{n+1}\right\}-\left(1-\frac{v_e\Delta t}{2}\right)\sigma\left\{\widehat{J}_{ex}|_{i+1/2,j,k}^{n}\right\}\\
&\quad+\frac{\omega_{cez}\Delta t}{2}\sigma\left\{\widehat{J}_{ey}|_{i+1/2,j,k}^{n+1}\right\}+\frac{\omega_{cez}\Delta t}{2}\sigma\left\{\widehat{J}_{ey}|_{i+1/2,j,k}^{n}\right\}\\
&\quad-\frac{\omega_{cey}\Delta t}{2}\sigma\left\{\widehat{J}_{ez}|_{i+1/2,j,k}^{n+1}\right\}-\frac{\omega_{cey}\Delta t}{2}\sigma\left\{\widehat{J}_{ez}|_{i+1/2,j,k}^{n}\right\}
\end{aligned}$$

Rearranging, the resulting equation from taking the variance of (5.9) yields

$$\begin{aligned}
&-\frac{(\omega_{Pe}\Delta t)^2}{2}\sigma\left\{E_x|_{i+1/2,j,k}^{n+1}\right\}+\left(1+\frac{v_e\Delta t}{2}\right)\sigma\left\{\widehat{J}_{ex}|_{i+1/2,j,k}^{n+1}\right\}\\
&\quad+\frac{\omega_{cez}\Delta t}{2}\sigma\left\{\widehat{J}_{ey}|_{i+1/2,j,k}^{n+1}\right\}-\frac{\omega_{cey}\Delta t}{2}\sigma\left\{\widehat{J}_{ez}|_{i+1/2,j,k}^{n+1}\right\}\\
=&\quad\omega_{Pe}\Delta t^2\rho_{\omega_{Pe},E_x}\sigma\left\{\omega_{Pe}\right\}E_x|_{i+1/2,j,k}^{n+1}+\omega_{Pe}\Delta t^2\rho_{\omega_{Pe},E_x}\sigma\left\{\omega_{Pe}\right\}E_x|_{i+1/2,j,k}^{n}\\
&\quad+\frac{(\omega_{Pe}\Delta t)^2}{2}\sigma\left\{E_x|_{i+1/2,j,k}^{n}\right\}+\left(1-\frac{v_e\Delta t}{2}\right)\sigma\left\{\widehat{J}_{ex}|_{i+1/2,j,k}^{n}\right\}\\
&\quad-\frac{\omega_{cez}\Delta t}{2}\sigma\left\{\widehat{J}_{ey}|_{i+1/2,j,k}^{n}\right\}+\frac{\omega_{cey}\Delta t}{2}\sigma\left\{\widehat{J}_{ez}|_{i+1/2,j,k}^{n}\right\}
\end{aligned}\tag{5.17}$$

Although only the x-component equations are derived here, analogous equations can be obtained for the y-component and z-component equations.

Since both the electric field E_x and its deviation $\sigma(E_x)$ are in equation (5.17), all of the state variables for the deviations of E and J_e will depend on the mean of electric field

E as well. All of the required equations can be combined to 18 scalar equations with 18 state variables. After the discretization of these equations using $E-J$ collocation, these equations can be divided into three groups. The first group consists of 6 difference equations for the magnetic field H and its deviation $\sigma(H)$ update similar to equations (5.7) and (5.14) given for H_x. The second group consists 6 linear equations of all the components of $E,\ J$, which can be given as

$$\begin{bmatrix} E_x|^{n+1}_{i+1/2,j,k} \\ E_y|^{n+1}_{i,j+1/2,k} \\ E_z|^{n+1}_{i,j,k+1/2} \\ \widehat{J}_x|^{n+1}_{i+1/2,j,k} \\ \widehat{J}_y|^{n+1}_{i,j+1/2,k} \\ \widehat{J}_z|^{n+1}_{i,j,k+1/2} \end{bmatrix} = \left[A^{-1}B\right] \begin{bmatrix} E_x^n \\ E_y^n \\ E_z^n \\ \widehat{J}_x^n \\ \widehat{J}_y^n \\ \widehat{J}_z^n \end{bmatrix} + \left[A^{-1}C\right] \begin{bmatrix} \left(\frac{\Delta \widehat{H}_z}{\Delta y}\right)^{n+1/2} \\ \left(\frac{\Delta \widehat{H}_y}{\Delta z}\right)^{n+1/2} \\ \left(\frac{\Delta \widehat{H}_x}{\Delta z}\right)^{n+1/2} \\ \left(\frac{\Delta \widehat{H}_z}{\Delta x}\right)^{n+1/2} \\ \left(\frac{\Delta \widehat{H}_y}{\Delta x}\right)^{n+1/2} \\ \left(\frac{\Delta \widehat{H}_x}{\Delta y}\right)^{n+1/2} \end{bmatrix} \tag{5.18}$$

Finally, the third group consists 6 linear equations of all the components of $\sigma(E)$, $\sigma(J)$, which can be given as

$$\begin{bmatrix} \sigma\left\{E_x|^{n+1}_{i+1/2,j,k}\right\} \\ \sigma\left\{E_y|^{n+1}_{i,j+1/2,k}\right\} \\ \sigma\left\{E_z|^{n+1}_{i,j,k+1/2}\right\} \\ \sigma\left\{\widehat{J}_x|^{n+1}_{i+1/2,j,k}\right\} \\ \sigma\left\{\widehat{J}_y|^{n+1}_{i,j+1/2,k}\right\} \\ \sigma\left\{\widehat{J}_z|^{n+1}_{i,j,k+1/2}\right\} \end{bmatrix} = \left[A^{-1}B\right] \begin{bmatrix} \sigma\{E_x^n\} \\ \sigma\left\{E_y^n\right\} \\ \sigma\{E_z^n\} \\ \sigma\left\{\widehat{J}_x^n\right\} \\ \sigma\left\{\widehat{J}_y^n\right\} \\ \sigma\left\{\widehat{J}_z^n\right\} \end{bmatrix} + \left[A^{-1}C\right] \begin{bmatrix} \sigma\left\{\left(\frac{\Delta \widehat{H}_z}{\Delta y}\right)^{n+1/2}\right\} \\ \sigma\left\{\left(\frac{\Delta \widehat{H}_y}{\Delta z}\right)^{n+1/2}\right\} \\ \sigma\left\{\left(\frac{\Delta \widehat{H}_x}{\Delta z}\right)^{n+1/2}\right\} \\ \sigma\left\{\left(\frac{\Delta \widehat{H}_z}{\Delta x}\right)^{n+1/2}\right\} \\ \sigma\left\{\left(\frac{\Delta \widehat{H}_y}{\Delta x}\right)^{n+1/2}\right\} \\ \sigma\left\{\left(\frac{\Delta \widehat{H}_x}{\Delta y}\right)^{n+1/2}\right\} \end{bmatrix} + \left[A^{-1}D\right] \begin{bmatrix} E_x^{n+1} \\ E_y^{n+1} \\ E_z^{n+1} \\ E_x^n \\ E_y^n \\ E_z^n \end{bmatrix} \tag{5.19}$$

where $A[6\times 6]$, $B[6\times 6]$, $C[6\times 6]$, and $D[6\times 6]$ are the coefficient matrixes that depend on the plasma properties and the modeling parameters (equations A.1-A.4). Note that in this derivation, $E-J$ collocation is utilized, such that $\{E,\ J,\ \sigma(E),\ \sigma(J)\}$ are all at the same locations, and $\{H,\ \sigma(H)\}$ are located at the same positions as shown in Figure 5.1.

Figure 5.2 shows a diagram of the iteration process for each time step. What is changed from the regular FDTD update is the addition of the calculation of the variances after the mean values are obtained. Also, since both the mean fields and their variances behave like waves, both require boundary conditions. Thus, the Mur's boundary condition developed

for the magnetized plasma as implemented in [106] is applied to the S-FDTD variance values as well as to the mean values.

5.3 Validation of the algorithm

The performance of the fully 3-D S-FDTD cold plasma model of Section 5.2 is evaluated by running a similar validation test as for the FDTD plasma model of [14]. An x-polarized, z-directed Gaussian-pulsed plane wave is modeled using

$$E_x = exp\left[\frac{-(t-50\Delta t)^2}{2(7\Delta t)^2}\right] \tag{5.20}$$

The lattice space increments in each Cartesian direction of the grid are $\Delta x = \Delta y = \Delta z = 1mm$, the time step $\Delta t = \Delta x/(c \times 0.55)$. The plasma medium has a mean electron density $\mu_{n_e} = 1.0 \times 10^{18} m^{-3}$, and the assumed electron density has a statistical variation given by $\sigma\{n_e\} = 2.0 \times 10^{16} m^{-3}$ (equivalently $\%\sigma\{n_e\} = 2.0$). A constant magnetic field $B = 0.06T$ is applied to the plasma as for the validation tests of [14]. For simplicity, a collisionless plasma is tested. This large magnetic field value (relative to the geomagnetic field as would be applied to the ionosphere) is used so that we can see a strong effect of the plasma over a short propagation distance and permit a smaller simulation. The E_x field component shown in Figure 5.3 is recorded 10-cells away from the source in the z-direction. The standard deviation and the variance are both important parameters which measure the spread of the distribution about the mean. The standard deviation and variance of the E_x field are shown in Figure 5.4 and Figure 5.5, respectively.

For validation, 100 Monte Carlo simulations is used to predict the exact mean, standard deviation and variance of the fields. The input electron densities n_e for each simulation are generated in a random manner with a normal distribution given by

$$f(n_e) = \frac{1}{\sqrt{2\pi\sigma^2\{n_e\}}} e^{\left\{\frac{-(n_e-\mu_{n_e})^2}{2\sigma^2\{n_e\}}\right\}} \tag{5.21}$$

All of the simulation responses are collected and analyzed to obtain their statistical properties (mean, standard deviation, and variance values). Then, using S-FDTD, three separate simulation cases are run using approximations for the correlation coefficients between the plasma frequency and the electric fields of 1, 0.5 and 0.05, respectively.

In Figure 5.3, there is a strong agreement between the mean values of the Monte Carlo and S-FDTD results. That is, it is found that evaluating the mean values using numbers

generated by the random generator is consistent with the mean values obtained directly from the Maxwell's equations / current equation solutions. Figure 5.4 shows that a higher correlation coefficient leads to a higher standard deviation (or variance) of the electric field. As expected, the approximations for the cross correlation of the plasma frequency and the electric fields have a direct impact on the accuracy of the S-FDTD method. The correlation coefficient of 1.0 yields a maximum (upper bound) of the variance. In this data set, a cross correlation value of 0.05 provides the best agreement with the Monte Carlo simulations as shown in Figure 5.5.

It is challenging to decide which method should be used to evaluate the cross correlation coefficients. So far we have considered the correlation coefficients between the plasma frequency and each of the three components of the E field to be equal. Now instead, Figure 5.6 shows results for cases wherein the correlation coefficients are not identical for each of the three Cartesian directions. For example, if we keep $\rho_{\omega,E_x} = 0.05$ and change ρ_{ω,E_y} and ρ_{ω,E_z} to 0, Figure 5.6 clearly shows that the variance of the E field mainly depends on ρ_{ω,E_x}. This can be explained as follows: For an x-polarized, z-directed plane wave, the E_z component is always equal to zero with any value of electron density. The ρ_{ω,E_z}, therefore, should also be equal to zero, since a variable and a constant are always independent. Moreover, when the E_x component is much larger than the E_y component, the value of ρ_{ω,E_x} primarily affects the variance of the field. Note that for a wave that is undergoing Faraday rotation, the E_x and E_y component amplitudes could change with propagation distance. It appears that there are many factors in choosing the best $\rho_{\omega,E}$ values, such as the field component orientation, the cell's location relative to the source, the type of source wave, and the direction of the background magnetic field.

Next, the $\%\sigma\{n_e\}$ is gradually increased from 2 to 8. Figure 5.7 graphs the resulting change in the ρ_{ω,E_x} required for the S-FDTD simulations in order to provide a good agreement with Monte Carlo results. We can see that there is a linear relationship between the choice of correlation coefficients for this range of $\%\sigma\{n_e\}$. We also observe similar trends when changing other input parameters such as the source or mean value of the electron density.

The results shown in Figure 5.7 provide an indication as to how to set the cross correlation coefficient values in the S-FDTD code. That is, two Monte Carlo simulations along

with the linear property observed in Figure 5.7 can be used to predict the correlation coefficients for an S-FDTD model having an ionosheric plasma at least within the weak scattering range (having for example $\%\sigma\{n_e\} = 1$ and 2). Note that a relatively small number of simulations is needed for the Monte Carlo method to obtain reasonably accurate results in the cases wherein the standard deviation is small. In contrast, the Monte Carlo method for validating the linear property of the S-FDTD algorithm in the cases of large standard deviation presents a much more significant challenge. More specifically, in a Monte Carlo simulation, the standard error of the mean of the distribution is:

$$error_{mean} = \frac{Z \times \sigma_p}{\sqrt{runs}} \tag{5.22}$$

where, Z is to the confidence multiplier of a two-tailed normal distribution. For a 95% confidence, $Z = 2$. For 99%, $Z = 3$, etc. σ_p is the portfolio's standard deviation. The *runs* term represents the number of runs in the Monte Carlo simulation. Thus, the error is higher for either a high standard deviation or a small number of runs. Note the accuracy improves as the square root of the ratio of the number of additional runs. As a consequence, tens of thousands of simulations are necessary for Monte Carlo validations when increasing $\%\sigma\{n_e\}$ up to 100 or more. Monte Carlo simulations of 3-D magnetized plasma model for more dense plasma may thus be prohibitively computationally expensive.

As part of future research, systematic studies will be performed to evaluate the best methodology for determining the appropriate correlation coefficients for a wider variety of plasma modeling scenarios. In the S-FDTD methodology of [103] applied to only Maxwell's equations, the correlation coefficients were set to neighboring reflection coefficients. For the modeling presented in this chapter, however, there are no reflection surfaces, and so there are no reflection coefficients that can be used for the correlation coefficients. Further, when applied to the ionosphere, the S-FDTD plasma model will use ionospheric parameters that will continuously vary with position and altitude. As a result, a different and more advanced methodology must be followed for determining the appropriate correlation coefficients between the electric field and the plasma frequency. Extensive studies and simulations will be performed as part of future research to develop these best approximations for the correlation coefficients.

Additionally, by running a similar numerical example for the PCE-plasma simulation

developed in the Chapter 4, compared to a single deterministic simulation, a PCE simulation for order $d = 1$ takes ~ 5 times longer and for order $d = 4$ takes ~ 21.5 times longer. Alternatively, to take advantage of the benefits of the different stochastic modeling approaches, it may possible to create a hybrid method to achieve optimal and efficient results. For example, the PCE method could help the S-FDTD simulations by providing correlation coefficients for cases involving larger deviations of electron density wherein a Monte Carlo validation is extremely inefficient. Note that the computational performance of the S-FDTD method is better than the PCE method since it requires only about twice as much computer simulation time and memory as a traditional FDTD simulation regardless of numbers of random variables. Overall, the ultimate objective is to develop a stochastic optimization FDTD-based algorithm that is well-suited for large uncertainty quantification of the ionosphere, so that the variability of the EM wave propagation is well understood.

5.4 Summary

A 3-D Stochastic FDTD (S-FDTD) model of EM wave propagation in anisotropic magnetized cold plasma was introduced. The plasma S-FDTD model of this chapter is an extension of the S-FDTD model developed by Smith and Furse for Maxwell's equations and applied to biomedical applications [103], [105]. The plasma S-FDTD model of this chapter is derived from Maxwells equations coupled to the current equations derived from the Lorentz equation of motion. When applied to the ionosphere, it uses as input not only average electron (or ion) densities, but also their variance due to uncertainties or variances due to factors such as space weather events.

S-FDTD offers an exceptional improvement in simulation time compared to the brute-force MC method. S-FDTD may therefore serve as an important tool for EM ionospheric propagation studies, especially for large 3-D plasma scenarios where Monte Carlo simulations would be impractical to run. Example S-FDTD simulation results were provided and compared to MC results. Different cross correlation values for the electric fields and the plasma frequency were tested. An upper bound of the variance was obtained by setting these cross correlation values to 1.0. Future research will be conducted to provide the best methodology for determining these cross correlation values for different modeling scenarios, particularly for the complex cases of a continuously varying ionosphere.

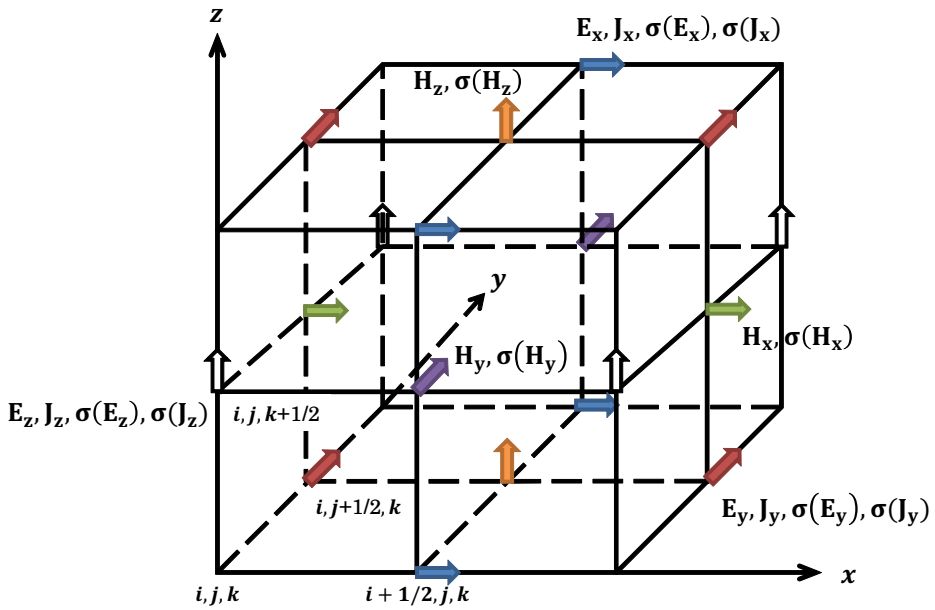

Figure 5.1: Yee cell (including stochastic variables) indicating the spatial positioning of the field components.

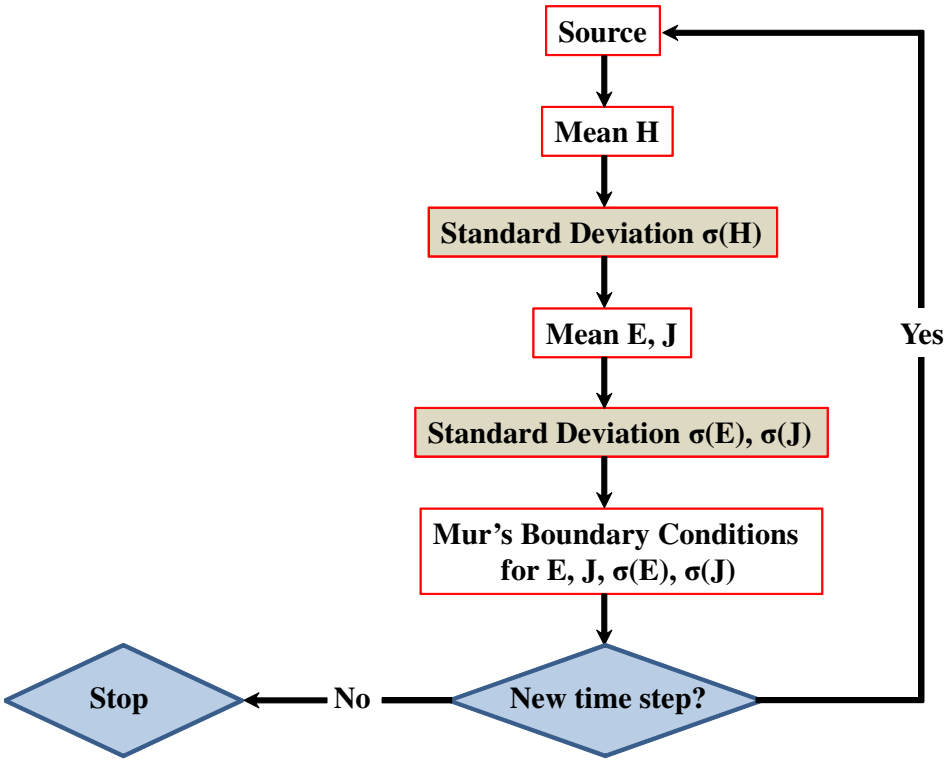

Figure 5.2: S-FDTD flow chart.

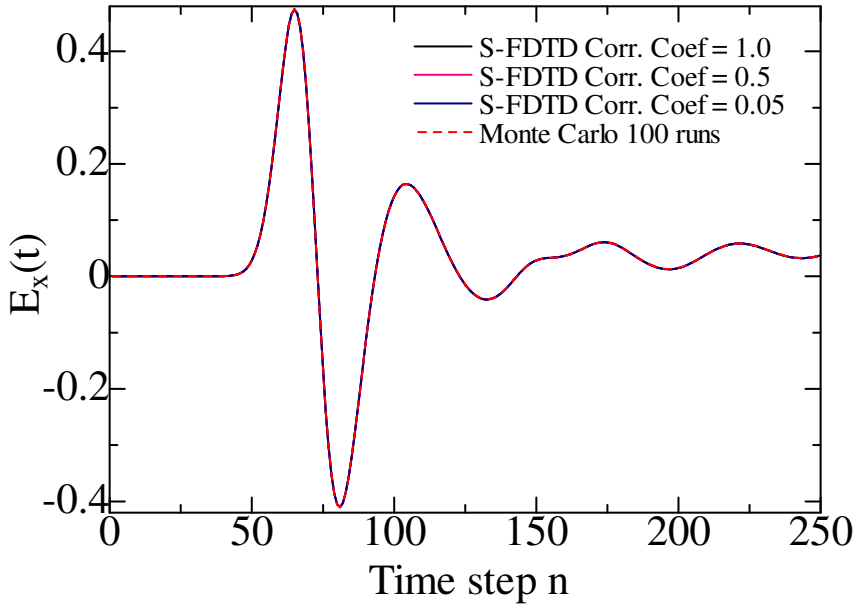

Figure 5.3: Mean of E_x (observed at a point 10 cells away from the source).

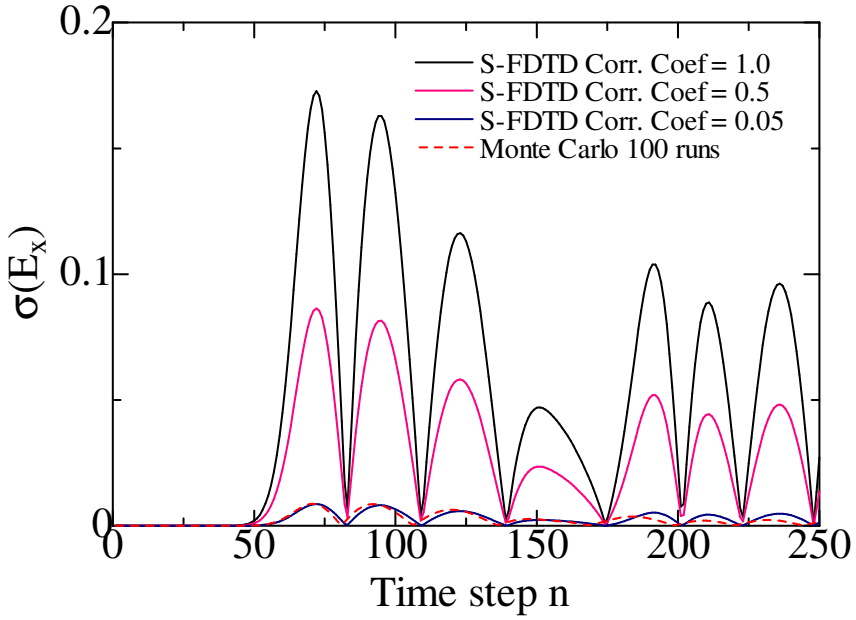

Figure 5.4: Standard deviation of E_x (observed at a point 10 cells away from the source).

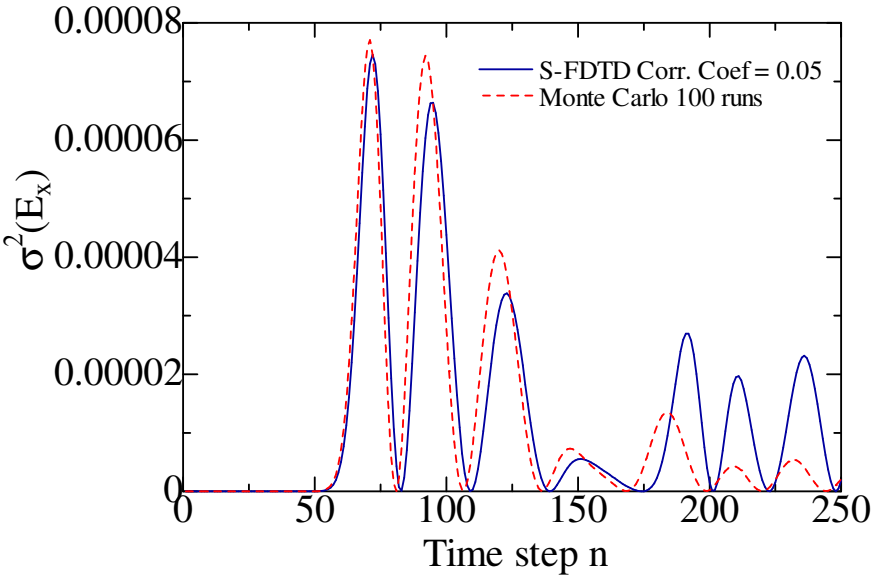

Figure 5.5: Variance of E_x (observed at a point 10 cells away from the source).

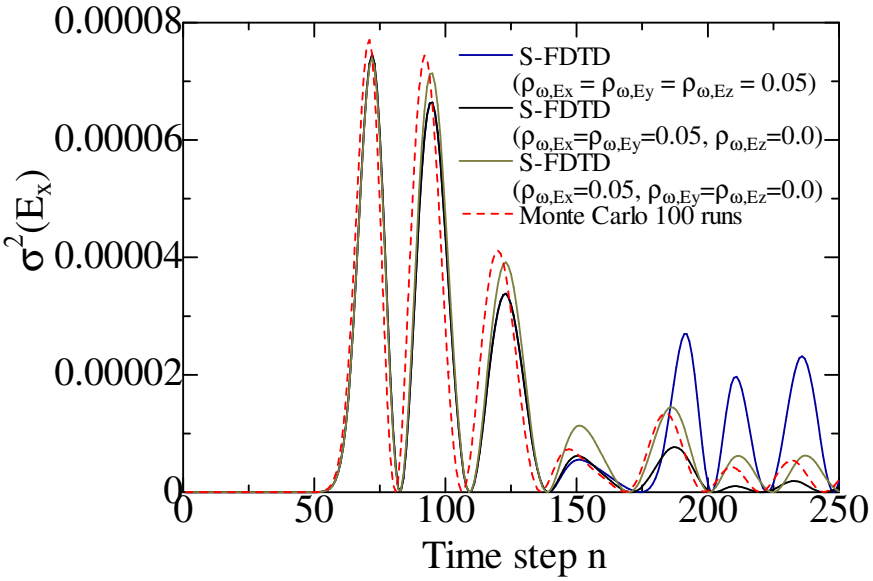

Figure 5.6: Variance of E_x with changing ρ_{ω,E_y} and ρ_{ω,E_z} (observed at a point 10 cells away from the source).

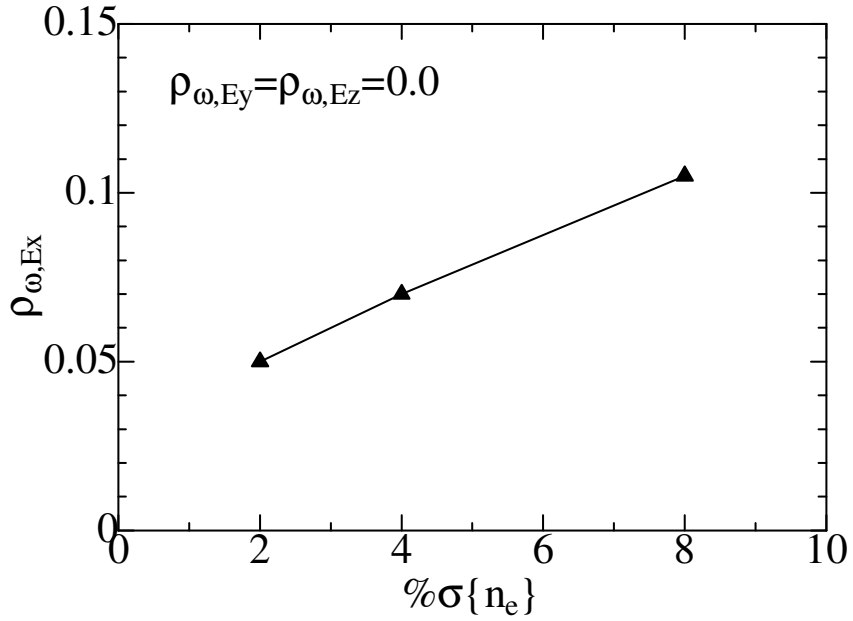

Figure 5.7: Correlation coefficient ρ_{ω,E_x} with changing standard deviation of n_e (observed at a point 10 cells away from the source).

CHAPTER 6

GROUND-LEVEL EFFECTS OF SPACE WEATHER EVENTS

6.1 Introduction

Solar coronal holes and coronal mass ejections can disturb the Earth's geomagnetic field. These geomagnetic disturbances (GMD) in turn induce electric fields which drive low frequency currents in the conductor systems operated on the surface of Earth such as power transmission networks, pipelines, telecommunication cables and railways. These low frequency currents, known as geomagnetically induced currents (GICs), may result in the saturation of the transformers in a power system, the enhanced corrosion of pipelines, and the mis-operation of communication systems etc.

The physical principle of the flow of GICs in a conductor system is fairly well understood and can be easily explained based on Faraday's law of induction: a varying magnetic field induces currents in conductors. In particular, geomagnetic disturbances result in the fluctuation of magnetospheric and ionospheric currents. These currents generate a secondary magnetic field. Faraday's law implies an electric field at the Earth's surface is induced in association with time variations of the magnetic field. This electric field then drives currents to flow in all technological networks (conductors).

Solar activity is cyclical, and reaches a maximum every $\sim$ 11 years. Some of the past extreme events, such as the Carrington event in 1859, the great geomagnetic storm of May 1921, and the Hydro-Quebec event in 1989 (which caused a massive regional power blackout within 9 h), although rare, are likely to happen again sometime in the future. Today, the occurrence of such an extreme event would cause as high as billions/trillion dollars of damage to satellites, power grids and radio communications, and could cause electrical blackouts on a massive scale. Therefore, there is an urgent need to develop methodologies that enable us to predict the occurrences of the GICs in real time in order

to mitigate harmful effects.

It is customary to divide a theoretical calculation of GICs in a technological network into two parts [107]:

- Determination of the induced geoelectric field $\{E_\phi, E_\theta\}$ at the Earth's surface, which drives the GICs in conductor systems when there are closed-loop paths typically formed by the lines, grounded transformers and the Earth (called geophysical part).
- Calculation of GICs in a particular technological network (called engineering part).

The second part is rather straightforward based on electric circuit theory such as Ohm's law, Kirchoff's law, and Thevenin's theorem for a given network. Accurate GICs can be easily obtained once the exact information on the geoelectric field and the conductor system characteristics (such as system topology, geospatial orientation, conductor type, line and winding resistances, etc.) are available. Therefore, many efforts have focused on the geophysical part. The knowledge of the geoelectric field strongly affects the accuracy of the resulting GICs. This part does not depend on any conductor systems. This chapter is also focused on the geophysical part and reports the application of the global latitude-longitude FDTD model presented in Section 3.2.1 to modeling ground-level electric fields during space weather events.

6.2 Limitations of the existing methods

The determination of the geoelectric field mainly depends on two factors:

- Magnetospheric and ionospheric currents which vary as functions of time and space.
- The Earth's conductivity which varies as a function of space. The frequency range of GICs is near-DC (less than 1 Hz), thus it can deeply penetrate inside the Earth's core.

Traditional methods of calculating the surface geoelectric field require the numerical computation that involves complicated integrals, demands long computing times, and are unsuitable for real-time prediction applications [108]. An improvement of the geophysical part has been introduced, and it is called Complex Image Method (CIM) [109], [110]. This method replaces the induced currents in the Earth by an image of the magnetospheric-

ionospheric source, and the complicated integrals are avoided when calculating the geoelectric field.

However, the accuracy of CIM is limited due to the restriction on one-dimensional (1-D) layered Earth models. Note that lateral variations in the Earth's conductivity structure affect the electric field in two ways, not only in vertical direction but also in horizontal direction. If one considers that, in each zone of the Earth's structure, the conductivity is horizontally constant, then different layers with different conductivity values within each zone will give different geoelectric field values. However, a second effect occurs at the boundary between zones where the conductivity contrast produces changes of the electric field. This is particularly true at the coast where conductivity contrast between the ocean and the continent is large. Therefore, in such cases, the geoelectric field enhancement can not be neglected. Gilbert has also recently highlighted the relevance of the "coast effect" for GICs, where the onshore electric field magnitude is enhanced considerably because of the large mismatch in the conductivities of the ocean and land [111].

6.3 Global FDTD method

A more accurate and sophisticated technique involving 2-D or 3-D modeling is necessary to investigate geomagnetic induction for realistic situations that include horizontal variations in conductivity. This is particularly important for calculations of the response of electric power systems, which often include electrical generating plants located near the seashore for cooling purposes, as well as for sea floor fiber optic telecommunications systems. Hence, the global FDTD model presented in Section 3.2.1 may be an ideal alternative for more complicated geomagnetic induction problems. As a grid-based method it may include 3-D spatial conductivity variations of the Earth's structure. Also, as a time-domain method it may model arbitrary time-varying source waveforms. It has been also demonstrated to be a robust and accurate numerical method for electromagnetic wave problems in Earth-ionosphere system. Therefore, this FDTD model can potentially provides better solutions for the surface-level geoelectromagnetic fields.

6.4 Model inputs

As discussed in the previous Section, the calculation of the geoelectric field depend on the information on ionospheric currents (equivalent to ionosphere electric fields), and the Earth's conductivity structure. These information can be applied to the global FDTD model to complete the model. A resolution of $160 \times 160 \times 5$ km at the equator is chosen for the FDTD grid where the radial direction extends from -400 km (below) to $+110$ km (above) sea level. First, this Section briefly describes the ionosphere electric fields obtained by Assimilative Mapping of Ionospheric Electrodynamics (AMIE) procedure at the height of 110 km above the Earth. This will be implemented into the top boundary of FDTD grid and acts as electric fields hard source exciting the EM wave propagation down to the Earth. Second, a 3-D Earth's conductivity model that was refined from various models will be introduced.

6.4.1 AMIE ionosphere electric field source

This Section briefly describes the Assimilative Mapping of Ionospheric Electrodynamics (AMIE) procedure and discusses potential uses of the procedure in support of GICs related studies. A full treatment of the AMIE technique is given by Richmond and Kamide [112] with an update provided by Richmond [113]. The AMIE procedure estimates distributions of electric fields E and other electrodynamic quantities (such as electrostatic potential Φ, height integrated horizontal ionospheric electric current density I, field-aligned current density $J_{||}$, and the magnetic perturbations ΔB) over the high latitude regions by the synthesis of multiple types of space-based and ground-based observations, and therefore, creating a coherent interhemispheric picture of global ionospheric electrodynamics. There are several motivations to obtain accurate patterns of ionospheric electric fields and currents. These patterns are a direct result of solar wind/magnetosphere/ionosphere interactions, and reflect the flow of plasma and electric current throughout of the magnetosphere.

Figure 6.1 schematically indicates the approach to the problem of determining a set of coefficients, which, when multiplied by a series basis functions in latitude θ and longitude ϕ, can mathematically describe a wide variety of the electrodynamic features present at any given time in the high latitude ionosphere. The AMIE procedure is essentially a con-

strained least-squares fit of the coefficients a_i to the data, with the constraints determined from a priori statistical knowledge about expected means and variances of the coefficients. The sets of coefficients in use at any given time are derived from a priori information and observations via a linear inversion. The various data sets and a priori information are assumed physically consistent. Inherent to this approach is the capability to incorporate several diverse types of observations into the inversion scheme while deriving only one set of coefficients for the basis functions which describe all of the electrodynamic patterns. AMIE can provide the type of information needed by global simulation models of ionospheric dynamic. It may also be possible to use AMIE electric field results to help define boundary conditions / sources for GICs-related FDTD simulation models.

6.4.2 Earth's conductivity

The conductivity model for entire FDTD grid consist of the ionosphere conductivity and the Earth's conductivity as shown in Figure 6.2. For the ionosphere, the exponential conductivity profile of [54] is used. A complete analysis of electric field induction would require a detailed 3-D Earth's conductivity model. A reliable 3-D conductivity Earth's model is inevitably required to quantify accurate GICs at global and regional scales. A global 3-D conductivity model of the Earth with a primary goal to be used for realistic simulation of GICs was compiled in [114]. This model will be utilized in the FDTD model in this chapter.

The compiled 3-D model represents the structures in depth range of $0 - 100$ km, including seawater, sediments, Earth crust, and partly lithosphere/asthenosphere. Global maps of bathymetry, sediment thickness, upper and lower crust thicknesses as well as lithosphere thickness are utilized to compile the model. Once the geometry of different structures is specified, each element of the structure is assigned either a certain conductivity value or conductivity versus depth distribution, according to available laboratory data and conversion laws. The model was further refined by incorporation of regional 3-D conductivity distributions inferred from the real EM data. Four 3-D regional conductivity models that are available from recent publications, namely, surface conductance model of Russia, and conductivity models of Fennoscandia, Australia and the Southwest of the United States were included into the model. All data are interpolated to form

$256 \times 128 \times 102$ cells of the FDTD grid. More explicitly, the model consists of four spherical layers as shown in Figures 6.3−6.6. In the FDTD grid, the last conductivity layer is extended until depth of 400 km due to the lack of available data at depth of $100 - 400$ km.

6.5 Calculation of the geoelectric field

The Halloween solar storm on October 30, 2003 was chosen for this study. This storm was notable because of the very high rates of change observed in the geomagnetic field. Transformer heating (gas production) and voltage fluctuations were observed in Scotland [115] and a GIC-related power outage in Malmo, Sweden, occurred at approximately 20:07 UTC and lasted for about 40 min [116].

Once the Earth-ionosphere conductivity and the AMIE electric field source are incorporated into the global FDTD model, we can readily calculate the electric field at any location on Earth's surface with respect to the source using the update equations (3.1)-(3.12) described in the Section 3.2.1. We can also determine how that electric field source interacts with the conductivity of the Earth. First, Figures 6.7, 6.8, and 6.9 show E_ϕ, E_θ and the magnitude of the horizontal E-field of the AMIE source located at the height 110 km, respectively. Next, in order to investigate the influence of the Earth's conductivity layers, snapshots of the global pattern of those fields at the Earth's surface are shown in Figures 6.10, 6.11, and 6.12. All snapshots are taken at 20:00 UTC on October 30, 2003, this is around the time the storm reach to the peak magnetic phase.

The amplitude of electric field at the Earth's surface depends on the Earth-ionosphere conductivity and the distribution of the source of electric field at the height of 110 km. The snapshots clearly indicate the influence of the Earth's conductivity layers, especially the first layer, as we can see that both E_ϕ and E_θ fields are significantly decreased in sea regions where the conductivity is the highest. Furthermore, in the continental region, relatively large amplitudes of the horizontal electric field are observed at Nordic countries and some regions of North America where known for relatively small conductivity areas compared with other regions.

Figures 6.13 and 6.14 indicate the penetration of the electric fields throughout the ionosphere and the Earth's interior. The field amplitudes, first slowly decrease down to the Earth's surface, then significantly decrease when they started to propagate into the Earth's

interior. The reason is that the Earth's conductivity, especially in the sea regions, is much larger than the ionosphere conductivity. These figures also show that the electric fields can penetrate up to more than 400 km inland depending on the site and the local conductivity structure. This observation suggests that a larger grid size should be considered to improve the results. The geoelectric field variations with periods of concern for GICs (1s to 24h) have skin depths that extend down into the core at the longest periods. Therefore, the conductivity structure down to these depths, in the future, has to be taken into account in calculating the geoelectric fields that drive GICs.

Figures 6.15-6.20 show the modeled time series of both horizontal components of *E*-field at three different observation locations as shown in Figure 6.10. The observation locations were selected for being at a similar high magnetic latitude, and since the Nordic countries and North America have been most often affected by GICs, most research has also been carried out in these countries. These figures show that the variations of the fields at the Earth's surface are similar to those at the height of 110 km, but amplitudes appear to be significantly lower. Data are shown at 5 min resolution. We can observe the first large variations in the electric fields at early time of the day, then the variations started to decline to quiet period from 04:00 UTC until 16:00 UTC, and the disturbance continues again for the remaining time of the day.

6.6 Summary

The study presented in this chapter represents the first computational solution of the full-vector Maxwell's equations for ground-level electric fields related to geomagnetic disturbances that can generate extreme geomagnetically induced currents (GICs). The model can take into account ionosphere disturbance characteristics and 3-D Earth's conductivity to calculate time-varying geoelectric fields at the entire Earth's surface.

This chapter suggests several opportunities for future research. The model presented here enables the accommodation of all of the physics of the phenomena, but there are some inherent limitations. First, it is still not able to provide any evidence for the electric field enhancement at the locations nearby ocean-continent boundaries. The main reason is that a relatively large horizontal resolution of 160×160 km was chosen for this model due to the limitation in computational resources and the lack of detail information on the

Earth's conductivity, while some studies shown that the electric field enhancement usually appears at locations less than 100 km away from coastline. A higher resolution model is necessary to study this problem.

Second, the time increment for the model is currently required to be at the micro-second order due to the bound of Courant stability condition, which led to extremely expensive computation, as a billions of time steps are needed to cover the period time (often hours/days) of GICs problem. In order to make the model feasible to apply to GICs related problem, it is important to further improve the computational efficiency for the model.

Third, a precise estimate of the ionosphere currents / electric fields and 3-D Earth conductivity in the region of interest is crucial in order to obtain a trustworthy estimate of the actual electric field. However, because of the lack of information or limitations in modeling techniques, the Earth conductivity is still poorly resolved on a global scale. It should be emphasized in this context that the numerical solution discussed in this chapter is fully 3-D and thus can readily adopt models once more reliable information is available. The influences of the conductivity distribution at greater depths and the precise stratification within the lithosphere on the results will be further investigated in the future. To this end, the stochastic FDTD model presented in Section 3.2.2 can be applied to better assess the effect of uncertainty in the Earth conductivity to the geoelectric fields.

Finally, recorded magnetic observatory data at the Earth's surface from INTERMAGNET (http://www.intermagnet.org/index-eng.php) can be directly used as an alternative data source to execute the model to calculate the geoelectric fields. Due to the lack of sufficient magnetometer installations, a suitable interpolation scheme is needed to provide full information about the spatial variation of the geomagnetic field fluctuations. Once a reliable model is established, it can provide principle information to be incorporated into GICs modeling to calculate the GICs in conductor systems across the Earth's surface.

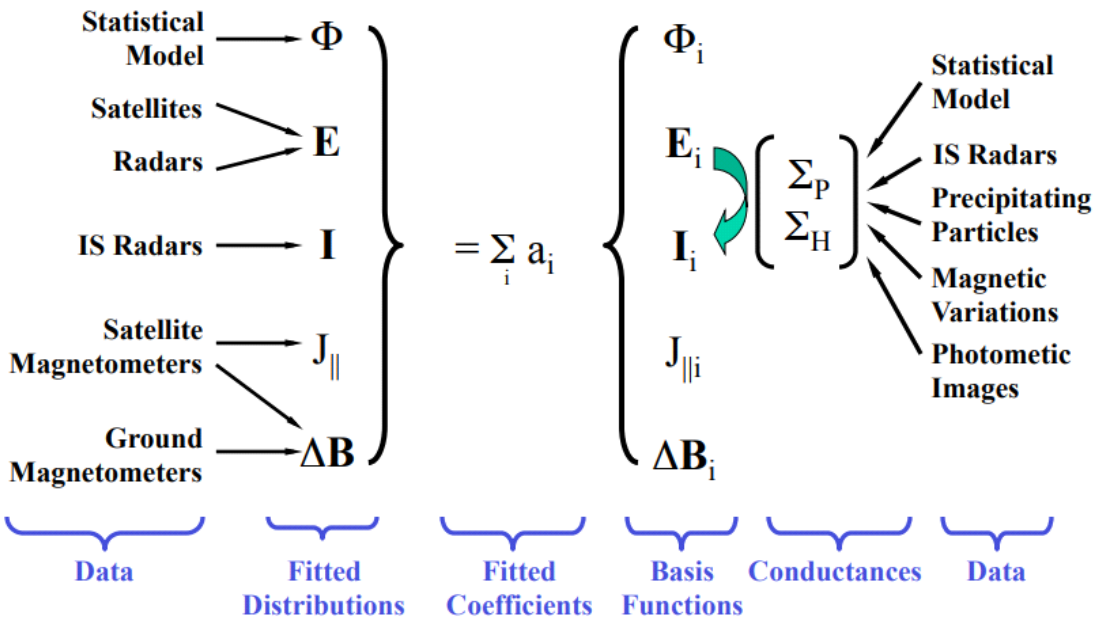

Figure 6.1: The AMIE procedure (figure courtesy of [112]).

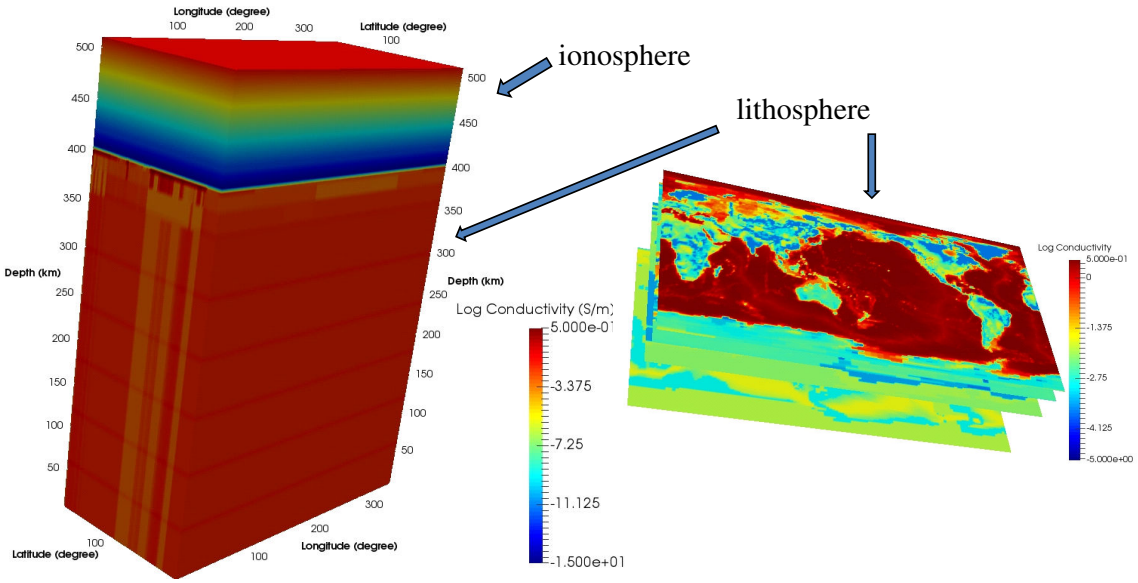

Figure 6.2: Earth-ionosphere conductivity model.

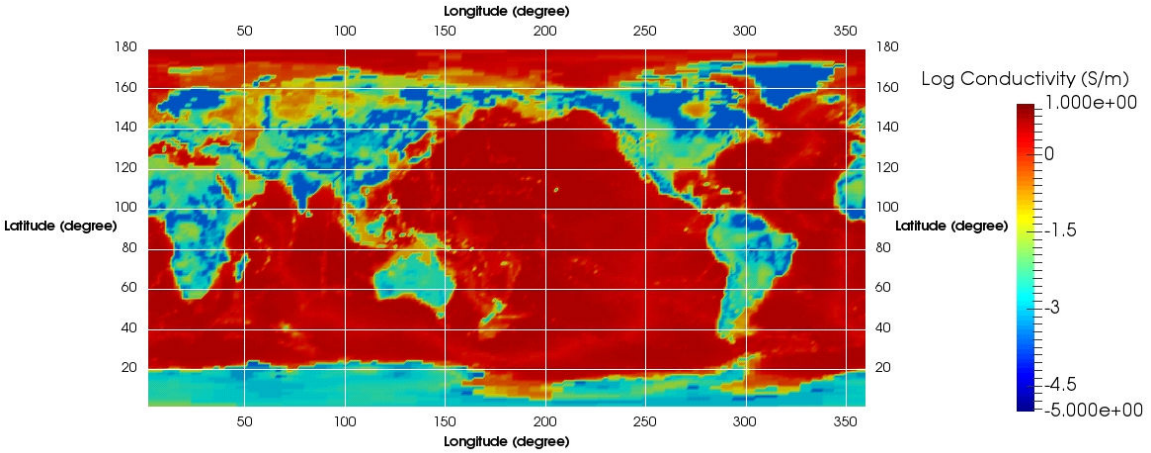

Figure 6.3: Global conductivity at the depth 0-5km.

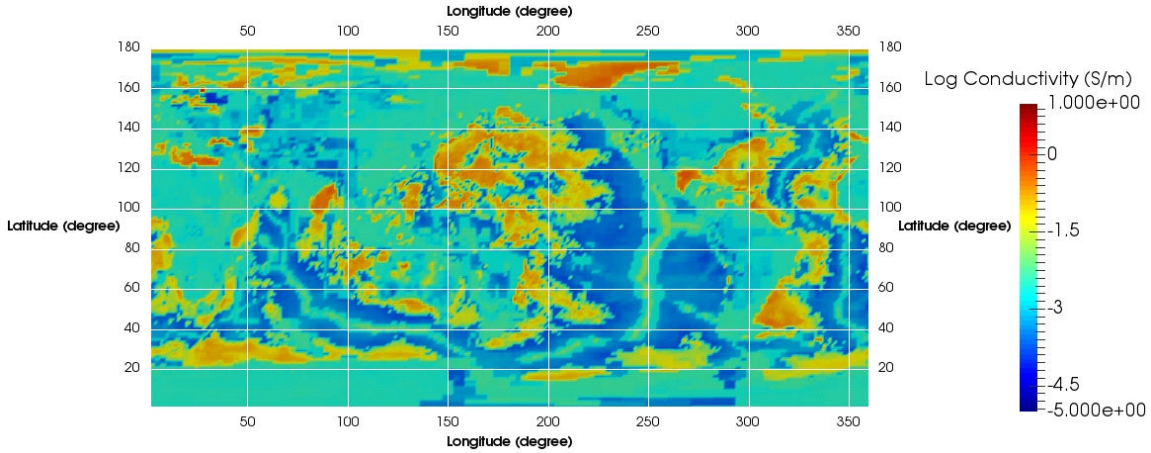

Figure 6.4: Global conductivity at the depth 5-20km.

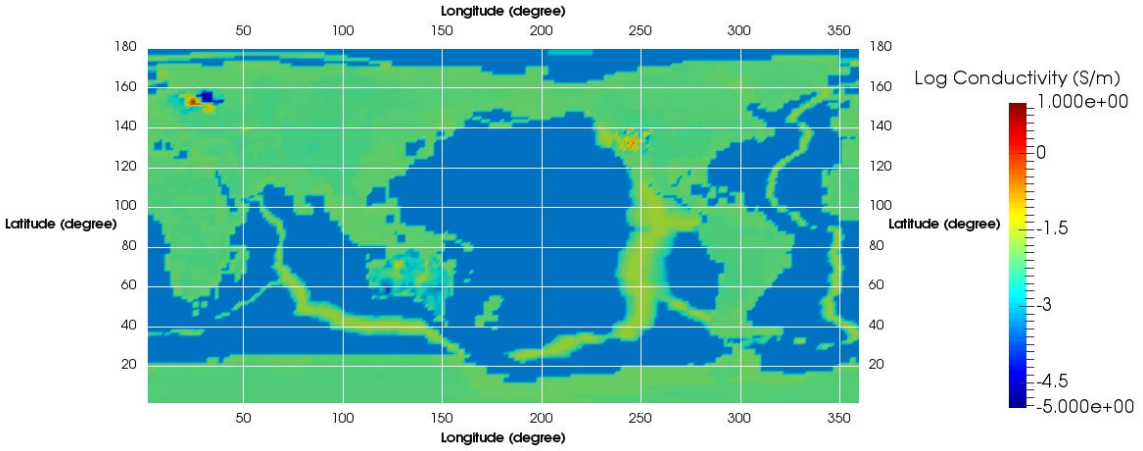

Figure 6.5: Global conductivity at the depth 20-45km.

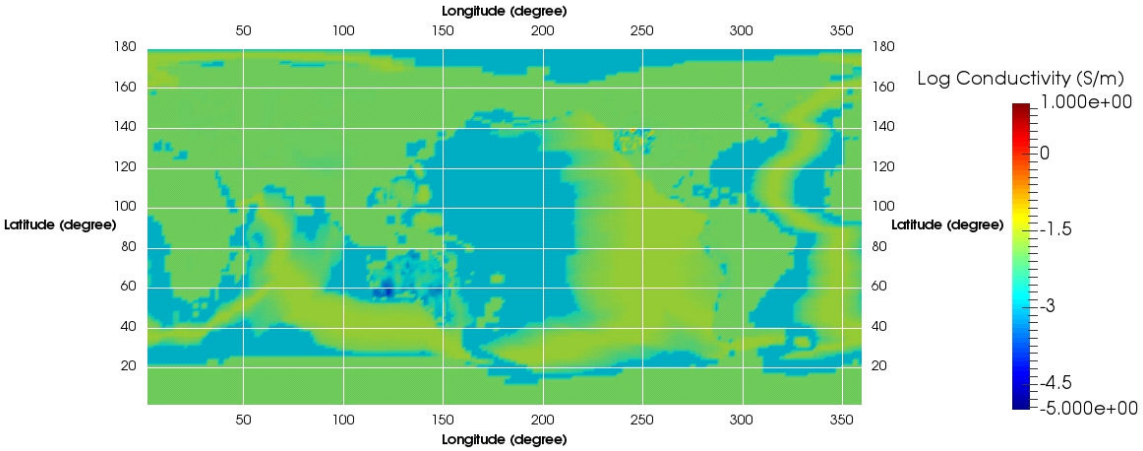

Figure 6.6: Global conductivity at the depth 45-400km.

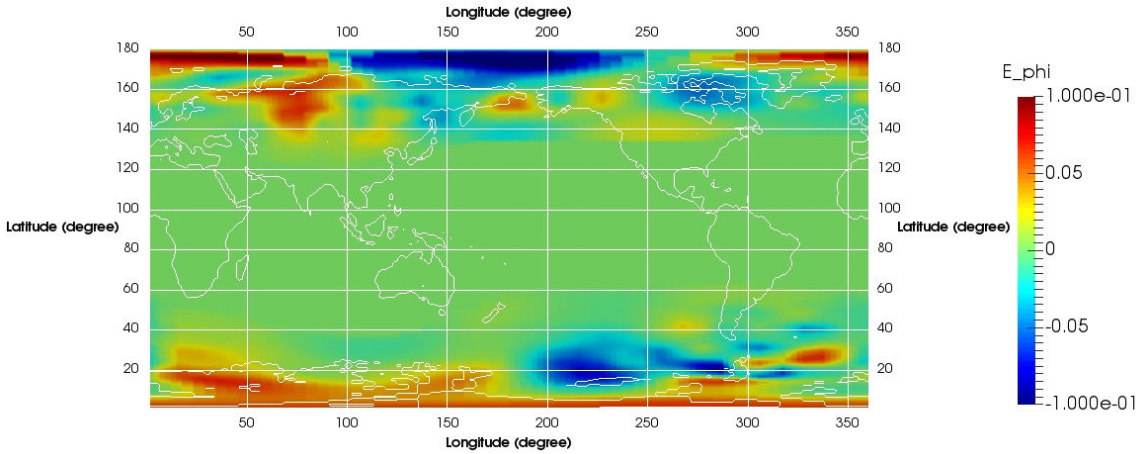

Figure 6.7: Snapshot of the E_ϕ at 110 km at 20:00 UTC on October 30, 2003.

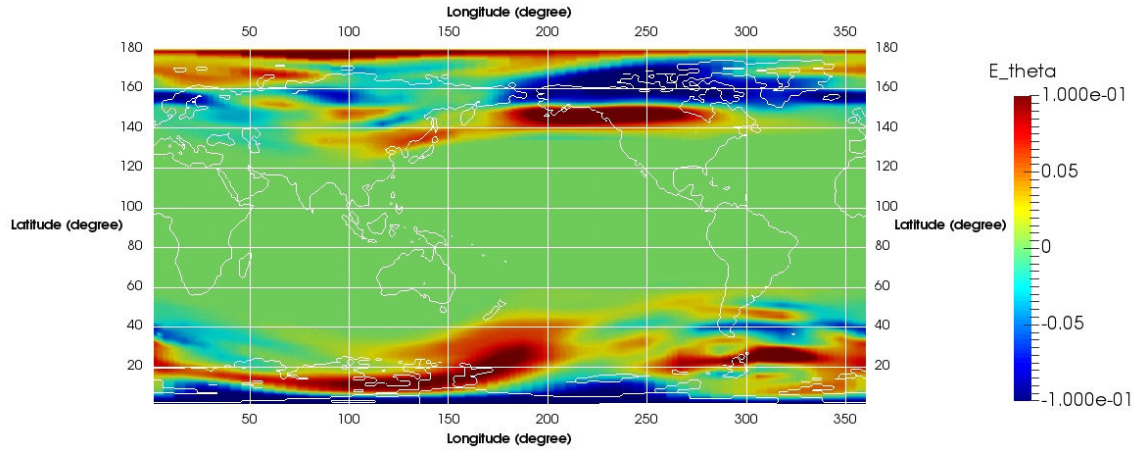

Figure 6.8: Snapshot of the E_θ at 110 km at 20:00 UTC on October 30, 2003.

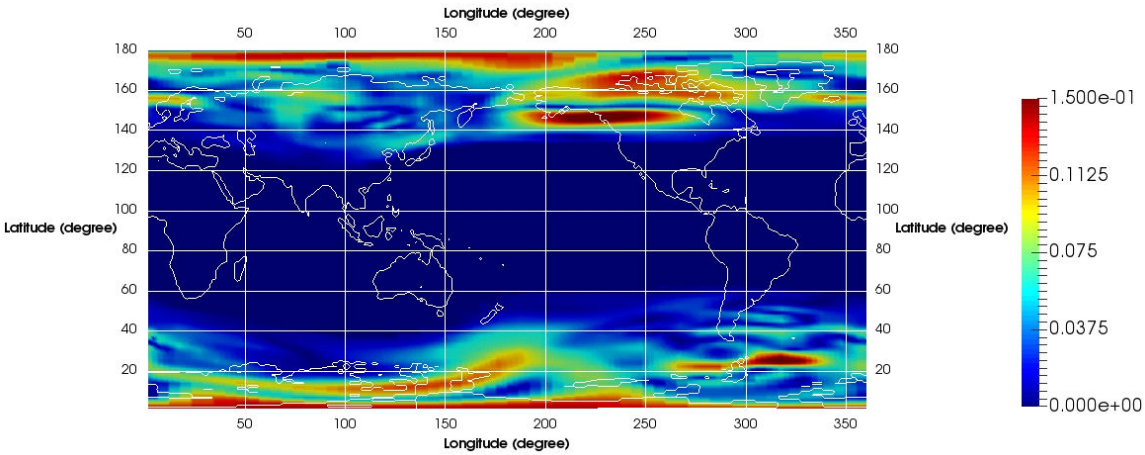

Figure 6.9: Snapshot of magnitude of the horizontal E field at 110 km at 20:00 UTC on October 30, 2003.

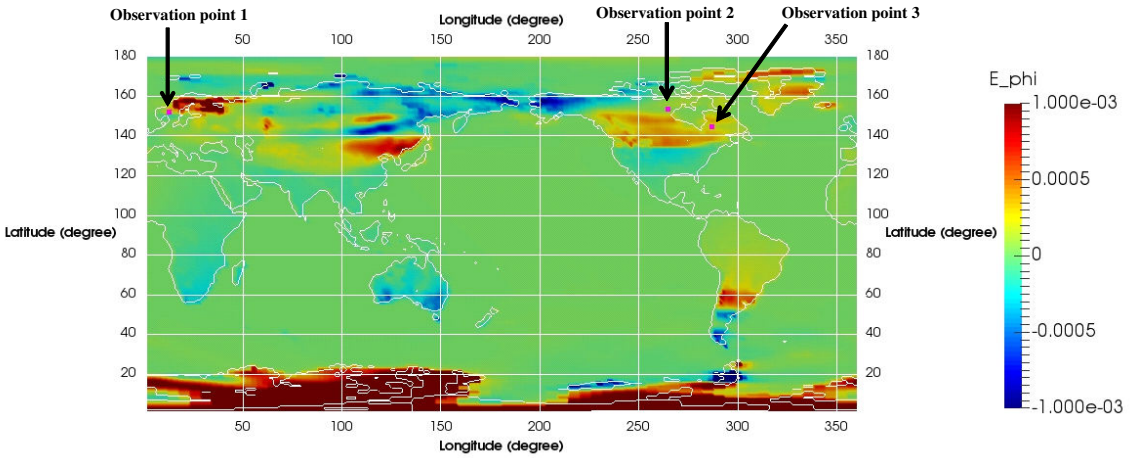

Figure 6.10: Snapshot of the E_ϕ at Earth's surface at 20:00 UTC on October 30, 2003.

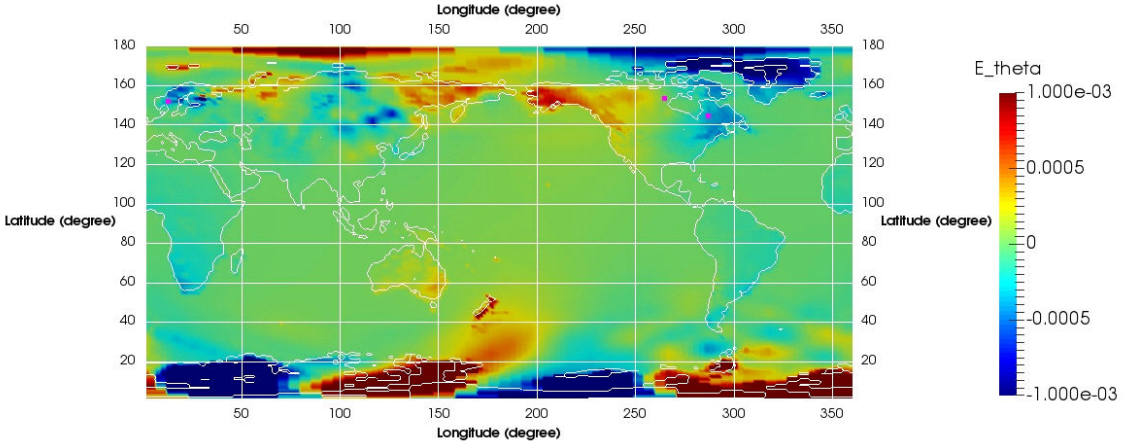

Figure 6.11: Snapshot of the E_θ at Earth's surface at 20:00 UTC on October 30, 2003.

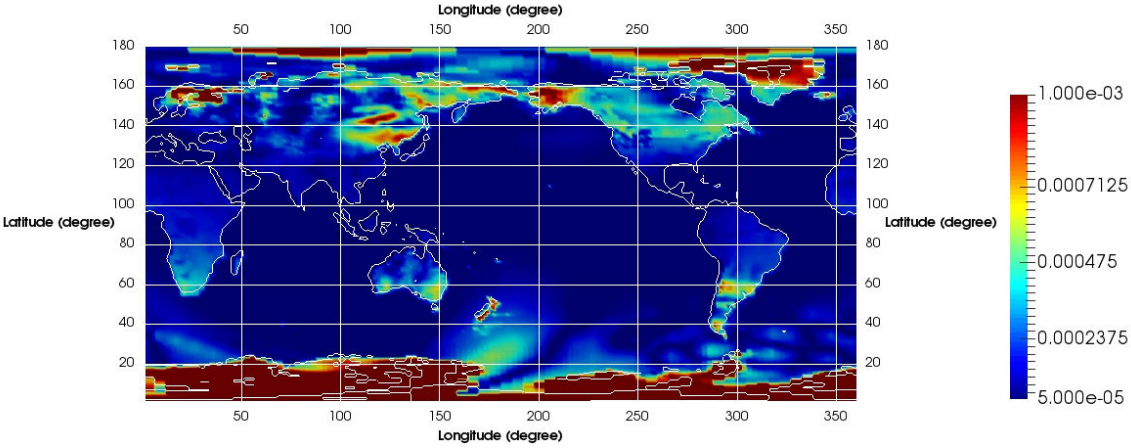

Figure 6.12: Snapshot of magnitude of the horizontal E field at Earth's surface at 20:00 UTC on October 30, 2003.

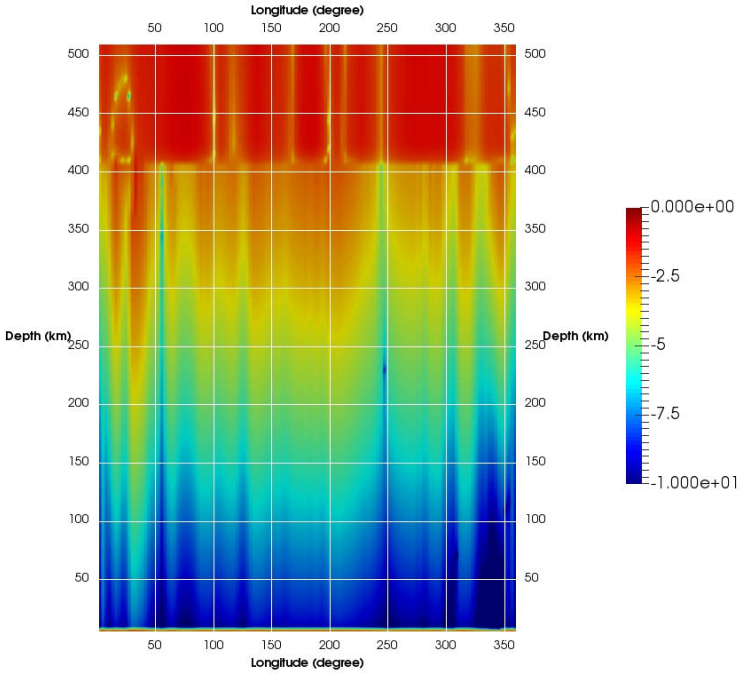

Figure 6.13: Vertical snapshot of the E_ϕ at 155^0 latitude at 20:00 UTC on October 30, 2003.

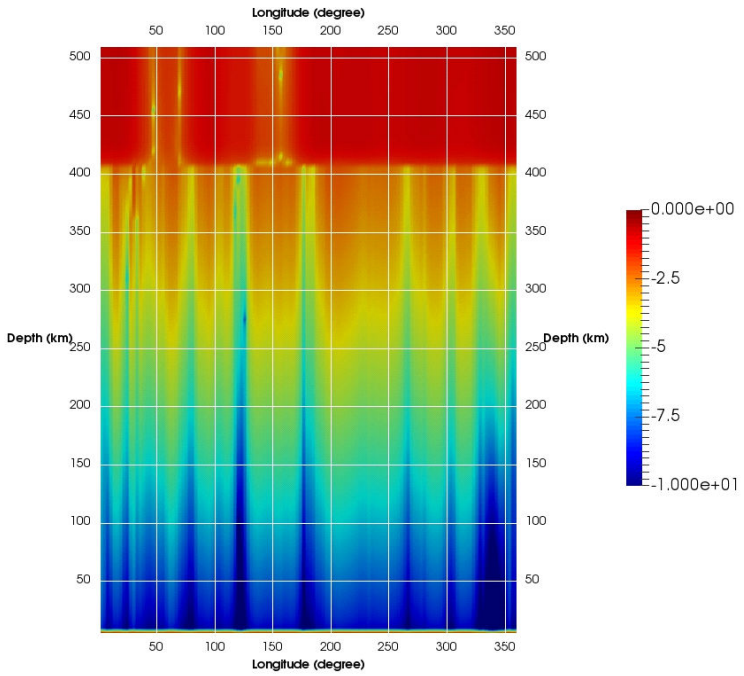

Figure 6.14: Vertical snapshot of the E_θ at 155^0 latitude at 20:00 UTC on October 30, 2003.

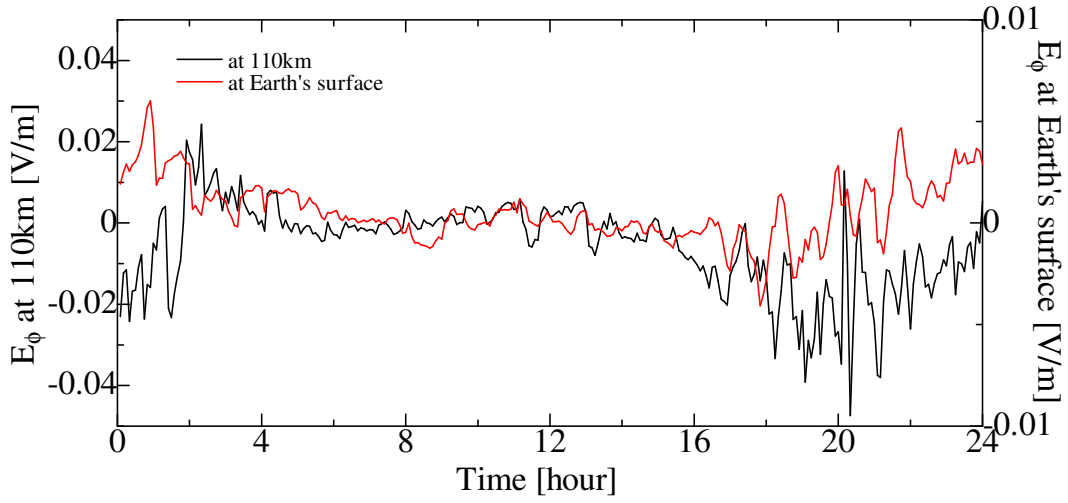

Figure 6.15: E_ϕ at 264^0 longitude and 154^0 latitude on October 30, 2003.

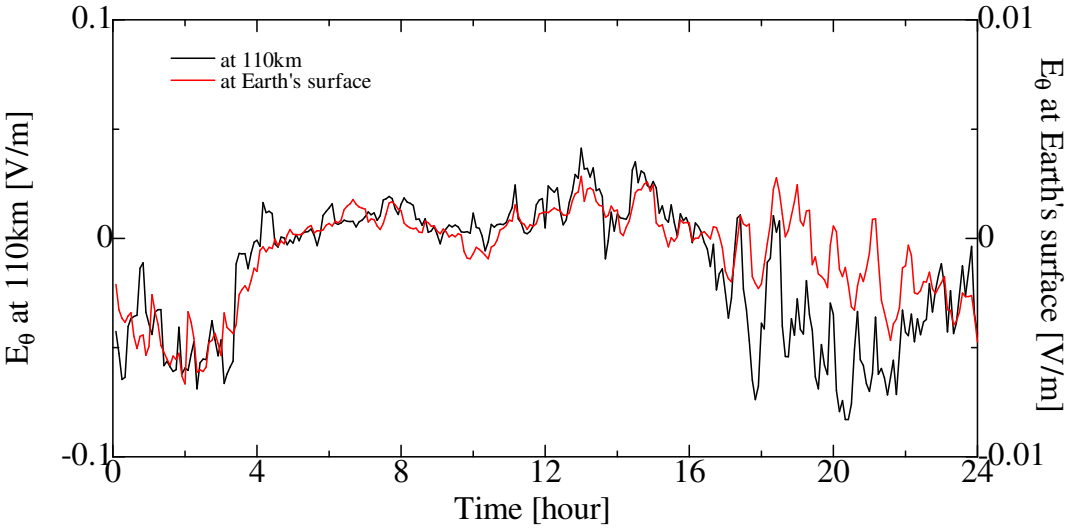

Figure 6.16: E_θ at 264^0 longitude and 154^0 latitude on October 30, 2003.

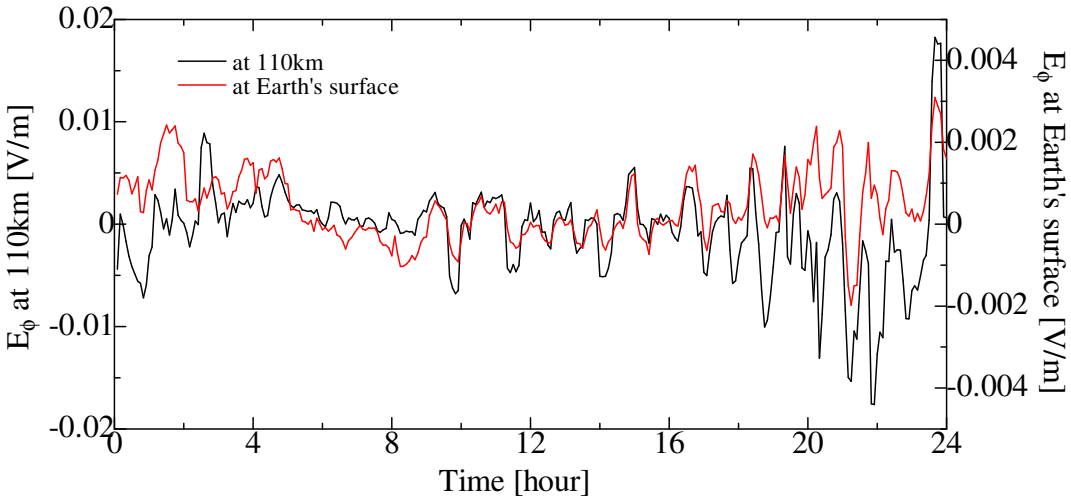

Figure 6.17: E_ϕ at 287^0 longitude and 145^0 latitude on October 30, 2003.

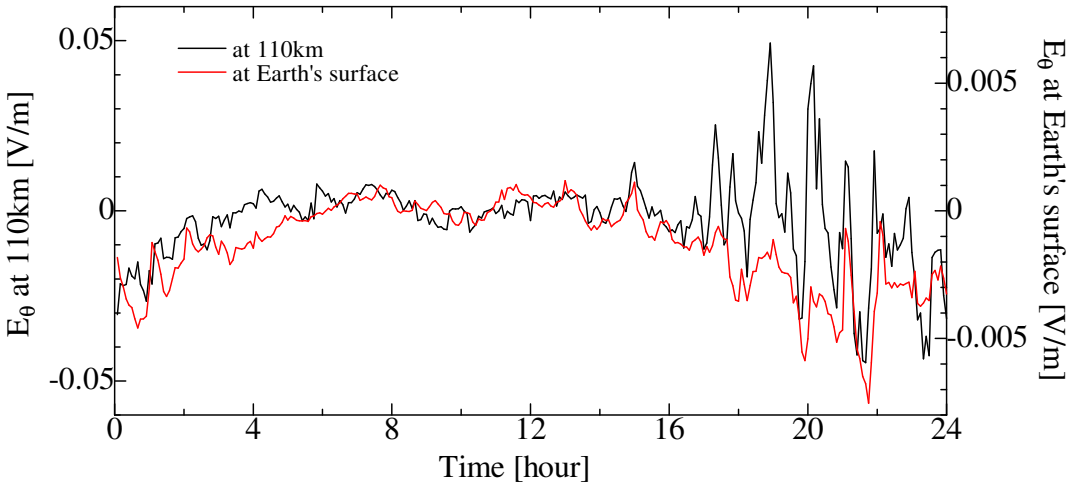

Figure 6.18: E_θ at 287^0 longitude and 145^0 latitude on October 30, 2003.

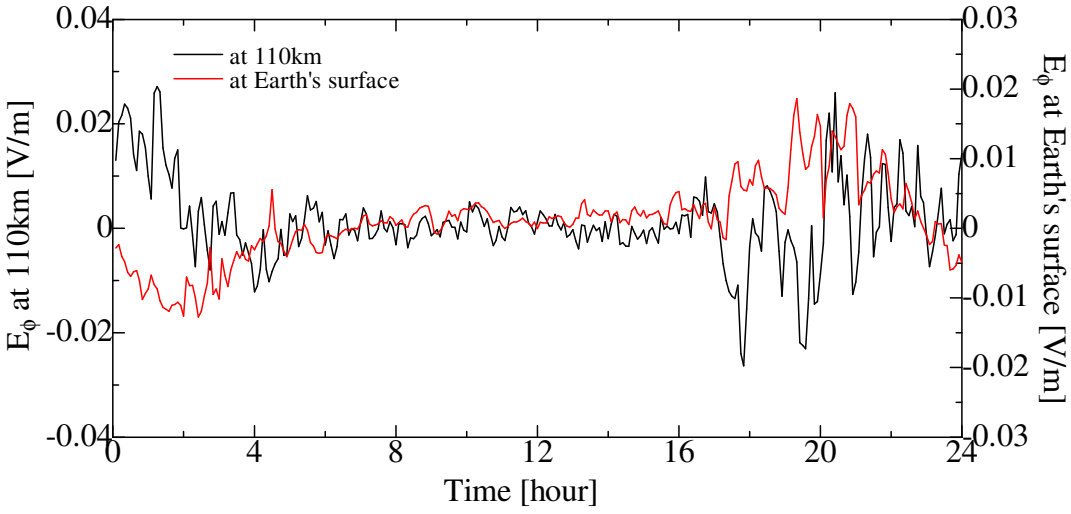

Figure 6.19: E_ϕ at 13^0 longitude and 152^0 latitude on October 30, 2003.

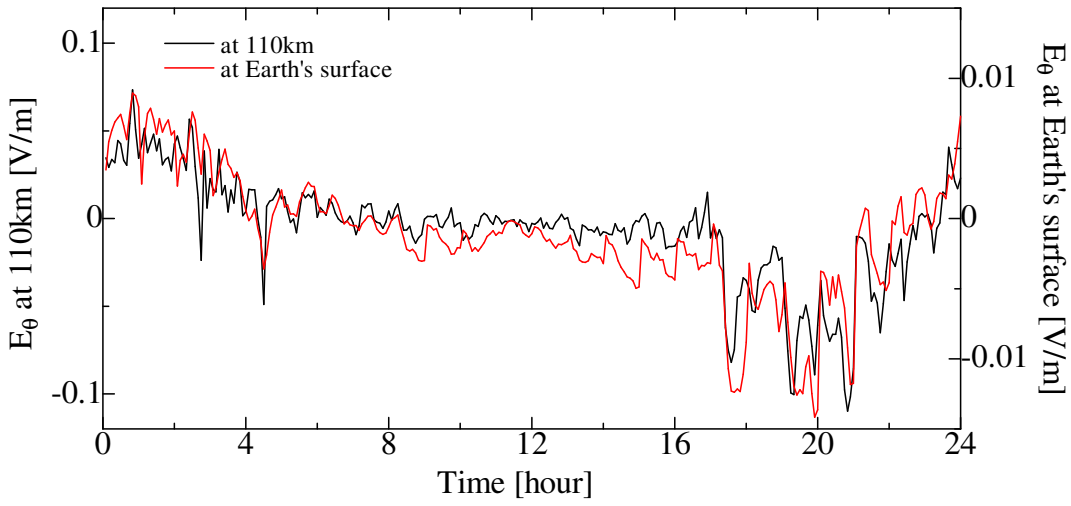

Figure 6.20: E_θ at 13^0 longitude and 152^0 latitude on October 30, 2003.

CHAPTER 7

CONCLUSIONS AND FUTURE WORK

7.1 Contributions of this dissertation

This dissertation aimed to develop the previous deterministic FDTD models of EM wave propagation in the Earth-ionosphere waveguide to efficient stochastic FDTD models wherein the ionosphere is treated as random medium. Two different stochastic methods, the polynomial chaos expansion and the delta method, were applied to the isotropic ionosphere and anisotropic ionosphere FDTD models. Excellent agreements with the results of the Monte Carlo simulations demonstrate the capability of the proposed models of treating the ionosphere complicated structure while keeping the computation cost reasonable. Furthermore, investigating effects of space whether on ground-level electric fields for the first time using the global FDTD model was another contribution of this dissertation.

The FDTD models presented in Chapters 3-5 improve our understanding of electromagnetic wave propagation through the Earth's highly variable and complex ionosphere. Specifically, these models are first time-domain stochastic solvers of EM wave propagation in Earth-ionosphere waveguide. These new algorithms efficiently calculate, via a single simulation, not only the mean EM field values, but also their variances caused by the variability or uncertainty of the ionosphere content. Following the quantification of the uncertainty in the model results, an evaluation of how much each input is contributing to the output uncertainty can be easily obtained based on global sensitivity analysis. This analysis is an aid in the validation/understanding of the model, model simplifying and factor prioritization. Furthermore, by accounting for fully, three-dimensional, global scale as well as high-resolution (even centimeter) scale and variability in the ionosphere, these new advanced algorithms represent a paradigm shift in our ability to analyze realistic, complex wave propagation in the Earth-ionosphere at broad range of frequency. These models show a significant advance over the traditional methods such as ray tracing and wave mode techniques, and this therefore will provides efficient and reliable tool for

broadband propagation.

The new stochastic FDTD models presented in this dissertation has broad potential applicability. The ability to determine not only the mean values of the ionospheric EM fields but also their variance will, for example, provide the capability of determining the confidence level that a communications / remote sensing / radar system will operate as expected under abnormal ionospheric conditions. It may also be useful in a wide variety of geophysical studies such as the work presented in Chapter 6. Taking into account that supercomputing capabilities continue to improve along with future improvement techniques on computation efficiency, these new FDTD solutions serve as a possible future standard for electrodynamics propagation modeling in Earth-ionosphere system on a global scale.

7.2 Future work

One of the major advantages of the FDTD method is its ability to spatially model complex, continuously varying, non-homogeneous media. Thus, potential research includes expanding the localized anisotropic ionosphere FDTD model discussed in Chapters 4 and 5 to a global model. This would yield the first global 3D EM propagation stochastic solver that includes a realistic, continuously-varying anisotropic model of the ionosphere subjected to the Earth's magnetic field.

Unlike the isotropic ionosphere FDTD model where a PEC boundary condition is sufficient in the radial direction of the Earth-ionosphere system, an appropriate absorbing boundary condition is usually required for the anisotropic ionosphere FDTD model that involves electromagnetic wave propagation at higher frequencies and altitudes in the ionosphere than isotropic conductivity profiles. Although an absorbing boundary condition based on the second-order approximations of Engquist and Majda's wave equations was implemented in the magnetized cold plasma algorithm in Chapter 5, it exhibits a late-time instability. A more proper absorbing boundary condition will be an important topic for future study to complete the global stochastic anisotropic ionosphere FDTD model.

Although the FDTD method has been demonstrated as an efficient and reliable method over the traditional analytical methods such as ray tracing and wave mode techniques for modeling EM wave propagation in the Earth-ionosphere waveguide, it is computationally expensive since large computation memory and time are required. The applications to

date, therefore, are limited to lower range frequencies such as ELF/VLF. These drawbacks mainly come from two modeling constraints:

- First, the spatial increment step (cell size) must be small enough in comparison with the smallest wavelength. Normally the method requires 10-20 steps per smallest wavelength to ensure that the numerical dispersion error is negligible.

- Second, the time step is limited by the minimum cell size in a computational domain to satisfy the Courant stability condition.

Many studies on time domain techniques have been developed to improve the FDTD computational efficiency. The strategies, apparently, are focused on increasing the cell size and/or the time step. To relax the first constraint, the multiresolution time domain (MRTD) method [117] can reduce the spatial discretization to two steps per wavelength by using orthonormal wavelet spatial expansions. Similarly, another technique, the pseudo-spectral time domain (PSTD) method [118] can also achieve a spatial grid of two points per wavelength by using the fast Fourier transform (FFT) to represent spatial derivatives. Both techniques maintain as high accuracy as the FDTD method. However, these methods still suffer from the stability condition due to the explicit time integration scheme. The MRTD method becomes even more stringent on the stability condition than the FDTD/PSTD methods as it requires the time-to-spatial five times less than that with the traditional FDTD. To overcome the second constraint, the alternating direct implicit (ADI) method based on implicit-type finite difference algorithm was proposed to remove the Courant stability condition [119]. The selection of the time step is now dependent only on the model accuracy of the FDTD algorithm because of the mixed ADI and the FDTD.

Some attempts but not many were made to enhance the computation efficiency for plasma applications and propagation in the Earth-ionosphere cavity applications by using the PSTD method or the ADI method (e.g., [120]–[122]). Nevertheless, they were considered for only some simplified cases. While the PSTD [120] and the ADI [121] methods were employed for modeling unmagnetized (therefore, isotropic) plasma and for the Cartesian coordinate system, the ADI [122] was developed for spherical geometries without considering the effects of ionosphere plasma (this assumption is only valid for lower frequency). The results in [122] also indicated that late time instability of the spherical ADI model occurs and prevents the full transient response.

Here, applying the PSTD and / or ADI methods for the models presented in this dissertation, although challenging, will be investigated as part of future research to explore alternatives that potentially allow a much larger cell size / time step and permit simulations to run significantly faster. The new models, if successful, provide a good means for higher frequency and long-distant propagation and applications.

APPENDIX A

COEFFICIENT MATRIXES

$$A = \begin{bmatrix} 1 & 0 & 0 & 0.5 & 0 & 0 \\ 0 & 1 & 0 & 0 & 0.5 & 0 \\ 0 & 0 & 1 & 0 & 0 & 0.5 \\ -\frac{(\omega_{Pe}\Delta t)^2}{2} & 0 & 0 & 1+\frac{v_e\Delta t}{2} & \frac{\omega_{cez}\Delta t}{2} & -\frac{\omega_{cey}\Delta t}{2} \\ 0 & -\frac{(\omega_{Pe}\Delta t)^2}{2} & 0 & -\frac{\omega_{cez}\Delta t}{2} & 1+\frac{v_e\Delta t}{2} & \frac{\omega_{cex}\Delta t}{2} \\ 0 & 0 & -\frac{(\omega_{Pe}\Delta t)^2}{2} & \frac{\omega_{cey}\Delta t}{2} & -\frac{\omega_{cex}\Delta t}{2} & 1+\frac{v_e\Delta t}{2} \end{bmatrix} \tag{A.1}$$

$$B = \begin{bmatrix} 1 & 0 & 0 & -0.5 & 0 & 0 \\ 0 & 1 & 0 & 0 & -0.5 & 0 \\ 0 & 0 & 1 & 0 & 0 & -0.5 \\ \frac{(\omega_{Pe}\Delta t)^2}{2} & 0 & 0 & 1-\frac{v_e\Delta t}{2} & -\frac{\omega_{cez}\Delta t}{2} & \frac{\omega_{cey}\Delta t}{2} \\ 0 & \frac{(\omega_{Pe}\Delta t)^2}{2} & 0 & \frac{\omega_{cez}\Delta t}{2} & 1-\frac{v_e\Delta t}{2} & -\frac{\omega_{cex}\Delta t}{2} \\ 0 & 0 & \frac{(\omega_{Pe}\Delta t)^2}{2} & -\frac{\omega_{cey}\Delta t}{2} & \frac{\omega_{cex}\Delta t}{2} & 1-\frac{v_e\Delta t}{2} \end{bmatrix} \tag{A.2}$$

$$C = \begin{bmatrix} \frac{(\Delta t)^2}{\epsilon_0\mu_0\Delta z} & -\frac{(\Delta t)^2}{\epsilon_0\mu_0\Delta y} & 0 & 0 & 0 & 0 \\ 0 & 0 & \frac{(\Delta t)^2}{\epsilon_0\mu_0\Delta x} & -\frac{(\Delta t)^2}{\epsilon_0\mu_0\Delta z} & 0 & 0 \\ 0 & 0 & 0 & 0 & \frac{(\Delta t)^2}{\epsilon_0\mu_0\Delta y} & -\frac{(\Delta t)^2}{\epsilon_0\mu_0\Delta x} \\ 0 & 0 & 0 & 0 & 0 & 0 \\ 0 & 0 & 0 & 0 & 0 & 0 \\ 0 & 0 & 0 & 0 & 0 & 0 \end{bmatrix} \tag{A.3}$$

$$D = \begin{bmatrix} 0 & 0 & 0 & 0 & 0 & 0 \\ 0 & 0 & 0 & 0 & 0 & 0 \\ 0 & 0 & 0 & 0 & 0 & 0 \\ \omega_{Pe}\Delta t^2\sigma\{\omega_{Pe}\} \times \rho_{\omega_{Pe},Ex} & 0 & 0 & \omega_{Pe}\Delta t^2\sigma\{\omega_{Pe}\} \times \rho_{\omega_{Pe},Ex} & 0 & 0 \\ 0 & \omega_{Pe}\Delta t^2\sigma\{\omega_{Pe}\} \times \rho_{\omega_{Pe},Ey} & 0 & 0 & \omega_{Pe}\Delta t^2\sigma\{\omega_{Pe}\} \times \rho_{\omega_{Pe},Ey} & 0 \\ 0 & 0 & \omega_{Pe}\Delta t^2\sigma\{\omega_{Pe}\} \times \rho_{\omega_{Pe},Ez} & 0 & 0 & \omega_{Pe}\Delta t^2\sigma\{\omega_{Pe}\} \times \rho_{\omega_{Pe},Ez} \end{bmatrix} \tag{A.4}$$

APPENDIX B

DERIVATION OF CURRENT DENSITY

The current density equation can be combined as

$$\mathbf{J}_e^+ = \mathbf{J}_e^- + [\mathbf{J}_e^- + (\mathbf{J}_e^- \times \mathbf{t})] \times \mathbf{s} \tag{B.1}$$

For collisional regime at predictor step we have

$$\mathbf{J}_e^+ = \mathbf{J}_{e,p}^{n+1/2} - \frac{\Delta t \epsilon_0 \omega_{Pe}^2 \mathbf{E}^n}{2} + \frac{\Delta t v_e \mathbf{J}_e^{n-1/2}}{2};\ \ \mathbf{J}_e^- = \mathbf{J}_e^{n-1/2} + \frac{\Delta t \epsilon_0 \omega_{Pe}^2 \mathbf{E}^n}{2} - \frac{\Delta t v_e \mathbf{J}_e^{n-1/2}}{2}$$

$$\mathbf{t} = \frac{-\boldsymbol{\omega_{Ce}}}{|\omega_{Ce}|} \tan\frac{\theta}{2};\ \ \mathbf{s} = \frac{-\boldsymbol{\omega_{Ce}}}{|\omega_{Ce}|} \sin\theta$$

Substitute the above into the equation (B.1), we obtain

$$\mathbf{J}_e^+ = \mathbf{J}_e^- + \mathbf{J}_e^- \times \mathbf{s} + (\mathbf{J}_e^- \times \mathbf{t}) \times \mathbf{s} \tag{B.2}$$

$$\begin{aligned} \mathbf{J}_{e,p}^{n+1/2} - \frac{\Delta t \epsilon_0 \omega_{Pe}^2 \mathbf{E}^n}{2} \quad + \quad & \frac{\Delta t v_e \mathbf{J}_e^{n-1/2}}{2} = \mathbf{J}_e^{n-1/2} + \frac{\Delta t \epsilon_0 \omega_{Pe}^2 \mathbf{E}^n}{2} - \frac{\Delta t v_e \mathbf{J}_e^{n-1/2}}{2} \\ & + \left(\mathbf{J}_e^{n-1/2} + \frac{\Delta t \epsilon_0 \omega_{Pe}^2 \mathbf{E}^n}{2} - \frac{\Delta t v_e \mathbf{J}_e^{n-1/2}}{2} \right) \times \mathbf{s} \\ & + \left[\left(\mathbf{J}_e^{n-1/2} + \frac{\Delta t \epsilon_0 \omega_{Pe}^2 \mathbf{E}^n}{2} - \frac{\Delta t v_e \mathbf{J}_e^{n-1/2}}{2} \right) \times \mathbf{t} \right] \times \mathbf{s} \end{aligned} \tag{B.3}$$

$$\begin{aligned} \mathbf{J}_{e,p}^{n+1/2} \quad = \quad & \mathbf{J}_e^{n-1/2} + \Delta t \epsilon_0 \omega_{Pe}^2 \mathbf{E}^n - \Delta t v_e \mathbf{J}_e^{n-1/2} \\ & + \mathbf{J}_e^{n-1/2} \times \mathbf{s} + \frac{\Delta t \epsilon_0 \omega_{Pe}^2 \mathbf{E}^n}{2} \times \mathbf{s} - \frac{\Delta t v_e \mathbf{J}_e^{n-1/2}}{2} \times \mathbf{s} \\ & + \left(\mathbf{J}_e^{n-1/2} \times \mathbf{t} \right) \times \mathbf{s} + \left(\frac{\Delta t \epsilon_0 \omega_{Pe}^2 \mathbf{E}^n}{2} \times \mathbf{t} \right) \times \mathbf{s} - \left(\frac{\Delta t v_e \mathbf{J}_e^{n-1/2}}{2} \times \mathbf{t} \right) \times \mathbf{s} \end{aligned} \tag{B.4}$$

$$\begin{aligned}\mathbf{J}_{e,p}^{n+1/2} &= \mathbf{J}_e^{n-1/2} + \Delta t\epsilon_0\omega_{Pe}^2\mathbf{E}^n - \Delta t v_e\mathbf{J}_e^{n-1/2} \\ &-\frac{\sin\theta}{|\omega_{Ce}|}\mathbf{J}_e^{n-1/2}\times\boldsymbol{\omega_{Ce}} - \frac{\Delta t\epsilon_0\sin\theta}{2|\omega_{Ce}|}\omega_{Pe}^2\mathbf{E}^n\times\boldsymbol{\omega_{Ce}} + \frac{\Delta t\sin\theta}{2|\omega_{Ce}|}v_e\mathbf{J}_e^{n-1/2}\times\boldsymbol{\omega_{Ce}} \\ &+\frac{\tan\frac{\theta}{2}\sin\theta}{|\omega_{Ce}|^2}\left(\mathbf{J}_e^{n-1/2}\times\boldsymbol{\omega_{Ce}}\right)\times\boldsymbol{\omega_{Ce}} + \frac{\Delta t\epsilon_0\tan\frac{\theta}{2}\sin\theta}{2|\omega_{Ce}|^2}\omega_{Pe}^2\left(\mathbf{E}^n\times\boldsymbol{\omega_{Ce}}\right)\times\boldsymbol{\omega_{Ce}} \\ &-\frac{\Delta t\tan\frac{\theta}{2}\sin\theta}{2|\omega_{Ce}|^2}v_e\left(\mathbf{J}_e^{n-1/2}\times\boldsymbol{\omega_{Ce}}\right)\times\boldsymbol{\omega_{Ce}} \end{aligned} \tag{B.5}$$

where

$$\mathbf{J}_e^{n-1/2}\times\boldsymbol{\omega_{Ce}} = \left\{J_{ey}^{n-1/2}\omega_{Cez} - J_{ez}^{n-1/2}\omega_{Cey};\ J_{ez}^{n-1/2}\omega_{Cex} - J_{ex}^{n-1/2}\omega_{Cez};\ J_{ex}^{n-1/2}\omega_{Cey} - J_{ey}^{n-1/2}\omega_{Cex}\right\}$$

$$\mathbf{E}^n\times\boldsymbol{\omega_{Ce}} = \left\{E_y^n\omega_{Cez} - E_z^n\omega_{Cey};\ E_z^n\omega_{Cex} - E_x^n\omega_{Cez};\ E_x^n\omega_{Cey} - E_y^n\omega_{Cex}\right\}$$

$$\begin{aligned}\left(\mathbf{J}_e^{n-1/2}\times\boldsymbol{\omega_{Ce}}\right)\times\boldsymbol{\omega_{Ce}} &= \left\{\left(J_{ez}^{n-1/2}\omega_{Cex} - J_{ex}^{n-1/2}\omega_{Cez}\right)\omega_{Cez} - \left(J_{ex}^{n-1/2}\omega_{Cey} - J_{ey}^{n-1/2}\omega_{Cex}\right)\omega_{Cey};\right. \\ &\left(J_{ex}^{n-1/2}\omega_{Cey} - J_{ey}^{n-1/2}\omega_{Cex}\right)\omega_{Cex} - \left(J_{ey}^{n-1/2}\omega_{Cez} - J_{ez}^{n-1/2}\omega_{Cey}\right)\omega_{Cez}; \\ &\left.\left(J_{ey}^{n-1/2}\omega_{Cez} - J_{ez}^{n-1/2}\omega_{Cey}\right)\omega_{Cey} - \left(J_{ez}^{n-1/2}\omega_{Cex} - J_{ex}^{n-1/2}\omega_{Cez}\right)\omega_{Cex}\right\}\end{aligned}$$

$$\begin{aligned}\left(\mathbf{E}^n\times\boldsymbol{\omega_{Ce}}\right)\times\boldsymbol{\omega_{Ce}} = \left\{\left(E_z^n\omega_{Cex} - E_x^n\omega_{Cez}\right)\omega_{Cez} - \left(E_x^n\omega_{Cey} - E_y^n\omega_{Cex}\right)\omega_{Cey};\right. \\ \left(E_x^n\omega_{Cey} - E_y^n\omega_{Cex}\right)\omega_{Cex} - \left(E_y^n\omega_{Cez} - E_z^n\omega_{Cey}\right)\omega_{Cez}; \\ \left.\left(E_y^n\omega_{Cez} - E_z^n\omega_{Cey}\right)\omega_{Cey} - \left(E_z^n\omega_{Cex} - E_x^n\omega_{Cez}\right)\omega_{Cex}\right\}\end{aligned}$$

REFERENCES

[1] K. Yee, "A numerical solution of initial boundary value problems involving Maxwell's equations in isotropic media," *IEEE Trans. Antennas Propag.*, vol. 14, pp. 302–307, 1966.

[2] A. Taflove and S. C. Hagness, *Computational Electromagnetics: Finite-Difference Time-Domain Method*, 3rd ed. Norwood, MA, USA: Artech House, 2005.

[3] J. P. Berenger, "Finite-difference computation of VLF-LF propagation in the Earth-ionosphere waveguide," in *EUROEM Symp.*, Bordeaux, France, 1994.

[4] S. A. Cummer, "An analysis of new and existing FDTD methods for isotropic cold plasma and a method for improving their accuracy," *IEEE Trans. Antennas Propag.*, vol. 45, no. 3, pp. 392–400, Mar. 1997.

[5] J. H. Lee and D. K. Kalluri, "Three-dimensional FDTD simulation of electromagnetic wave transformation in a dynamic inhomogeneous magnetized plasma," *IEEE Trans. Antennas Propag.*, vol. 47, no. 7, pp. 1146–1151, 1999.

[6] M. Thèvenot, J. P. Bérenger, T. Monedière, and F. Jecko, "A FDTD scheme for the computation of VLF-LF propagation in the anisotropic earth-ionosphere waveguide," *Ann. Telecommun.*, vol. 54, pp. 297–310, 1999.

[7] S. A. Cummer, "Modeling electromagnetic propagation in the earth-ionosphere waveguide," *IEEE Trans. Antennas Propag.*, vol. 48, pp. 1420–1429, 2000.

[8] T. Otsuyama and M. Hayakawa, "FDTD simulation and experimental result on VLF scattering by ionospheric perturbation in earth-ionosphere waveguide," *Trans. Inst. Elect. Eng. Jpn. A*, vol. 122-A, no. 1, pp. 59–63, 2002.

[9] J. J. Simpson and A. Taflove, "Three-dimensional FDTD modeling of impulsive ELF antipodal propagation and Schumann resonance of the earth-sphere," *IEEE Trans. Antennas Propag.*, vol. 52, no. 2, pp. 443–451, Feb. 2004.

[10] H. Yang and V. P. Pasko, "Three-dimensional finite difference time domain modeling of the diurnal and seasonal variations in Schumann resonance parameters," *Radio Sci.*, vol. 41, p. RS2S14, 2006.

[11] W. Hu and S. A. Cummer, "An FDTD model for low and high altitude lightning-generated EM fields," *IEEE Trans. Antennas Propag.*, vol. 54, no. 5, pp. 1513 –1522, 2006.

[12] J. J. Simpson and A. Taflove, "A review of progress in FDTD Maxwell's equations modeling of impulsive subionospheric propagation below 300 kHz," *IEEE Trans. Antennas Propag.*, vol. 55, no. 6, pp. 1582–1590, 2007.

[13] J. J. Simpson, "Current and future applications of 3-D global Earth-ionosphere models based on the full-vector Maxwells equations FDTD method," *Surv. Geophys.*, vol. 30, no. 2, pp. 105–130, 2009.

[14] Y. Yu and J. J. Simpson, "An E-J collocated 3-D FDTD model of electromagnetic wave propagation in magnetized cold plasma," *IEEE Trans. Antennas Propag.*, vol. 58, no. 2, pp. 469–478, 2010.

[15] Y. Yu, J. Niu, and J. J. Simpson, "A 3-D global Earth-ionosphere FDTD model including an anisotropic magnetized plasma ionosphere," *IEEE Trans. Antennas Propag.*, vol. 60, no. 7, pp. 3246–3256, 2012.

[16] A. Samimi and J. J. Simpson, "An efficient 3-D FDTD model of electromagnetic wave propagation in magnetized plasma," *IEEE Trans. Antennas Propag.*, vol. 63, no. 1, pp. 269–279, Jan. 2015.

[17] M. Cho and M. J. Rycroft, "Computer simulation of the electric field structure and optical emission from cloud-top to the ionosphere," *J. Atmos. Sol. Terr. Phys.*, vol. 60, no. 7, pp. 871–888, 1998.

[18] V. P. Pasko, U. S. Inan, T. F. Bell, and S. C. Reising, "Mechanism of ELF radiation from sprites," *Geophys. Res. Lett.*, vol. 25, no. 18, pp. 3493–3496, 1998.

[19] G. Veronis, V. P. Pasko, and U. S. Inan, "Characteristics of mesospheric optical emissions produced by lightning discharges," *J. Geophys. Res.*, vol. 104, no. A6, pp. 12 645–12 656, 1999.

[20] H. Yang and V. P. Pasko, "Three-dimensional finite difference time domain modeling of the Earth-ionosphere cavity resonances," *Geophys. Res. Lett.*, vol. 32, no. 3, 2005.

[21] J. J. Simpson and A. Taflove, "A novel ELF radar for major oil deposits," *IEEE Geosci. Remote Sens. Lett.*, vol. 3, no. 1, pp. 36–39, 2006.

[22] ——, "ELF radar system proposed for localized D-region ionospheric anomalies," *IEEE Geosci. Remote Sens. Lett.*, vol. 3, no. 4, pp. 500–503, 2006.

[23] ——, "Electrokinetic effect of the Loma Prieta earthquake calculated by an entire-Earth FDTD solution of Maxwell's equations," *Geophys. Res. Lett.*, vol. 32, no. 9, 2005.

[24] A. Taflove and M. E. Brodwin, "Numerical solution of steady-state electromagnetic scattering problems using the time-dependent Maxwell's equations," *IEEE Trans. Microw. Theory Tech.*, vol. 23, no. 8, pp. 623–630, 1975.

[25] E. K. Miller, "A selective survey of computational electromagnetics," *IEEE Trans. Antennas Propag.*, vol. 36, no. 9, pp. 1281–1305, 1988.

[26] C. Chauviere, J. S. Hesthaven, and L. Lurati, "Computational modeling of uncertainty in time-domain electromagnetics," *SIAM J. Sci. Comput.*, vol. 28, no. 2, pp. 751–775, 2006.

[27] G. Steiner, A. Weber, and C. Magele, "Managing uncertainties in electromagnetic design problems with robust optimization," *IEEE Trans. Magn.*, vol. 40, no. 2, pp. 1094–1099, 2004.

[28] R. S. Edwards, A. C. Marvin, and S. J. Porter, "Uncertainty analyses in the finite-difference time-domain method," *IEEE Trans. Electromagn. Compat.*, vol. 52, no. 1, pp. 155–163, Feb. 2010.

[29] M. Stein, "Large sample properties of simulations using Latin hypercube sampling," *Technometrics*, vol. 29, no. 2, pp. 143–151, 1987.

[30] H. Niederreiter, *Random number generation and quasi-Monte Carlo methods*. SIAM, 1992.

[31] G. Fishman, *Monte Carlo: concepts, algorithms, and applications*. Springer Science & Business Media, 2013.

[32] F. Yamazaki, M. Shinozuka, and G. Dasgupta, "Neumann expansion for stochastic finite element analysis," *J. Eng. Mech.*, vol. 114, no. 8, pp. 1335–1354, 1988.

[33] G. Deodatis, "Weighted integral method. I: stochastic stiffness matrix," *J. Eng. Mech.*, vol. 117, no. 8, pp. 1851–1864, 1991.

[34] G. Deodatis and M. Shinozuka, "Weighted integral method. II: response variability and reliability," *J. Eng. Mech.*, vol. 117, no. 8, pp. 1865–1877, 1991.

[35] D. B. Xiu and G. E. Karniadakis, "The Wiener-Askey polynomial chaos for stochastic differential equations," *SIAM J. Sci. Comput.*, vol. 24, no. 2, pp. 619–644, 2002.

[36] R. Ghanem and P. Spanos, *Stochastic Finite Element: A Spectral Approach*. Springer-Verlag, 1991.

[37] D. B. Xiu, *Numerical Methods for Stochastic Computations: A Spectral Method Approach*. Princeton, NJ, USA: Princeton Univ. Press, 2010.

[38] A. H. Nayfeh, *Perturbation methods*. John Wiley & Sons, 2008.

[39] S. A. Cummer, U. S. Inan, T. F. Bell, and C. P. Barrington-Leigh, "ELF radiation produced by electrical currents in sprites," *Geophys. Res. Lett.*, vol. 25, no. 8, pp. 1281–1284, 1998.

[40] S. A. Cummer and W. M. Farrell, "Radio atmospheric propagation on Mars and potential remote sensing applications," *J. Geophys. Res.*, vol. 104, no. E6, pp. 14 149–14 157, 1999.

[41] E. R. Williams, "The Schumann resonance: A global tropical thermometer," *Science*, vol. 256, no. 5060, p. 1184, 1992.

[42] M. Parrot, "Statistical study of ELF/VLF emissions recorded by a low-altitude satellite during seismic events," *J. Geophys. Res.*, vol. 99, no. A12, pp. 23 339–23 347, 1994.

[43] W. Harth, "Theory of low frequency wave propagation," in *IN: CRC handbook of atmospherics*, vol. 2. CRC Press, 1982, pp. 133–202.

[44] J. R. Wait, *Electromagnetic wave theory*. Harper & Row New York, 1985.

[45] ——, *Electromagnetic Waves in Stratified Media: Revised Edition Including Supplemented Material*. Elsevier, 2013, vol. 3.

[46] A. Kulak and J. Mlynarczyk, "ELF propagation parameters for the ground-ionosphere waveguide with finite ground conductivity," *IEEE Trans. Antennas Propag.*, vol. 61, no. 4, pp. 2269–2275, 2013.

[47] A. Kulak, J. Mlynarczyk, and J. Kozakiewicz, "An analytical model of ELF radiowave propagation in ground-ionosphere waveguides with a multilayered ground," *IEEE Trans. Antennas Propag.*, vol. 61, no. 9, pp. 4803–4809, 2013.

[48] M. Thèvenot, J.-P. Bérenger, T. Monedière, and F. Jecko, "A FDTD scheme for the computation of VLF-LF propagation in the anisotropic earth-ionosphere waveguide," in *Annales des télécommunications*, vol. 54, no. 5-6. Springer, 1999, pp. 297–310.

[49] J.-P. Bérenger, "FDTD computation of VLF-LF propagation in the Earth-ionosphere waveguide," in *Annales des télécommunications*, vol. 57, no. 11-12. Springer, 2002, pp. 1059–1090.

[50] T. Otsuyama, D. Sakuma, and M. Hayakawa, "FDTD analysis of ELF wave propagation and Schumann resonances for a subionospheric waveguide model," *Radio Sci.*, vol. 38, no. 6, 2003.

[51] J. J. Simpson and A. Taflove, "Two-dimensional FDTD model of antipodal ELF propagation and Schumann resonance of the Earth," *IEEE Antennas Wireless Propagat. Lett.*, vol. 1, no. 1, pp. 53–56, 2002.

[52] H. Yang, V. P. Pasko, and Y. Yair, "Three-dimensional finite difference time domain modeling of the Schumann resonance parameters on Titan, Venus, and Mars," *Radio Sci.*, vol. 41, no. 2, 2006.

[53] R. Cole and E. Pierce, "Electrification in the earth's atmosphere for altitudes between 0 and 100 kilometers," *J. Geophys. Res.*, vol. 70, no. 12, pp. 2735–2749, 1965.

[54] P. R. Bannister, "The determination of representative ionospheric conductivity parameters for ELF propagation in the Earth-ionosphere waveguide," *Radio Sci.*, vol. 20, no. 4, pp. 977–984, 1985.

[55] ——, "Further examples of seasonal variations of ELF radio propagation parameters," *Radio Sci.*, vol. 34, no. 1, pp. 199–208, 1999.

[56] V. C. Mushtak and E. R. Williams, "ELF propagation parameters for uniform models of the Earth–ionosphere waveguide," *J. Atmos. Sol. Terr. Phys.*, vol. 64, no. 18, pp. 1989–2001, 2002.

[57] A. P. Nickolaenko, Y. P. Galuk, and M. Hayakawa, "Vertical profile of atmospheric conductivity that matches Schumann resonance observations," *SpringerPlus*, vol. 5, no. 1, p. 108, 2016.

[58] D. Bilitza and B. W. Reinisch, "International reference ionosphere 2007: improvements and new parameters," *Adv. Space Res.*, vol. 42, no. 4, pp. 599–609, 2008.

[59] D. Bilitza, L.-A. McKinnell, B. Reinisch, and T. Fuller-Rowell, "The international reference ionosphere today and in the future," *J. Geod.*, vol. 85, no. 12, pp. 909–920, 2011.

[60] D. Bilitza, D. Altadill, Y. Zhang, C. Mertens, V. Truhlik, P. Richards, L.-A. McKinnell, and B. Reinisch, "The International Reference Ionosphere 2012–a model of international collaboration," *J. Space Weather Space Clim.*, vol. 4, p. A07, 2014.

[61] A. C. M. Austin, N. Sood, J. Siu, and C. D. Sarris, "Application of polynomial chaos to quantify uncertainty in deterministic channel models," *IEEE Trans. Antennas Propag.*, vol. 61, no. 11, pp. 5754–5761, Nov. 2013.

[62] A. C. M. Austin and C. D. Sarris, "Efficient analysis of geometrical uncertainty in the FDTD method using polynomial chaos with application to microwave circuits," *IEEE Trans. Microw. Theory Tech.*, vol. 61, no. 12, pp. 4293–4301, Dec. 2013.

[63] Z. Zhang, T. A. El-Moselhy, I. M. Elfadel, and L. Daniel, "Stochastic testing method for transistor-level uncertainty quantification based on generalized polynomial chaos," *IEEE Trans. Comput.-Aided Des. Integr. Circuits Syst.*, vol. 32, no. 10, pp. 1533–1545, Oct. 2013.

[64] B. Sudret, "Global sensitivity analysis using polynomial chaos expansions," *Reliab. Eng. Syst. Safe.*, vol. 93, no. 7, pp. 964–979, 2008.

[65] T. Crestaux, O. Le Maıtre, and J.-M. Martinez, "Polynomial chaos expansion for sensitivity analysis," *Reliab. Eng. Syst. Safe.*, vol. 94, no. 7, pp. 1161–1172, 2009.

[66] J. F. Hermance, "Electrical conductivity models of the crust and mantle," *Global Earth Physics: A Handbook of Physical Constants*, pp. 190–205, Wiley Online Library, 1995.

[67] O. Pechony and C. Price, "Schumann resonance parameters calculated with a partially uniform knee model on Earth, Venus, Mars, and Titan," *Radio Sci.*, vol. 39, no. 5, 2004.

[68] G. Molina-Cuberos, J. Morente, B. Besser, J. Portí, H. Lichtenegger, K. Schwingenschuh, A. Salinas, and J. Margineda, "Schumann resonances as a tool to study the lower ionospheric structure of Mars," *Radio Sci.*, vol. 41, no. 1, 2006.

[69] F. Simões, R. Grard, M. Hamelin, J. López-Moreno, K. Schwingenschuh, C. Béghin, J.-J. Berthelier, J.-P. Lebreton, G. Molina-Cuberos, and T. Tokano, "The Schumann resonance: A tool for exploring the atmospheric environment and the subsurface of the planets and their satellites," *Icarus*, vol. 194, no. 1, pp. 30–41, 2008.

[70] C. Béghin, P. Canu, E. Karkoschka, C. Sotin, C. Bertucci, W. Kurth, J.-J. Berthelier, R. Grard, M. Hamelin, K. Schwingenschuh *et al.*, "New insights on Titan's plasma-driven Schumann resonance inferred from Huygens and Cassini data," *Planet. Space Sci.*, vol. 57, no. 14, pp. 1872–1888, 2009.

[71] C. Béghin, O. Randriamboarison, M. Hamelin, E. Karkoschka, C. Sotin, R. C. Whitten, J.-J. Berthelier, R. Grard, and F. Simões, "Analytic theory of Titan's Schumann resonance: Constraints on ionospheric conductivity and buried water ocean," *Icarus*, vol. 218, no. 2, pp. 1028–1042, 2012.

[72] J. Kozakiewicz, A. Kulak, and J. Mlynarczyk, "Analytical modeling of Schumann resonance and ELF propagation parameters on Mars with a multi-layered ground," *Planet. Space Sci.*, vol. 117, pp. 127–135, 2015.

[73] W. R. Hamilton, "Third supplement to treatise on geometrical optics," *The Mathematical Papers of W. R. Hamilton*, 1931.

[74] J. Haselgrove, "Ray theory and a new method for ray tracing," in *Physics of the Ionosphere*, 1955, pp. 355–364.

[75] C. Haselgrove and J. Haselgrove, "Twisted ray paths in the ionosphere," *Proc. Phys. Soc.*, vol. 75, no. 3, pp. 357–361, 1960.

[76] S. C. Aune, "Comparison of ray tracing through ionospheric models," Master's thesis, Dept. of the Air Force, Air Force Inst. of Technol., Wright-Patterson Air Force Base, OH, USA, Mar. 2006.

[77] R. M. Jones and J. J. Stephenson, "A versatile three-dimensional ray tracing computer program for radio waves in the ionosphere," *NASA STI/Recon Technical Report N*, vol. 76, 1975.

[78] C. Rino, "A power law phase screen model for ionospheric scintillation: 1. Weak scatter," *Radio Sci.*, vol. 14, no. 6, pp. 1135–1145, 1979.

[79] K. C. Yeh and C.-H. Liu, "Radio wave scintillations in the ionosphere," *Proc. IEEE*, vol. 70, no. 4, pp. 324–360, 1982.

[80] V. E. Gherm, N. N. Zernov, and H. J. Strangeways, "Propagation model for transionospheric fluctuating paths of propagation: Simulator of the transionospheric channel," *Radio Sci.*, vol. 40, no. 1, 2005.

[81] B. Chaudhury and S. Chaturvedi, "Comparison of wave propagation studies in plasmas using three-dimensional finite-difference time-domain and ray-tracing methods," *Phys. Plasmas*, vol. 13, no. 12, p. 123302, 2006.

[82] D. Bilitza, "International Reference Ionosphere 2000," *Radio Sci.*, vol. 36, pp. 261–275, 2001.

[83] J. M. Forbes, S. E. Palo, and X. Zhang, "Variability of the ionosphere," *J. Atmos. Sol. Terr. Phys.*, vol. 62, pp. 685–693, 2000.

[84] P. G. Richards, "Seasonal and solar cycle variations of the ionospheric peak electron density: Comparison of measurement and models," *J. Geophys. Res.*, vol. 106, no. A7, pp. 12 803–12 819, 2001.

[85] J. S. Belrose and L. W. Hewitt, "Variation of collision frequency in the lowest ionosphere with solar activity," *Nature*, vol. 202, no. 4929, pp. 267–269, Apr. 1964.

[86] W. J. G. Beynon and E. S. O. Jones, "Collision frequency in ionosphere and solar activity," *Nature*, vol. 203, no. 4950, p. 1159, 1964.

[87] D. B. Xiu and G. E. Karniadakis, "Modeling uncertainty in flow simulations via generalized polynomial chaos," *J. Comp. Phys.*, vol. 187, no. 1, pp. 137–167, 2003.

[88] O. M. Knio and O. P. L. Maitre, "Uncertainty propagation in CFD using polynomial chaos decomposition," *Fluid Dyn. Res.*, vol. 38, no. 9, pp. 616–640, 2006.

[89] A. Biondi, D. Ginste, D. D. Zutter, P. Manfredi, and F. Canavero, "Variability analysis of interconnects terminated by general nonlinear loads," *IEEE Trans. Compon., Packag. Manuf. Technol.*, vol. 3, no. 7, pp. 1244–1251, 2013.

[90] F. Boeykens, H. Rogier, and L. Vallozzi, "An efficient technique based on polynomial chaos to model the uncertainty in the resonance frequency of textile antennas due to bending," *IEEE Trans. Antennas Propag.*, vol. 62, no. 3, pp. 1253–1260, 2014.

[91] A. C. M. Austin, "Wireless channel characterization in burning buildings over 100-1000 MHz," *IEEE Trans. Antennas Propag.*, vol. 64, no. 7, pp. 3265–3269, 2016.

[92] J. P. Boris, *The Acceleration Calculation from a Scalar Potential*. Princeton University Plasma Physics Laboratory, 1970.

[93] C. K. Birdsall and A. B. Langdon, *Plasma Physics via Computer Simulation*. Institute of Physics, New York, 1991.

[94] G. A. Sod, "A survey of several finite difference methods for systems of nonlinear hyperbolic conservation laws," *J. Comp. Phys*, vol. 27, no. 1, pp. 1–31, 1978.

[95] R. Garcia and R. A. Kahawita, "Numerical solution of the St. Venant equations with the MacCormack finite-difference scheme," *Int. J. Numer. Meth. Fluids*, vol. 6, pp. 259–274, 1986.

[96] J. Bloxham and D. Gubbins, "The secular variation of Earth's magnetic field," *Nature*, vol. 317, no. 6040, pp. 777–781, 1985.

[97] I. M. Sobol, "Global sensitivity indices for nonlinear mathematical models and their Monte Carlo estimates," *Math. Comput. Simul.*, vol. 55, no. 1, pp. 271–280, 2001.

[98] T. Homma and A. Saltelli, "Importance measures in global sensitivity analysis of nonlinear models," *Reliab. Eng. Syst. Safe.*, vol. 52, no. 1, pp. 1–17, 1996.

[99] K. Budden, *The Propagation of Radio Waves*. Cambridge Univ. Press, New York, 1985.

[100] S. A. Cummer, U. S. Inan, and T. F. Bell, "Ionospheric D region remote sensing using VLF radio atmospherics," *Radio Sci.*, vol. 33, no. 6, pp. 1781–1792, 1998.

[101] T. Tan, A. Taflove, and V. Backman, "Single realization stochastic FDTD for weak scattering waves in biological random media," *IEEE Trans. Antennas Propag.*, vol. 61, pp. 818–828, 2013.

[102] G. Casella and R. L. Berger, *Statistical Inference*, 2nd ed. Pacific Grove, CA, USA: Thompson Learning, 2002.

[103] S. M. Smith and C. Furse, "Stochastic FDTD for analysis of statistical variation in electromagnetic fields," *IEEE Trans. Antennas Propag.*, vol. 60, no. 7, pp. 3343–3350, Jul. 2012.

[104] Y. Yu, "A three-dimensional FDTD magnetized cold plasma model for global electromagnetic wave propagation," Ph.D. dissertation, Univ. of New Mexico, Albuquerque, NM, USA, 2011.

[105] S. M. Smith, "Stochastic finite-difference time-domain," Ph.D. dissertation, Univ. of Utah, Salt Lake City, UT, USA, 2011.

[106] Y. Yu and J. J. Simpson, "A magnetic field-independent absorbing boundary condition for magnetized cold plasma," *IEEE Antennas Wireless Propagat. Lett.*, vol. 10, pp. 294–297, 2011.

[107] R. Pirjola, "Geomagnetically induced currents during magnetic storms," *IEEE Trans. Plasma Sci.*, vol. 28, pp. 1867–1873, 2000.

[108] L. Hakkinen and R. Pirjola, "Calculation of electric and magnetic fields due to an electrojet current system above a layered earth," *Geophysica*, vol. 22, pp. 31–44, 1986.

[109] D. H. Boteler and R. J. Pirjola, "The complex-image method for calculating the magnetic and electric fields produced at the surface of the Earth by the auroral electrojet," *Geophysical J. Int.*, vol. 132, pp. 31–40, 1998.

[110] R. Pirjola and A. Viljanen, "Complex image method for calculating electric and magnetic fields produced by an auroral electrojet of finite length," *Ann. Geophysicae*, vol. 16, pp. 1434–1444, 1998.

[111] J. L. Gilbert, "Modeling the effect of the ocean-land interface on induced electric fields during geomagnetic storms," *Space Weather*, vol. 3, no. 4, 2005.

[112] A. Richmond and Y. Kamide, "Mapping electrodynamic features of the high-latitude ionosphere from localized observations: Technique," *J. Geophys. Res.*, vol. 93, no. A6, pp. 5741–5759, 1988.

[113] A. Richmond, "Assimilative mapping of ionospheric electrodynamics," *Adv. Space Res.*, vol. 12, no. 6, pp. 59–68, 1992.

[114] D. Alekseev, A. Kuvshinov, and N. Palshin, "Compilation of 3D global conductivity model of the Earth for space weather applications," *Earth Planets Space*, vol. 67, no. 1, p. 108, 2015.

[115] A. W. Thomson, A. J. McKay, E. Clarke, and S. J. Reay, "Surface electric fields and geomagnetically induced currents in the Scottish Power grid during the 30 October 2003 geomagnetic storm," *Space Weather*, vol. 3, no. 11, 2005.

[116] H. Lundstedt, "The sun, space weather and GIC effects in Sweden," *Adv. Space Res.*, vol. 37, no. 6, pp. 1182–1191, 2006.

[117] M. Krumpholz and L. P. B. Katehi, "MRTD: New time-domain schemes based on multiresolution analysis," *IEEE Trans. Microw. Theory Tech.*, vol. 44, pp. 555–571, 1996.

[118] Q. H. Liu, "The PSTD algorithm: A time-domain method requiring only two cells per wavelength," *Microw. Opt. Technol. Lett.*, vol. 15, no. 3, pp. 158–165, 1997.

[119] T. Namiki, "A new FDTD algorithm based on alternating-direction implicit method," *IEEE Trans. Microw. Theory Tech.*, vol. 47, pp. 2003–2007, 1999.

[120] G. Fan, Q. H. Liu, and S. A. Hutchinson, "FDTD and PSTD simulation for plasma applications," *IEEE Trans. Plasma Sci.*, vol. 29, no. 2, pp. 341–348, 2001.

[121] L. Zu and N. Yuan, "PLJERC-ADI-FDTD method for isotropic plasma," *IEEE Microw. Wireless Compon. Lett.*, vol. 15, no. 4, pp. 277–279, 2005.

[122] D. L. Paul and C. J. Railton, "Spherical ADI FDTD method with application to propagation in the Earth ionosphere cavity," *IEEE Trans. Antennas Propag.*, vol. 60, no. 1, pp. 310–317, 2012.